WIDE-ANGLE INFRARED CLOUD IMAGING

FOR CLOUD COVER STATISTICS

by

Paul Winston Nugent

A thesis submitted in partial fulfillment
of the requirements for the degree

of

Master of Science

in

Electrical Engineering

MONTANA STATE UNIVERSITY
Bozeman, Montana

January, 2008

APPROVAL

of a thesis submitted by

Paul Winston Nugent

This thesis has been read by each member of the thesis committee and has been found to be satisfactory regarding content, English usage, format, citation, bibliographic style, and consistency, and is ready for submission to the Division of Graduate Education.

Dr. Joseph A. Shaw

Approved for the Department of Electrical and Computer Engineering

Dr. Robert C. Maher

Approved for the Division of Graduate Education

Dr. Carl A. Fox

STATEMENT OF PERMISSION TO USE

In presenting this thesis in partial fulfillment of the requirements for a master's degree at Montana State University, I agree that the Library shall make it available to borrowers under rules of the Library.

If I have indicated my intention to copyright this thesis by including a copyright notice page, copying is allowable only for scholarly purposes, consistent with "fair use" as prescribed in the U.S. Copyright Law. Requests for permission for extended quotation from or reproduction of this thesis in whole or in parts may be granted only by the copyright holder.

Paul Winston Nugent

January 2008

ACKNOWLEDGMENTS

The completion of this thesis has been made possible by the contributions of many groups. First, I'd like to acknowledge those who contributed to the funding of this project. The NASA Stennis Space Center which provided a GSRP fellowship allowing me to pursue the research described in this thesis, and the NASA Jet Propulsion Laboratory (JPL) for the contribution of equipment and monetary funding. Also I'd like to acknowledge the Montana State University Space Science Engineering Laboratory (SSEL) and the Department of Civil Engineering, both who graciously allowed for the use of their environmental chambers.

I'd also like to acknowledge those who contributed to this project in other ways, no less important than funding to the completion of this project. Many of these people are the fellow members of the Montana State University Optical Remote Sensor Laboratory (ORSL) who have helped contribute to this project and my thesis in numerous ways. Either by helping run experiments, often late at night, or by putting up with the messes I often made in the lab. I'd like to acknowledge my advisor Dr. Joseph Shaw whose guidance helped me understand many of the difficult problems addressed in this thesis. I'd also like to acknowledge my parents, Terry and Jody Nugent, and many of my close friends, too many to name here. These people helped encourage me through the processes which eventually lead to the completion of this project. Their contribution cannot be adequately described with words.

TABLE OF CONTENTS

TABLE OF CONTENTS - CONTINUED

TABLE OF CONTENTS - CONTINUED

LIST OF TABLES

LIST OF FIGURES

LIST OF FIGURES - CONTINUED

Table Page

LIST OF FIGURES - CONTINUED

LIST OF FIGURES - CONTINUED

Table Page

LIST OF FIGURES - CONTINUED

Table Page

LIST OF FIGURES - CONTINUED

Table Page

LIST OF FIGURES - CONTINUED

Table Page

LIST OF FIGURES - CONTINUED

ABSTRACT

The Infrared Cloud Imager (ICI) is a radiometrically calibrated thermal infrared imaging instrument currently in development at Montana State University to measure cloud cover statistics. This instrument was developed originally as part of a joint U.S.-Japan effort to study the arctic atmosphere. The ICI provides localized high-resolution data relative to satellites images and, in contrast to visible imaging systems, provides continuous day and night operation. While the original instrument proved the capabilities of using radiometrically calibrated thermal infrared images to produce cloud coverage measurements, this instrument was limited. These limits were primarily the instrument's large size, relatively high cost, narrow field of view, and need to recalibrate the camera for each image. The work presented here covers work conducted to develop two prototypes of a second-generation ICI instrument, and the work which laid the groundwork for the development of a fully deployable version of these systems. These systems are to be used to measure cloud cover statistics for the characterization of optical communication paths by the Optical Communication Group at NASA JPL. The second-generation ICI, based around the FLIR Photon camera, expands the field of view (fov) from 20° to 50° in the early prototype and up to 100° in the latest version, reduces instrument size, reduces instrument cost, and implements a novel internal shutter-based calibration technique. Increasing the fov has required the modification of the routines to process ICI data, in particular to accommodate the angular dependence of atmospheric emission from a clear sky. These processing routines have also been extended to provide cloud type classification in addition to only cloud presence as in the original system. Versions of this instrument have been deployed at Bozeman, Montana, and at JPL's Table Mountain Facility (TMF). During the deployment at Bozeman these instruments have been shown to be accurately calibrated, and that they produce the same data (after accounting for bandwidth and fov differences) while viewing the same scene. Much of the continued work needed to complete this project can be conducted during an extended deployment of these systems, which should take place during early 2008 at JPL's TMF.

INTRODUCTION

Of all the features of the Earth’s atmosphere, clouds are one of the most observed, but possibly least understood. Everyone has at least some memory or idealized image of lying on your back watching the overhead clouds in wonder. This wonder inspired by clouds is not without reason; clouds play an important role in regulating climate, and thus have more impact on our lives than one might assume. The impact on climate, in particular the role clouds play in feedback processes in the Earth's radiation budget, is not fully understood. This facilitates a need for an increase in the understanding of the relationship between cloud cover and local or global climate.

Recently there has been an accelerated push to study and understand cloud cover. This push has led to requirements for more accurate statistical measurements of cloud cover. To truly study something, you need to be able to observe it, and thus determine when it's there, how much is there, and how it changes with time. Such observation is the foundation of science. This is where remote sensing plays its part. The push for accurate and consistent remote sensing of cloud cover prompted the development of various types of instruments capable of measuring long term cloudiness on both a local and global scale. There are still many opportunities to develop instruments for cloud measurements in comparison to many other fields of remote sensing. As said by Graeme Stephens in his book *Remote Sensing of the Lower Atmosphere,* “Remote sensing of clouds looms as an important aspect of global climate change…. The field is not as highly developed as other topics in remote sensing.”

Motivations for Cloud Cover Studies

The motivation behind the development of an instrument for studying cloud cover statistics has been twofold. The first of these motivations has been the need to study cloud cover as part of an effort to understand the impact of global cloud cover on climate. This motivation for understanding clouds has been part of an attempt to answer the questions surrounding global climate change. The demand for an answer to this question has increased in recent decades, as the effects of global climate change have become a social and political point of interest. Attempts to better understand the global climate facilitated the development of climate models. Most of these models are based around a General Circulation Model (GCM) or similar model [*Wild et al. 2001*]. These models simulate variations in the Earth's atmosphere such as increasing cloud cover, increasing greenhouse gas concentrations, or changing solar flux to predict future climate trends. Thus, an accurate understanding of global cloud coverage is required. This push to understand cloud cover and its role in climate has facilitated the development of instruments capable of measuring cloud cover statistics on global and local scales.

The second motivation, which has arisen more recently, has been the establishment of Earth-space optical communication links [*Piazzolla et al. 2000*]. These are dependent on a free-space laser link between Earth-side telescopes and on-orbit or deep-space communication platforms [*Churnside and Shaik 1989*]. The availability of a free-space laser link has a fundamental dependence on the cloud cover occurring at the Earth based telescope receiver site. This has facilitated a push to develop instruments capable of studying the localized cloud cover around these sites or prospective sites. This project arises from an attempt at developing an instrument capable of fitting both the needs of the climate research and Earth-space optical communication channel characterization.

Climate and Atmospheric Research

Clouds play an important role in regulating the Earth's radiation budget, and thus any change in climate. Clouds act as part of a radiative forcing feedback loop [*Wetherald and Manabe 1988*]. The net effect of this radiative forcing can have either a cooling or warming effect on the Earth, dependent on conditions. Clouds provide cooling by reflecting sunlight, and thus preventing energy from reaching the surface of the earth. Warming by clouds takes place when clouds absorb long-wave radiation emitted from the Earth's surface, and decrease the loss of energy from the surface-atmosphere system [*Wetherald and Manabe 1988*]. This decreases the rate of cooling at the surface, and thus has a net warming effect. Whether the net effect is heating or cooling is dependent on numerous variables including type of cloud, percentage of the sky covered, time of day, and seasonal variations. Thus, an accurate understanding of the Earth's climate requires an understanding of cloud cover.

During the late 20th century through the present, the need for understanding the global climate has facilitated the development of meteorological satellites capable of measuring cloud cover statistics on a global scale. The first of these satellites was the TIROS satellite launched by NASA in 1960 [*TIROS 1962*]. In the years to follow, such systems became a common part of the effort to understand the Earth's weather and climate. These systems have greatly improved the scientific community's understanding of cloud cover on a global scale. This level of understanding of cloud cover is required on both a global and a more local scale. Localized cloud cover statistics are important for the validation and improvement of climate models. If local cloud cover is well known for a single location or set of locations it can be used as a reference point to validate global climate models.

The least understood component of cloudiness, and thus global climate, is the impact of cirrus clouds. Cirrus clouds are of particular difficulty because of the ability of these high altitude clouds to have both a warming and cooling effect on the surface of the Earth and the atmosphere [*Liou 1986*]. Thus, any accurate global climate model requires an accurate measurement of the statistical distribution of cirrus clouds.

Earth-space Optical Communication

The establishment of Earth-space optical communication between terrestrial telescope sites and space-borne communication platforms is under development by groups such as the National Aeronautical and Space Administration (NASA). This work is primarily being conducted through NASA's Jet Propulsion Laboratory (JPL). The establishment of these links has been driven by an ever-increasing demand of high data return from near and deep-space missions [*Piazzolla 2007*]. Earth-space optical communication is seen as a good alternative and/or extension to radio-based communication. This requires the establishment of free-space optical communication links between Earth-side telescope sites and orbiting satellites or deep-space platforms [*Piazzolla et al. 2000*]. Free-space optical communication along an Earth-space path requires an obstruction-free communication path, and thus is dependent on local cloud cover. Thick clouds will completely block the laser signal, breaking the communication link. Thin clouds will scatter the beam, removing power from the signal path, and degrading signal quality. This scattering of the communication signal can lead to intersymbol interference of the transmitted data, causing errors in the received data [*Churnside and Shaik 1989*]. These issues create a need for reliable classification of spatial and temporal cloudiness, cloud type, and cloud optical thickness at Earth-side communication sites.

The link availability of a particular optical communication channel can sometimes be improved through the use of multiple Earth-side communication sites. The selection of these sites requires knowledge of the long-term cloud coverage to enable calculation of site diversity statistics. The selection of such sites requires that the local weather patterns, particularly cloud cover, be anti-correlated [*Piazzolla et al. 2000*]. Therefore, a statistical understanding of localized cloud cover is required in the development of a network of communication sites for Earth-space optical communication. These paths, along which the communication channels exist, will not be targeted at fixed locations in the sky due to the orbit of non-geosynchronous near-Earth space-side platforms, or due to the rotation of the Earth for deep-space platforms. Geosynchronous platforms would avoid this problem as the communication path would remain fixed to a single point. These statistics need to contain both spatial and temporal data, to characterize both seasonal and angular variability.

In an effort to develop the required site-diversity cloud cover statistics, the Optical Communications Group at the NASA’s JPL instituted the Atmospheric Visibility Monitoring (AVM) program [*Jeganthan and Erickson 1997*]. Three of these AVM sites are located in the southwest United States and have been in operation since 1994 [*Jeganthan and Erickson 1997*]. The sites use a combination of sensors, including a star-imaging-based multi-wavelength atmospheric visibility sensor, a seeing monitor that characterizes atmospheric turbulence, and a series of other instruments. The data collected have been used to develop models that allow for the analysis of link-margin studies. These studies were designed for the design of hypothetical optical Earth-space communication channels [*Erickson and Tsiang 1999*].

Requirements of an Instrument to Fit These Applications

An instrument capable of collecting the required data for cloud cover statistics for climate studies would need to meet the following requirements: it would be capable of operating remotely and in harsh environments; it would provide continuous data day or night, and with the same detection methods and sensitivity levels; it would be able to detect thin high-altitude cirrus clouds; and it would be capable of measuring clouds in a large portion of the sky.

The second motivation of cloud detection for Earth-space optical communication dictates a nearly similar set of instrument requirements: it needs to be able to provide continuous data, day and night; it needs to operate at telescope receiver sites often located in remote and harsh environments; it needs to be able to detect thin cirrus clouds, and it needs to measure clouds over an extended region of the sky. Unlike the instrument for climate research, one for communication path characterization ideally would be capable of providing real-time cloud distribution data to allow for prediction of communication link availability.

The instruments commonly used for collecting statistical cloud data do not immediately meet the combined need of both climate research and communication path characterization. Some of these instruments come close in meeting all these needs; however, there is no single instrument that is capable of providing the desired localized cloud coverage data needed in both these applications. Thus, to meet the needs of climate research and Earth-space optical communication, a new instrument was needed.

Methods of Cloud Detection

The first scientific characterization of cloud coverage was visual observations by trained technicians or automated stations. These observations classified the percentage of the total sky cloud cover into eight categories or ‘oktas’. These values ranged from zero, for no clouds present, to eight, for a fully obscured sky [*OFCM 2005*]. The accuracy of such observations is highly variable and only available when the clouds can be visibly observed. This method posed problems during nighttime at any location and in particular during the Arctic and Antarctic winters [*Town et al. 2007*].

Although observations made by trained professionals still are relied upon as part of the global effort to determine cloud cover, more often scientific studies of clouds rely on remote sensing instruments. These cloud detection instruments fall into two categories: passive sensors and active sensors. Passive sensors rely on naturally occurring signals, such as thermal emission or scattered visible light, to determine the presence and characteristics of clouds. Active sensors, such as radio detection and ranging (RADAR) or light detection and ranging (LIDAR), transmit a signal and observe its scattered return.

Passive Detection Systems

Passive sensing of clouds relies on naturally occurring signals such as thermal emission or scattered sunlight to determine the presence and properties of clouds. This allows these sensors to be simpler in contrast to active sensing systems, as there is no reliance on a transmitted signal. However, this is also a limitation of these sensors as they are dependent on a signal that may vary diurnally and seasonally.

Radiometers can be used to measure the radiation emitted from the atmosphere or overhead clouds. These instruments measure this information over a wide frequency range, ranging from the microwave into the long-wave and mid-wave infrared [*Stephens 1994*]. These systems are often limited in that they provide only a single data point, typically aimed at the zenith. Spatial data can be obtained by scanning to cover a larger portion of the sky over some scanning period. More often to provide spatial data, these zenith-viewing systems relate temporal cloud cover statistics to spatial cloud cover statistics through the use of Taylor's Hypothesis. This model proposes that temporal cloud coverage statistics along a single point are the same along the direction of the mean wind [*Sun and Thorn 1995*]. Under conditions in which Taylor's Hypothesis breaks down, such as forming or dissipating clouds, the relations between spatial and temporal cloud data could not be made [*Thurairajah and Shaw 2005*]. This is a prominent limitation of cloud detection with zenith-viewing sensors.

Visible-wavelength imagers, such as the Total Sky Imager (TSI) and the Whole Sky Imager (WSI), are an alternative to the single-pixel systems and thus do not rely on Taylor's Hypothesis. Both these instruments are visible-wavelength cloud imagers that use sunlight to passively image overhead clouds during daytime operation, typically using a red-blue ratio to determine cloud presence [*Long et al. 2001, Tooman 2003*]. The WSI can operate at night, and when sufficient moonlight is not present it operates by comparing visible stars with star maps, and assuming non-visible bright stars are blocked by clouds [*Tooman 2003*]. This means that the WSI is constantly changing imaging methods, and thus sensitivity levels and resolutions. The TSI instrument avoids these problems by only operating during the daytime [*Long et al. 2006*]. Both these instruments and other similar visible-wavelength cloud imaging systems are limited in their ability to provide continuous data sets, either due to diurnal periods of non-operation or changing acquisition methods. None of these systems are capable of providing cloudiness measurements during twilight periods [*Tooman 2003*]. Twilight periods are a time of interest due to possible rapid changes in cloudiness due to warming or cooling of the atmosphere and surface.

Satellite imaging is another passive sensing solution that has been extensively used for the collection of cloud cover statistics, particularity thermal imaging from Earth orbiting satellites [*Minnis et al. 2001*]. These data provide calibrated imagery of cloud-top emission day and night with a continuous detection method. The data they produce have spatial scales from tens of kilometers per pixel to a few kilometers per pixel [*Minnis et al. 2001, Baum et al. 1995*]. These data have been important in the development of global climate models. However, these data do not provide sufficiently high resolution to characterize localized cloud coverage needed for climate research and characterization of Earth-space communication channels.

Active Detection Systems

All active sensors operate on the basic principle of transmitting a signal and monitoring the scattering of this signal off some object, such as a cloud. The returned signal is essentially an echo of the transmitted signal, and thus the time delay between transmission and receptions can be used with the amplitude of the returned signal to determine properties of the scattering object [*Stephens 1994*]. Thus, the use of active sensors for cloud detection has some distinct advantages over passive systems by providing unique information, such as cloud height.

The most commonly used active sensors for cloud detection are RADAR and LIDAR. Both these sensing systems can provide information such as cloud presence and cloud height. Some systems, such as the Multi-Application Montana LIDAR (MAML), can be used to derive cloud properties such as the presence of ice through the use of additional information such as the de-polarization ratio of the returned signal [*Seldomridge 2005, Seldomridge et al. 2006*]]. The capability of providing this additional information is one of the benefits of active sensing systems over passive sensors in cloud detection.

Many active sensors are limited to providing only single-pixel data, and usually only the directly overhead cloud cover. Spatial statistics can be achieved by scanning the instrument, but this adds complexity and thus cost to the instrument. Therefore scanning systems for remote, continuous cloud detection are rare, and instead active sensors typically rely on Taylor's Hypothesis to estimate spatial cloud cover from zenith cloud statistics. Thus, many active sensors suffer from the limitations of this model, and cannot accurately predict total cloud cover during rapidly changing conditions.

Ground-Based Thermal Imaging for Cloud Detection

Developing knowledge of cloud cover statistics for climate research and Earth-space optical communication can be met on a local scale by the same instrument. This is true if the instrument is designed to fit the specific requirements of both applications, and this is done without sacrificing capabilities that are uniquely required by each application.

One possible solution is to use an upward-looking, ground-based thermal imaging sensor. This system would be similar to the downward-looking thermal imaging sensors commonly used by meteorological satellites to image clouds.

Detection of thermal emission from clouds with an upward-looking infrared imaging detector is quite different from cloud detection with a downward-looking detector on a satellite. Localized cloud coverage can be highly variable on a level equal to the pixel-to-pixel difference of the satellite data. This is especially true in mountainous regions, where topography has a strong effect on cloud cover.

The differences are not limited only to spatial resolution alone, but also extend to the information contained within the data themselves. Downward-looking detectors face the problem of relatively cold cloud tops which are seen against the relatively warm surface of the Earth. This can be a problem, as the surface of the Earth is uniform in neither temperature nor emissivity. Surface temperature varies with incident solar radiation, which is dependent both on day/night variability, and the local cloud coverage. This variability is added to variations in surface emissivity, due to the local variations in the Earth's surface from geographic makeup, vegetation, and human impact. The combination of these factors leads to a highly variable background [*Stephens 1994*]. This causes a problem of varying contrast based on localized conditions, and is most significant near the poles as the surface becomes colder [*King et al. 1992, Liu et al. 2004*]. In upward-looking detectors this problem is avoided. Rather than having clouds contrasted against the variable and radiometrically bright surface of the Earth, clouds are contrasted against the emission of the atmosphere, which is also variable but radiometrically much less bright than most clouds. This causes the clouds to appear warmer than the background. The atmospheric background emission can be accurately estimated using measurable parameters such as precipitable water vapor. Precipitable water vapor is the depth of liquid water that would result from compressing the entire atmospheric column of water vapor to the point of saturation, and is typically measured in cm. Also, the cloud-to-space contrast is often much greater than the cloud-to-ground contrast [*Stephens 1994*].

Ground-based thermal imaging of overhead clouds is ideal for providing the continuous day and night high-spatial-resolution cloud cover statistics not achievable with other detection methods. The statistics from such an instrument could include spatial measurements of cloud amount, temporal cloud amount, effective cloud-base temperature, and cloud type based on a cloud's brightness temperature. If combined with a cloud-height measurement or estimate, the instrument would be capable of providing cloud emissivity measurements. This is in contrast to many other cloud detection methods, which only produce data such as cloud amount and sometimes additional useful information such as effective particle size [*Stephens 1994*].

The Infrared Cloud Imager

Over a time period between 1999 and 2007, the Optical Remote Sensor Laboratory (ORSL) at Montana State University (MSU) and the National Oceanic and Atmospheric Administration (NOAA), in collaboration with the Communication Research Lab of Japan (CRL, now the National Institute of Information and Communication Technology, or NICT), have worked on developing the Infrared Cloud Imager (ICI). The ICI instrument is a ground-based thermal imaging system that can provide high-spatial-resolution localized cloud cover statistics. Figure 1-1 shows the ICI during a deployment at the Poker Flat Research Range (PFRR) near Fairbanks, AK in 2005.

This instrument is an upward-looking thermal infrared imager which uses a two-point blackbody reference to yield radiometrically calibrated images of a portion of the overhead sky. The ICI system was originally developed for studying the impact of cloud cover on climate. As part of this research the ICI has been deployed at Atmospheric Radiation Measurement (ARM) sites at Barrow, AK and Lamont, OK [*Thurairajah 2004, Thurairajah and Shaw 2005*]. These sites contain a variety of other instruments to which comparisons could be made. The instrument has also been deployed at PFRR in AK, Boulder, CO, and Bozeman, MT.

Figure 1-1. The original ICI during a deployment at Poker Flat Research Range, AK. The ICI camera and calibration equipment are inside the white housing in the foreground. The instruments in the background are other instruments at the site operated by other groups. (Photo by J. Shaw)

The reliability of the ICI for cloud detection has been proven during these deployments through comparisons with other instruments at these sites; including microwave radiometers, cloud LIDARS, and visible-wavelength cloud imagers [*Thurairajah and Shaw 2005, Shaw et al. 2005*]. During the deployment at the ARM site in Lamont, OK it was determined that the cloud amount (the portion of the ICI image that contained clouds) was larger when determined from the full image than when determined from a single-pixel time series [*Thurairajah and Shaw 2005*]. This suggests that single-pixel zenith-viewing systems such as LIDARs and radiometers may under sample cloudiness during variable conditions such as developing or dissipating clouds. This under-sampling of zenith-viewing systems suggests a breakdown of Taylor's Hypothesis during these conditions. Subsequent deployments at the ARM site in Barrow, AK showed better agreement between single-pixel and full-image cloud amount. This is likely due to the higher uniformity and temporal stability of arctic clouds, but also needs to be studied with images covering a larger field of view (fov) than the 18.5°×13.5° fov of the original ICI system.

The ARM sites also included instruments such as the WSI. During a deployment at the Lamont, OK ARM site in 2003, comparisons between the cloud amounts measured by the ICI and WSI showed good correlation during daytime, but poor correlation during nighttime [*Thurairajah and Shaw 2005*]. This difference is most likely caused by the WSI changing detection methods between daytime and nighttime readings, whereas data from the ICI uses a consistent detection method during day and night.

The ICI instrument was originally developed to prove the feasibility of using uncooled microbolometer detector arrays for measuring cloud statistics. The original target was the collection of cloud cover statistics for climate research. As a proof of concept, the instrument operated well. Modifications needed to be made to extend the capabilities of the instrument for climate research, and to adapt the instrument to the characterization of Earth-space optical communication paths. This is primarily due to the reasonably large size and weight, and its relatively narrow fov of the original ICI. The desired modifications were largely the same for both target applications, and the development of a second-generation ICI started in March 2006.

The Second-Generation Infrared Cloud Imager

The development of the second-generation ICI instrument has been the focus of collaboration between researchers at ORSL at MSU, the Optical Communications Group at the NASA JPL, and the Earth Systems Science Office at the NASA Stennis Space Center (SSC). This second-generation ICI instrument is designed to be capable of providing cloud-cover statistics for climate research, along with the characterization of optical Earth-space communication paths.

For the second-generation ICI instrument to fit a dual-use application, the instrument had to be improved to fit the specific needs of the characterization of optical communication channels, while keeping the instrument usable to the original application of climate research. The major goals for the second-generation ICI instrument were to increase the field of view, reduce the size, and reduce the cost of the instrument. Increasing the full-angle fov to nearly 100° allows the instrument to provide spatial cloud statistics over a wider angular area. Coverage of a wider area is desired for both the climate research application and characterizing Earth-space optical communication paths.

Reducing the size and cost allows the development of multiple instruments and for the ease of re-deployment as different sites or regions are investigated.

The core of the wide-angle ICI instrument is the Photon Core thermal infrared camera, an uncooled microbolometer camera from FLIR Indigo Systems. This camera was selected for use in the second-generation ICI primarily for its low cost and small size. In this camera the focal plane array (FPA) resolution is 324×256 pixels, the same as the original ICI. Thus, by increasing the field of view of the second-generation ICI, greater coverage of the sky dome is achieved, but with reduced instantaneous fov. Operational specifics of this camera will be discussed in depth in following chapters.

As part of this project, two second-generation ICI systems were developed. One of the cameras used in these systems is the Photon core with a 14.25-mm focal-length lens. This configuration provides a 50°x38° full-angle fov (the “50° system”), which allows for viewing of 8.8% of the total sky dome. The second configuration uses an after-market lens to provide an 86°x67° full-angle fov (the “100° system” – indicating the larger diagonal fov). This system can view 25.6% of the overhead sky. Both configurations are an improvement over the original ICI which had a field of view of 18.5°x13.5°, or 1.4% of the overhead sky.

Monte Carlo modeling has shown that 100° is nearly the ideal full-angle field of view for measuring spatial cloud statistics from the ground [*Kassianov et al. 2005*]. For zenith angles greater than 50° (full-angle fov > 100°), it becomes increasingly difficult to remove the dependence cloud coverage statistics have on the position of the cloud in the imager’s field of view (i.e., statistics become biased by seeing cloud sides at the edge of the field). To accurately account for this, additional data are needed on cloud aspect ratio from a collocated scanning LIDAR or RADAR. At zenith angles greater that 60° it becomes nearly impossible to remove the field-of-view dependence from the measured cloud coverage statistics. These results have been found both with simulated data and with actual cloud data from the ARM Total Sky Imager (TSI) [*Kassianov et al. 2005*].

In the project reported here, the 50° fov system was developed primarily as an ultra-compact system for characterizing Earth-space communication paths, and the 100° fov system was developed for both applications, but especially to provide a near-optimal angular coverage for measuring cloud amount in climate studies. Basing these imagers on the FLIR Photon core camera has dramatically reduced size, and thus allows the system to be more easily deployed at multiple locations, and makes it more feasible to build multiple versions of the instrument at low cost.

Successfully increasing the ICI field of view required modifications to the data processing procedures. In particular, the water vapor correction routines needed to be adapted to account for pixel viewing angle. Thus, accurate measurements of the per-pixel field of view and pointing angle were required for a full correction of water vapor radiance over the entire field of view.

The 50° fov system was successfully deployed at the JPL Table Mountain Facility from Dec 2006 through March 2007, and will be redeployed at this facility soon. The TMF deployment demonstrated the application of thermal cloud imaging for the detection of clouds in Earth-space communication paths. The new ICI systems are a relatively low cost and simple solution to the need for high spatial and temporal resolution cloud cover statistics. These statistics are integral to the characterization of

Earth-space communication paths, especially for site-diversity statistics needed for the evaluation of possible Earth-side communication sites.

Currently work is underway to ready a 100° fov ICI system for deployment at JPL's Table Mountain Facility, and to construct an Arctic version of the 100° fov ICI for deployment at locations such as the ARM site in Barrow, AK. Long-term deployment of either of these systems will require the system to be adapted to operate in varied climate conditions, including snow, rain, heat, and cold.

This thesis provides an overview of the development of the second-generation ICI systems. This work is presented here in five chapters, the introduction plus the following four chapters. These chapters are laid out the following order: Chapter 2 presents the development of the processing routines for the ICI systems and the modifications that needed to be made when increasing the fov of these systems; Chapter 3 presents a detailed description of the calibration routines developed to allow the ICI systems to provide calibrated measurements of scene radiance; Chapter 4 presents an overview of the data taken with these systems during the deployments at Bozeman MT and at the TMF; Chapter 5 concludes the work conducted as part of this thesis and provides an overview of future work that needs to be conducted, including deployment of these systems and application of the data to scientific problems. Overall these chapters provide an overview of the development of the second-generation ICI prototype systems developed over a time period from 2005 through 2007.

EXTENSION OF THE ICI METHOD FOR CLOUD DETECTION TO WIDE FIELD-OF-VIEW CAMERAS

The ICI method of cloud detection is based on using a thermal camera to radiometrically image the downwelling radiation from the overhead cloud cover. This forms an image in which the clouds have relatively high radiance and the background sky has relatively low radiance. This effect causes the clouds to look warmer than the overhead sky. However, isolating the cloud signal from the intervening atmospheric radiance is not a trivial problem. The atmospheric background can be highly variable, based on local conditions. This chapter describes the concepts and processing routines needed to separate cloud signatures from the atmospheric background.

Atmospheric Effects in the Long-Wave Infrared

Most thermal infrared cameras operate in one of two wavelength bands where there is relatively little emission from the atmosphere, hence relatively high transmission. These spectral regions are called atmospheric windows. The Photon Core cameras used in this project operate in the long-wave infrared window from 8 μm to 13 μm. There is some response of these cameras at the edge of this window, just below 8 μm and just above 13 μm. To understand the operation of these cameras within this spectral region, and to build a cloud detection processing algorithm for these cameras, the atmospheric emission in this band needs to be understood.

Atmospheric MODTRAN Simulations

To build the understanding needed for this project, simulation software was used to build a representation of the signals that a cloud detection system such as the ICI would observe. The atmospheric radiative transfer software MODTRAN was used to simulate the expected atmospheric downwelling, or downward-emitted, thermal emission. Figure 2-1 shows three different simulations based on a U.S 1976 Standard Atmosphere model [*Anderson et al. 1986*] over a spectral band from 7 µm to 15 µm. This simulation shows three distinctly different atmospheres, all with a clear sky and ground altitude of 1.524 km, the altitude of the observations based at Montana State University (MSU). These atmospheres are a nearly water-vapor-free sky, a clear sky with the 1976 U.S. Standard water vapor profile [*Anderson et al. 1986*], and a clear sky with twice the standard water vapor content.

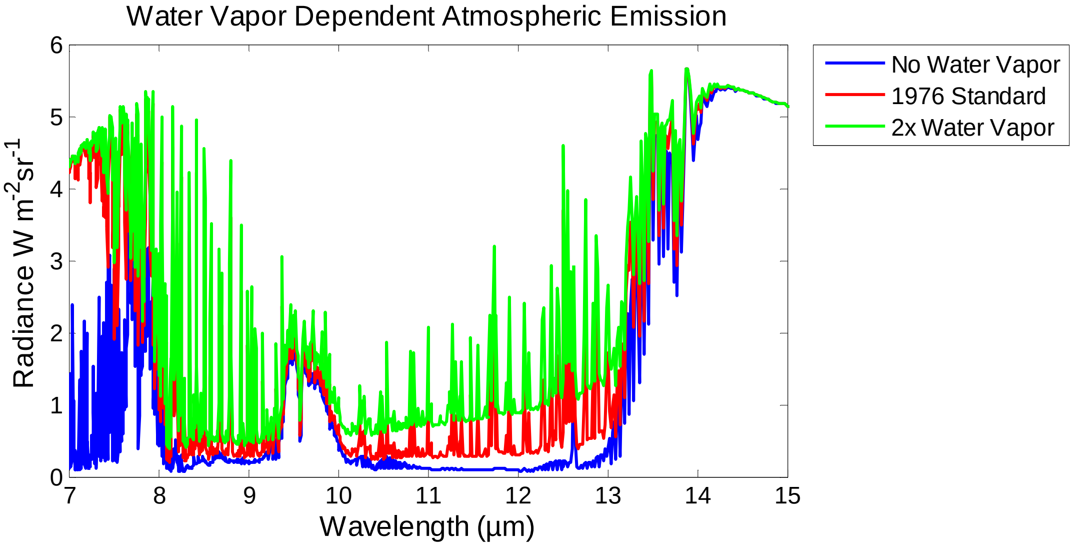

Figure 2-1. MODTRAN-simulated downwelling atmospheric emission spectrum for three different cloud free atmospheres: (bottom) zero water vapor, (middle) 1976 U.S. Standard profile, and (top) twice the standard water vapor profile.

There is a window region of low atmospheric absorption and emission from approximately 8 μm to 13 μm. This band is often referred to as the atmospheric water vapor window, in which both low thermal emission and low absorption are present [*Stephens 1994]*. The two major sources of emission or absorption in this band are O_3 (ozone) centered at 9.6 μm and water vapor throughout [*Stephens 1994*]. Removing water vapor from the atmosphere in this region leaves a nearly zero background, excluding the region of ozone emission around 9.6 μm.

The low absorption in the 8 μm to 13 μm spectral region leads to high atmospheric transmittance. Figure 2-2 shows a MODTRAN-simulated transmittance spectrum, calculated for the U.S. 1976 Standard Atmosphere model for a zenith path to space. This simulation contains both normal and doubled water vapor; the no-water-vapor case was omitted.

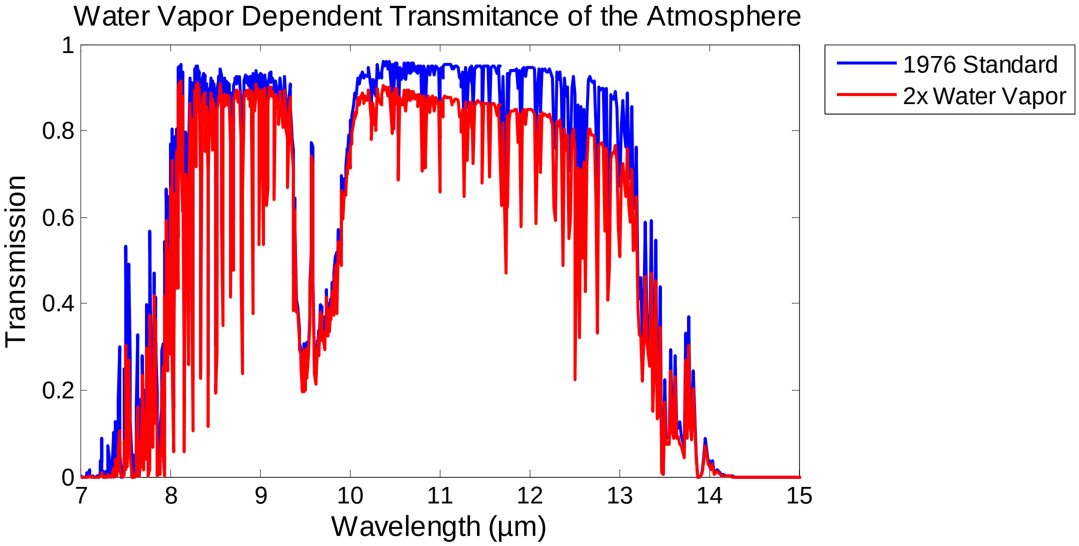

Figure 2-2. MODTRAN-simulated transmittance over the 7 μm to 15 μm band, using the 1976 model atmosphere with a zenith path to space.

In the water vapor window there is high transmittance everywhere except for the region around 9.6 µm with O_3 absorption. Increasing the water vapor content of the atmosphere increases the atmospheric absorption and therefore decreases the transmittance in the 8 µm to 13 µm window.

Liquid water clouds also absorb and emit throughout this spectral region, nearly as opaque black bodies [*Shaw and Fedor 1993*]. Ice clouds emit over the entire spectrum, but usually have much lower optical thickness. Figure 2-3 shows a MODTRAN simulation of cloud emission over this region. The U.S. 1976 Standard Atmosphere clear-sky emission spectrum is shown as a reference, along with three cloud types: high-altitude cirrus clouds at 9 km, mid-altitude alto-stratus clouds with a cloud base at 2.4 km and top at 3 km, and low-altitude cumulus clouds with a base at 0.066 km and top at 3 km.

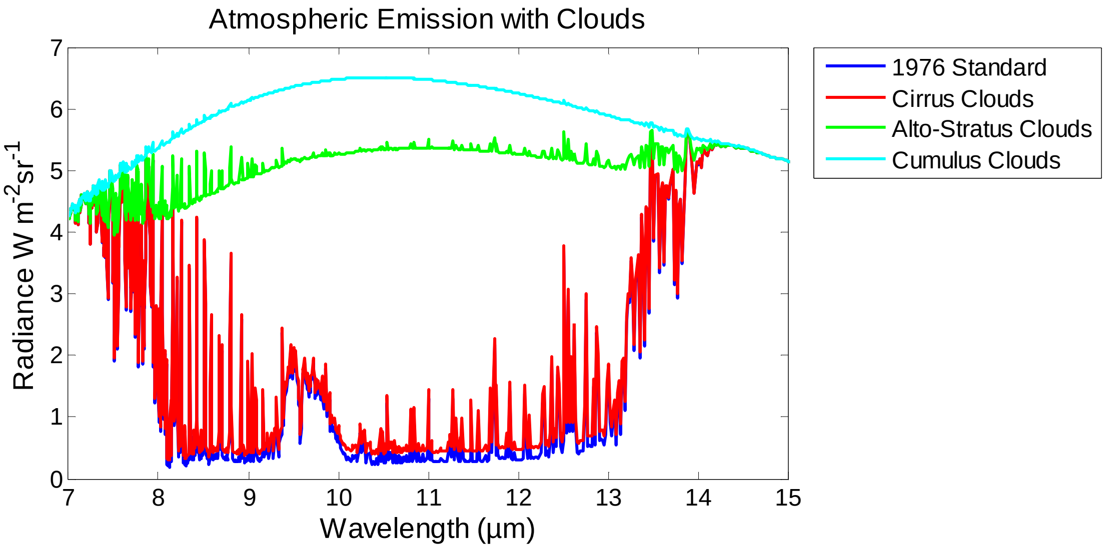

Figure 2-3. MODTRAN-simulated downwelling emission over the 7 µm to 15 µm band, for the 1976 U.S. Standard Atmosphere model. The plot contains a clear sky (bottom) and three cloud types: cirrus at 9km (red), alto-stratus at 2.4km (green), and cumulus at 0.066km (teal).

The differences in integrated radiance of the different clear and cloudy atmospheres from Figure 2-1 and Figure 2-3 are presented in Table 2-1. Integrated radiance is the total detectable radiance integrated across the bandwidth of a detector such as the ICI cameras. For the data presented in Table 2-1 it was assumed that the detector had full response across the total 7 μm to 15 μm band. This is not an entirely realistic representation of an instrument, but it does provide a good comparison between the different signals from the clear and cloudy atmospheres presented. The most important differences to note are those between the clear U.S. 1976 Standard Atmosphere, the U.S. 1976 Standard Atmosphere with doubled water vapor, and the 1976 Standard Atmosphere with the addition of thin cirrus clouds. The difference in integrated radiance due to doubling the water vapor content is greater than the difference seen from the addition of thin cirrus clouds. Thus, to reliably detect thin clouds, the atmospheric emission needs be calculated and removed.

Table 2-1: Integrated Radiance for Clear and Cloudy Atmospheres

Atmosphere Type	**Integrated Radiance**	**Difference from 1976 Standard**
1976 Standard	17.42 $W \cdot m^{-2} \cdot sr^{-1}$	0 $W \cdot m^{-2} \cdot sr^{-1}$
1976 2x Water Vapor	20.47 $W \cdot m^{-2} \cdot sr^{-1}$	+ 3.06 $W \cdot m^{-2} \cdot sr^{-1}$
1976 No Water Vapor	12.13 $W \cdot m^{-2} \cdot sr^{-1}$	- 5.28 $W \cdot m^{-2} \cdot sr^{-1}$
1976 Cirrus Clouds	18.17 $W \cdot m^{-2} \cdot sr^{-1}$	+ 0.75 $W \cdot m^{-2} \cdot sr^{-1}$
1976 Alto-Stratus Clouds	41.65 $W \cdot m^{-2} \cdot sr^{-1}$	+ 24.23 $W \cdot m^{-2} \cdot sr^{-1}$
1976 Cumulus Clouds	47.93 $W \cdot m^{-2} \cdot sr^{-1}$	+ 30.52 $W \cdot m^{-2} \cdot sr^{-1}$

Need for a Radiometric Calibration and Water Vapor Measurements

The combination of low atmospheric emission and high cloud emission makes the band from 8 μm to 13 μm the ideal band for thermal imaging of clouds. This is especially true in fairly dry atmospheres with low intervening water vapor emission. However, there exists a background signal due to water vapor, O_3, and CO_2 emission that is dependent on both the total amount of water contained in the atmosphere, or precipitable water vapor, and the temperature of the atmosphere. Both of the values are highly variable, and hence the induced background signal is highly variable.

As shown in Table 2-1, the variability of this background emission is greater than the difference between the background and the emission from a cirrus cloud. Thus, to detect cirrus clouds, the removal of this background signal is required. The background signal can be calculated, but using this value requires that the camera in the ICI run in a radiometrically calibrated mode. Radiometrically calibrated cameras measure the optical power emitted from the scene (for example, in terms of radiance, $W \cdot m^{-2} \cdot sr^{-1}$), and not just the scene contrast as is common in non-calibrated imagers.

Calibrating the camera for radiance has advantages over other techniques, such as calibrating in temperature space, as is commonly done in many commercial thermal imaging systems. Scene radiance is linear with a measurement of optical power on the detector, whereas a scene temperature can appear linear over a narrow range, but when calibrating over a wide range such as in the ICI this apparent linearity breaks down because of the highly nonlinear dependence of optical power on temperature through the Planck function. Radiometric calibration also has the advantage of requiring no assumptions about the emissivity of the objects in the scene. Thus, the cameras used in the ICI systems operate in a radiometrically calibrated mode. If desired, scene temperature can be retrieved from the radiometric data. These temperatures can be the brightness temperature, the temperature of a perfectly emitting blackbody with an emissivity of one for the observed radiance, or they can be the physical object temperature derived using the object's emissivity.

The Cloud Data Processing Routine

The process used for the first-generation ICI is as follows: calibrate the sky data, measure the precipitable water vapor, calculate the band-average atmospheric radiance from water vapor and near-surface air temperature, subtract background radiance from the calibrated data to yield a residual radiance file, threshold residual radiance file to detect clouds. Figure 2-12 shows the flow diagram of this processing routine. The threshold used to detect clouds was a single-value threshold (except that this threshold was varied when necessary to account for cases of thick haze) and only allowed determination of cloud presence [*Thurairajah and Shaw 2005*].

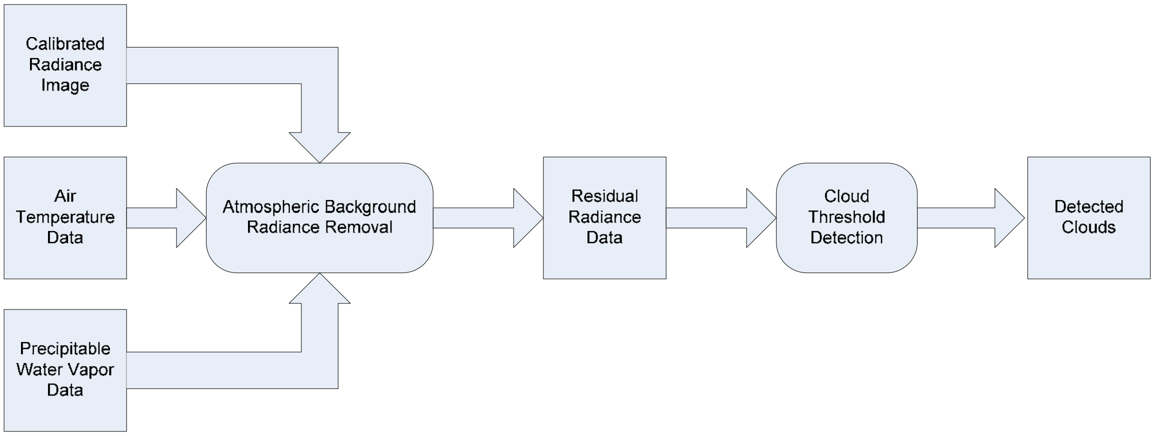

Figure 2-4. Flow diagram of the processing algorithm used for cloud detection in the original ICI. This processing method only allowed for the detection of cloud presence, and not cloud type.

Water Vapor Radiance Correction

In the first-generation ICI system an accurate calculation of the precipitable-water-vapor-dependent atmospheric radiance was determined. For the deployment in Barrow, AK, a single water vapor correction was developed. This was done by running MODTRAN simulations for various precipitable water vapor levels, and various atmospheres ranging from dry sub-arctic winter to humid tropical conditions [*Thurairajah 2004*]. A polynomial was fit to these data, producing the following equation for the Barrow model:

$$L_{sky} = 0.1659wv^2 + 4.368wv + 3.835 \quad [\mathrm{W \cdot m^{-2} \cdot sr^{-1}}] \tag{2.1}$$

This model worked well and allowed for the removal of the background radiance during the deployment in Barrow, AK. However, during the deployment at Lamont, OK, this model broke down [*Thurairajah 2004*]. The Barrow model had not taken into account the temperature dependence of the atmospheric radiance. This was acceptable due to the low atmospheric temperatures experienced in the Arctic climate of the Barrow, AK, ARM site, but no longer worked in the warm and humid mid-latitude climate of the ARM site at Lamont, OK.

Improving upon the Barrow model, a second model was developed that took into account the temperature of the atmosphere through the easily measurable value of near-surface air temperature [*Thurairajah 2004*]. This correction was built by running a series of MODTRAN simulations for various air temperature values, and for each air temperature various precipitable water vapor levels. For each air temperature range a unique linear fit was found relating precipitable water vapor and the integrated radiance of a clear sky. This work led to the development of the Oklahoma atmospheric radiance model, which used a unique background radiance equation for four different temperature ranges [*Thurairajah 2004*]. Linear interpolation was used to apply these equations to air temperatures between calculated curves. This model is shown in Equations. 2.2 – 2.5.

For air temperature > 25 °C

$$L_{sky} = 4.395wv + 7.88 \quad [\mathrm{W \cdot m^{-2} \cdot sr^{-1}}] \tag{2.2}$$

For air temperature = 15 °C

$$L_{sky} = 3.562wv + 6.731 \quad [\mathrm{W \cdot m^{-2} \cdot sr^{-1}}] \tag{2.3}$$

For air temperature = 0 °C

$$L_{sky} = 2.517wv + 5.559 \quad [\mathrm{W \cdot m^{-2} \cdot sr^{-1}}] \tag{2.4}$$

For air temperature < 0 °C

$$L_{sky} = 1.786wv + 4.448 \quad [\mathrm{W \cdot m^{-2} \cdot sr^{-1}}] \tag{2.5}$$

The Oklahoma model assumed that near-surface air temperature could be used as an indicator of the temperature profile of the atmosphere. This holds true for adiabatic lapse rate conditions, during with the atmospheric temperature drops with altitude in a predictable manner, and the model proved to be accurate during the deployment at Lamont, OK [*Thurairajah and Shaw 2005*]. For most atmospheric conditions this is a valid assumption. However, during conditions such as temperature inversions this is not true and resulting errors may lead to underestimating or overestimating sky radiance.

Methods of Precipitable Water Vapor Measurements

This dependence on precipitable water vapor is one of the limitations of the ICI cloud detection method. This limitation does not hinder the ability of the ICI from operating and producing accurate cloud cover statistics, but it requires that other measurements be available to initialize the water vapor correction algorithm. Precipitable water vapor measurements are not a trivial measurement; however, there exists a wide variety of methods for making the needed measurements. One commonly used and accurate method is the use of microwave radiometers to retrieve an atmospheric liquid and water vapor amount [*Westwater et al. 2001*]. These instruments provide continuous measurements of precipitable water vapor, day and night, fairly independent of local weather conditions. Such an instrument was located at both the Barrow, AK and Lamont, OK ARM sites, which helped facilitate the development of the ICI water vapor radiance correction routines. However, measurements from this type of instrument will not always be available; for example, locations such as the MSU site do not have the convenience of such an instrument.

There exist feasible alternatives to microwave radiometers that can provide water vapor data. Solar radiometers, such as those in the AERONET system, can provide measurements of precipitable water vapor during periods of clear skies in the day [*Holben et al. 1998*], Global Positioning System (GPS) receivers can estimate the precipitable water vapor for clear and cloudy skies [*MacDonald et al. 2002*], and radiosondes (meteorological sensors carried aloft on weather balloons) can measure water vapor profiles that are even better than a simple value of precipitable water vapor. It is becoming common for such instruments to be available at atmospheric measurement sites and at telescope sites used for Earth-space optical communication. GPS-based water vapor measurements are still experimental, but they may be a good alternative for continuous precipitable water vapor measurements in the near future. Solar radiometers and radiosondes are limited in that they cannot produce continuous measurements of precipitable water vapor. Solar radiometers are dependent on an un-obstructed line of sight to the sun, limiting the availability of data during cloudy weather and eliminating data during the night. Radiosondes only produce a single measurement around the time of the launch and are too expensive to launch with high frequency. Therefore if either or both of these methods are used, gaps will exist in the data, quite possibly during the most critical data sets, such as during rapidly changing clouds.

One promising method to fill in the gaps in the solar radiometer, radiosonde, or other non-continuous measurements of precipitable water vapor is to use Reitan's relationship. This relationship allows for the relating of surface dew-point temperature, a relatively easy and readily available measurement, with the total precipitable water vapor contained in the atmosphere [*Reitan 1963*]. The form of this relationship is shown in Equation 2.6. The equation relates the natural log of the total precipitable water vapor, *ln(pwv)*, with the surface dew-point temperature, T_d, through a linear relationship.

$$\ln(pwv) = a + bT_d \tag{2.6}$$

The values of *a* and *b* could be derived using measured precipitable water vapor and dew-point values, preferably over a year or greater. Subsequent research has found that the slope term, *b*, remains constant throughout the year, but the offset term, *a*, varies diurnally and seasonally [*Tomasi 1997*]. Thus, to fill in the gaps of non-continuous measurements, such as from radiosondes or solar radiometers, these accurate precipitable water vapor measurements could be used to update the offset term, *a*, and improve the accuracy of the estimate. Such an estimation routine has been used while processing the ICI data during deployments at the Bozeman, MT and the Poker Flat, AK and are planned to be used during deployments at JPL's Table Mountain Facility..

Need for Camera-Specific Water Vapor Corrections

With the increased field of view of the second-generation ICI systems, the water vapor correction becomes more complicated. The effective water vapor amount present in the atmosphere is dependent on the path length through the atmosphere. This causes a perceived increase in water vapor, and thus an increase of water vapor emission, for angles away from the zenith. For narrow-field-of-view thermal imagers, such as the original ICI, this is not a problem, as the variation with angle over the field of view is small enough it can be ignored. Figure 2-4 demonstrates that the effective path length through the atmosphere increases with zenith angle following a $\cos(\theta)^{-1}$ or $\sec(\theta)$ relationship.

An increase in effective water vapor causes an increase in perceived radiance, particularly near the edge if the ICI's field of view. Figure 2-6 shows a series of MODTRAN simulations of atmospheric emission with increasing zenith angle. These simulations were based on the U.S. 1976 Standard Atmosphere. The majority of the change occurs in the 8 μm to 13 μm region, showing the increase in perceived water vapor, and thus water-vapor-dependent radiance, with increasing angle. This becomes a significant problem for a wide-field-of-view ICI.

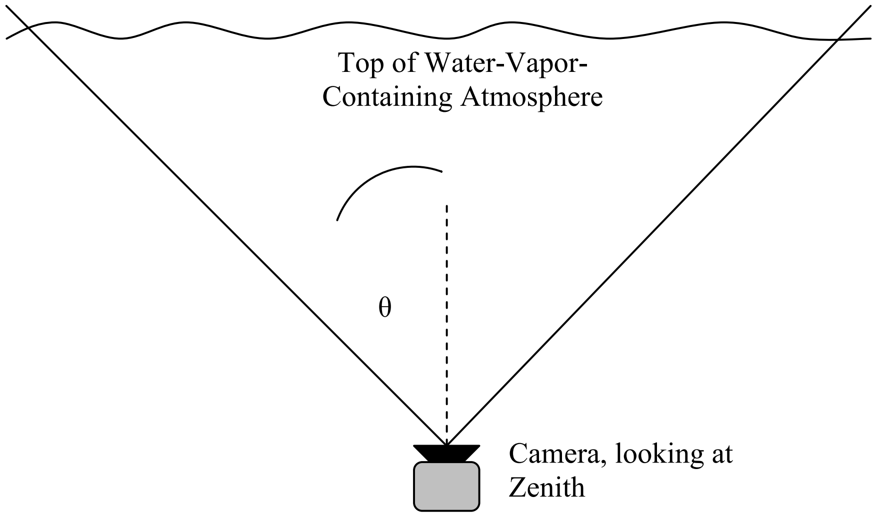

Figure 2-5. For an upward-viewing thermal camera the increasing atmospheric path length with increasing zenith angle causes an increase in perceived radiance.

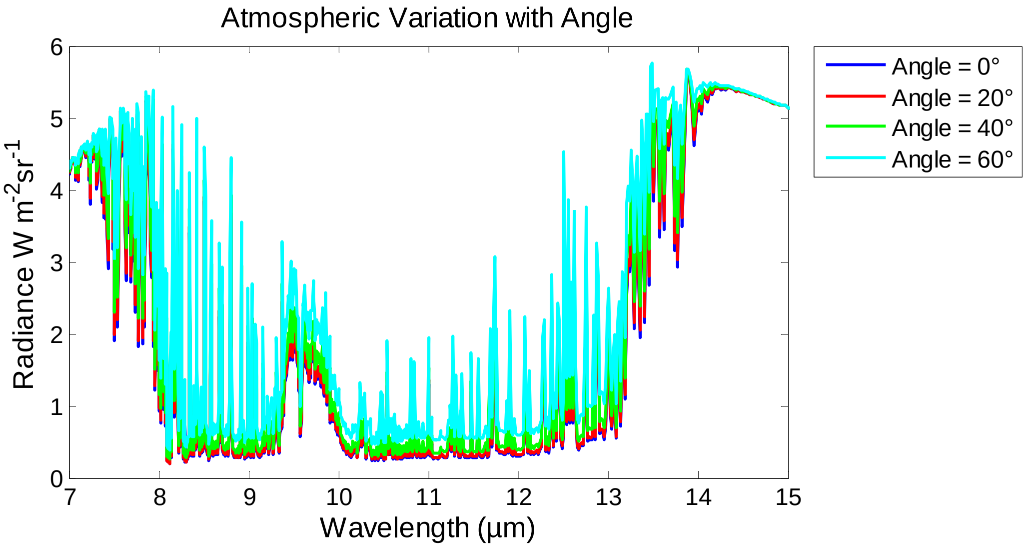

Figure 2-6. The downwelling radiance increases with zenith angle. The majority of the change occurs in the 8 µm to 13 µm region, showing the increase in perceived water vapor with increasing angle.

Better understanding of the magnitude of this error is available by viewing the band-integrated radiance as a function of zenith angle. Figure 2-7 plots band-integrated radiance versus zenith angle. These data were obtained from a MODTRAN simulation with the U.S. 1976 Standard Atmosphere model, assuming a rectangular bandwidth from

7 μm to 15 μm. With increasing angle, the band-integrated radiance is seen to increase. This increase in radiance with zenith angle poses a problem when attempting to remove the background atmospheric radiance.

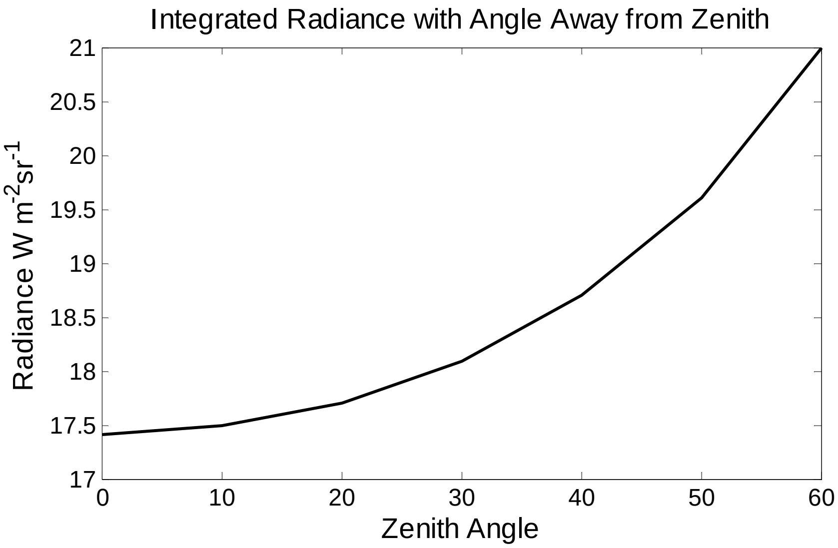

Figure 2-7. Band-integrated radiance plotted versus zenith angle.

The water vapor correction shown in Equation 2.1 and the more robust correction of Equations 2.2 - 2.5 were developed for the first-generation ICI camera, which had a bandwidth of 8 μm to 14 μm and a narrow field of view. For wide-field-of-view cameras, such as those used in this project, the angular dependence of the atmospheric background emission removal routines becomes significant. The concepts behind these corrections were carried over into this project, but new equations were developed for corrections specific to the cameras used in the second-generation ICIs. To build this correction, camera-specific information such as bandwidth and field of view were needed. The following section outlines this information specific to the two cameras used in the two versions of the second-generation ICI, and the development of water-vapor-correction and cloud-detection routines specific to these cameras.

The Photon Core Camera

The Photon Core camera, built by Indigo Systems of FLIR Systems, Inc., was selected as the thermal imaging camera to be used in the development of a second-generation ICI. This camera is a low-cost, small-form-factor, thermal-infrared camera. The selection of this camera was made by the Optical Communications Group at JPL in collaboration with ORSL at MSU as part of their project to measure the overhead clouds at Earth-Space optical communication sites. Two configurations of this camera were used in this project, a semi-wide-angle 50° fov and a wide-angle 100° fov camera. These two configurations of the Photon Core thermal camera are shown in Figure 2-8.

Figure 2-8. The Photon Core thermal cameras built by Indigo Systems: (left) the 50° fov camera, and (right) the 100° fov camera.

These cameras were sent to MSU for testing, characterization, and calibration. The following section describes characteristics required to develop a cloud-detection processing routine based around these cameras. These characteristics include: spectral bandwidth, field of view, and image distortion.

Bandwidth of the 50° fov Photon Camera

The combined bandwidth of the optics, filter, and microbolometer array is specified as nominally 7.5 µm to 14.5 µm. This specification is for an equivalent rectangular bandwidth. The bandwidth of a typical Photon Core camera is shown in Figure 2-9. The actual bandwidth for the total camera system, lens, filter and detector, cannot be easily measured, therefore this typical bandwidth is assumed to be close to that of the actual camera.

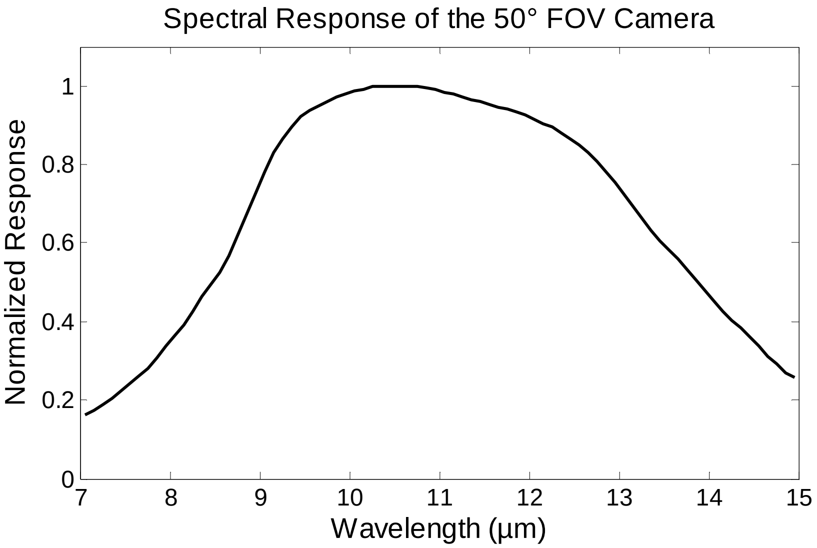

Figure 2-9. Optical bandwidth of a typical Photon Camera. The major response lies within the atmospheric water vapor window, over which water in the atmosphere is the primary emission source.

This camera has low, but significant, response outside the atmospheric window. Although low, this response will effect the operation of the camera and the removal of background atmospheric emission. For example, the camera responds above 14 µm where temperature-dependent CO_2 emission is significant. Near 14.3 μm CO_2 emission and absorption is strong enough that the atmosphere is effectively opaque [*Shaw e. al. 2001*].

The camera also responds below 7.5 μm, where primarily water vapor but also a combination of N_2O and CH_4 provide significant emission [*Stephens 1994*]. This emission is not insignificant but water vapor within the atmospheric window dominates the signal. One advantage of limiting the bandwidth to within the window is that it reduces the temperature dependence of the atmospheric correction. Therefore, the camera's spectral response plays a role in determining the expected background radiation needed to establish a background-radiance-removal algorithm, allowing for a cloud-detection threshold.

Bandwidth of the 100° fov Photon Camera

With the addition of the after-market lens, the combined spectral bandwidth of the optics, filter, and microbolometer array is specified as nominally 8.5 μm to 13 μm. Measurement of the full combined bandwidth of the optics, filter, and microbolometer array with the aftermarket 100° fov lens was not feasible at MSU. However, the capability to measure the bandwidth of just the lens alone did exist. This allowed for the measurement of bandwidth for the original 50° fov and the 100° fov lenses.

To estimate a spectral response function for the camera without lens, the bandwidth of the 50° fov lens was divided out of the response specified for the camera and standard lens, shown in Figure 2-9. The bandwidth of the 100° fov lens was then multiplied by this approximate lens-less camera response. The yielded an estimate of the response of the camera with the aftermarket 100° fov lens. The camera response with the lens is shown in Figure 2-10.

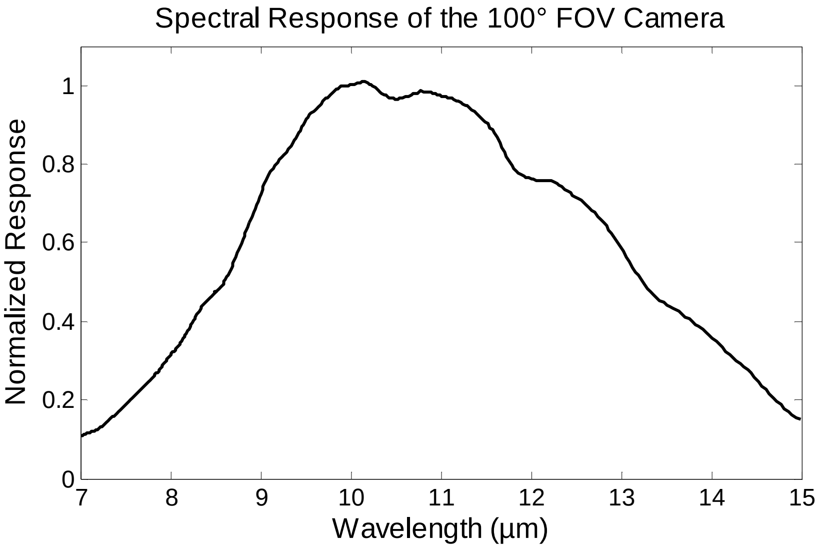

Figure 2-10. The estimated bandwidth of the Photon Camera with the after-market 100° fov lens.

Mapping Each Camera's Per-Pixel Field of View

Increasing the field of view for the camera introduced problems that needed to be overcome to develop an accurate cloud detection algorithm. As part of this processing, an accurate characterization of each camera's field of view was needed. This characterization needed to include the per-pixel pointing angle and instantaneous field of view (ifov). This measurement therefore must characterize the camera's full field of view and the distortion present in the imaging system.

These measurements are needed for a variety of reasons. First, this information was needed for the angular dependence of the water vapor removal algorithms. The pointing angle and ifov are also needed for accurate calculation of angle-dependent cloud coverage statistics. This is needed to remove the dependence cloud cover statistics have on the angular location in the camera's field of view [*Kassinov et al 2005*]. For zenith angles greater than 50° it becomes increasingly difficult to remove the dependence of cloud cover statistics on the position of the cloud in the imager’s fov. For a fov half-angle less than 60°, derivation of the actual sky cloud fraction is possible, but for greater angles the accuracy of such a correction breaks down [*Kassianov et al. 2005*]. Angular information is also needed for characterization of optical communication paths, as a specific communication channel may be located at a fixed angle or may sweep across the sky. Thus, to properly track such a channel across the camera's field of view the pointing angle of each pixel would be needed.

Measuring the field of view and distortion present in a thermal imaging system is not as straight forward as a similar measurement for a visible-wavelength camera. To measure the distortion in a visible-wavelength camera a grid pattern is often used. This allows for a simultaneous measurement of the distortion across the camera's field of view. Building such a pattern in the thermal infrared would require a pattern of heated bars or wires with thermal isolation between these heated elements and the spaces between. Also these cameras are focused at a hyper-focal distance, meaning that for such a pattern to be in focus, the grid would need to be at a distance of five meters. This would dictate an impractical pattern ten meters across when using the 100° fov camera.

A solution to this difficulty was to make these measurements by imaging a straight edge as it was scanned a known angular distance across the camera’s fov. Once these images were taken, a polynomial fit was found for the edge at each angular location. This kind of measurement was taken in both the horizontal and vertical axis of the camera. Using these equal-angle lines across the camera's field of view, the pointing angle of each pixel could be determined. The measurements taken during this experiment are shown in Figure 2-11for the 50° fov camera, and Figure 2-12 for the 100° fov camera.

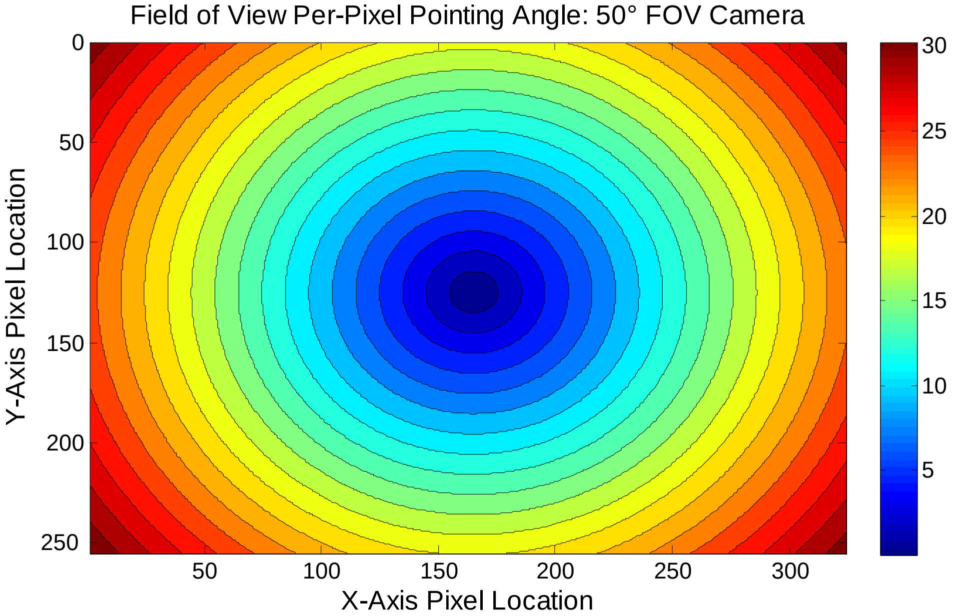

Figure 2-11. The full-fov per-pixel pointing angle for the 50° fov camera.

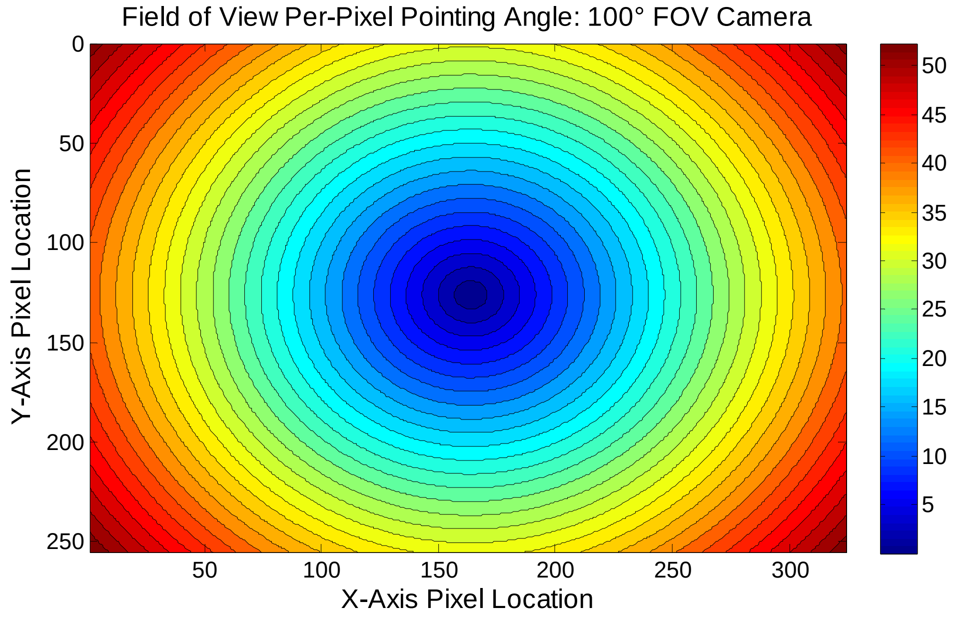

Figure 2-12. The full-fov per-pixel pointing angle for the 100° fov camera.

Camera-Specific Data Processing and Cloud Detection

With the mentioned camera properties, the necessary components were available to build a cloud-detection algorithm specific to each of the two cameras used in the second-generation ICI systems. This processing routine has been highly expanded from the original ICI routine. This is primarily due to the differing bandwidth and fields of view of the two second-generation ICI cameras. Also the cloud-threshold routine has been expanded to allow for the detection of cloud presence, along with cloud type. The flow diagram for the new expanded detection scheme is shown in Figure 2-13.

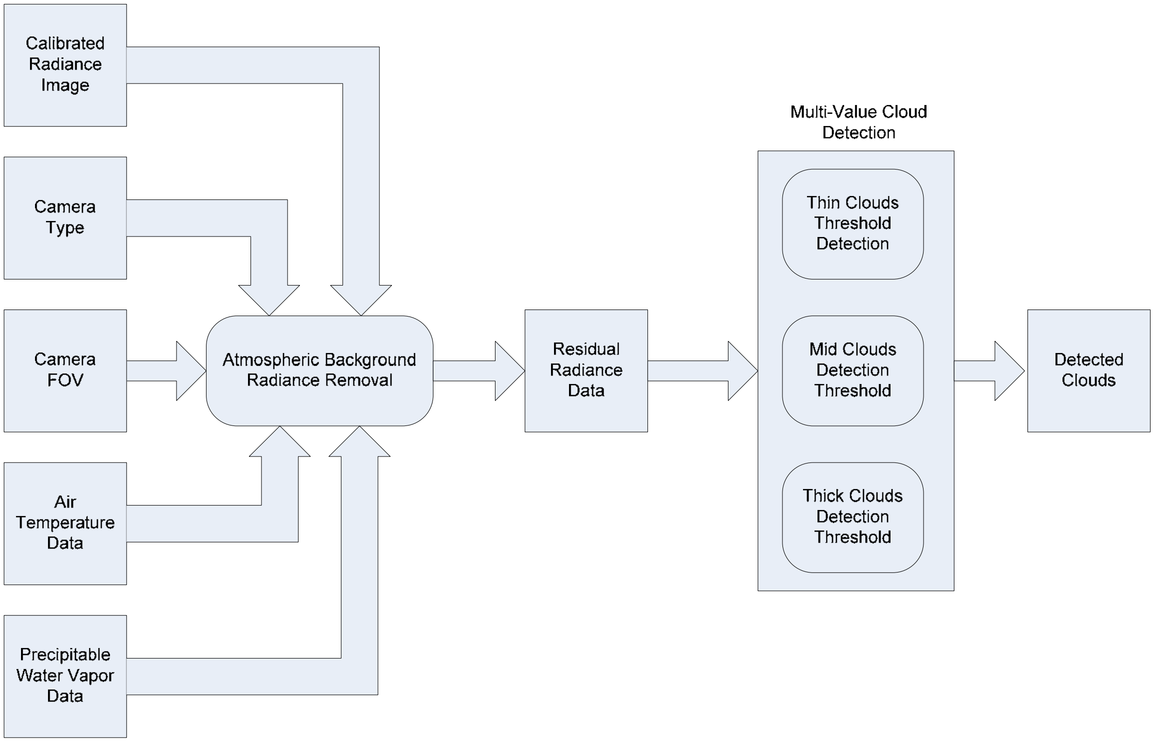

Figure 2-13. The updated processing routine used for the second-generation ICI.

Extended Water Vapor Correction

To build a realistic water vapor correction algorithm for the wide-angle cameras, a collection of all the radiosonde data collected at MSU from 2004 through 2007 was used as the model atmosphere inputs into MODTRAN for atmospheric emission simulations for a zenith path. Each simulation calculated the emitted clear sky radiance over the 7 µm to 15 µm band. These radiosondes had been launched at various times throughout the year, and thus provided a distribution of near-surface air temperature measurements from -5 °C to 35 °C. For each of these atmospheres the precipitable water vapor was varied from 0.1 g cm^{-2} to 3.5 g cm^{-2}, using the water vapor scaling functions in MODTRAN.

Once these simulations had been run, the emission spectra were scaled by the camera's spectral response function. After scaling by each camera's response, the radiance across the 7 µm to 15 µm band was integrated. This band-integrated radiance is representative of the values that would be measured by a calibrated camera. A two-dimensional fit was calculated for these data. This fit gives an empirical equation that relates near-surface air temperature and precipitable water vapor as input variables to the camera-weighted integrated atmospheric radiance of a clear sky as the output. These simulations and the following data fits were calculated using the camera response of the 50° fov and 100° fov cameras. The integrated radiance from the simulations and the values calculated from the fit using the 50° fov camera are shown in Figure 2-14, and the two-dimensional fit to the data is shown in Equation 2.7. The calculated value for these simulations and the values calculated from the fit using the 100° fov camera are shown in Figure 2-15, and the resulting empirical equation is shown in Equation 2.8.

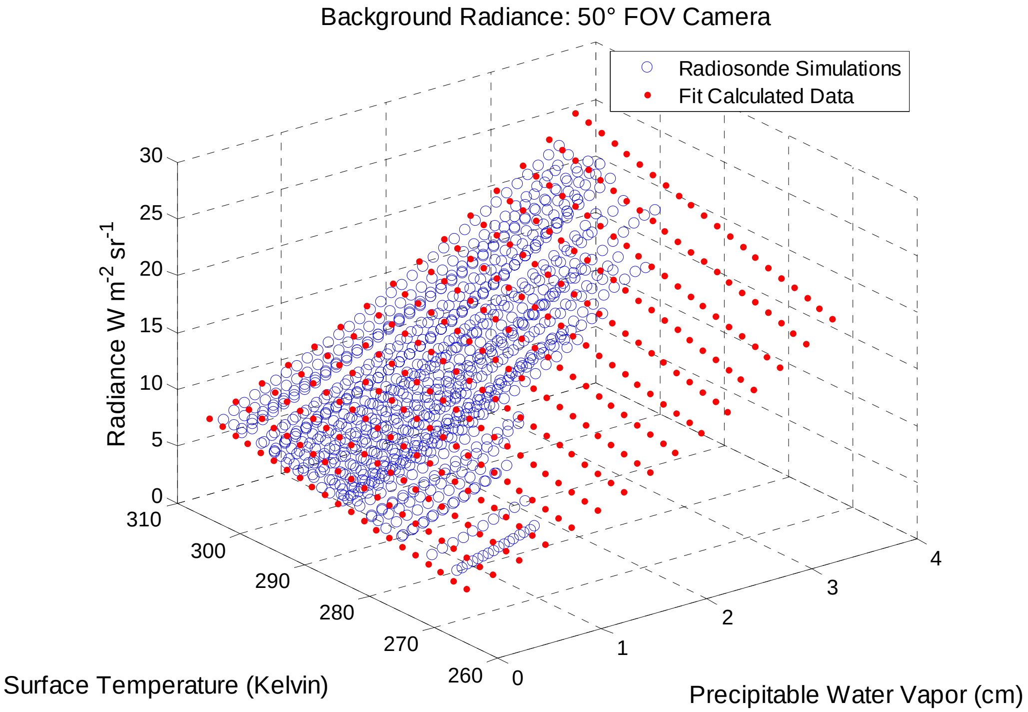

Figure 2-14. Background atmospheric radiance for the 50° fov camera calculated for a set of radiosondes with varying near-surface air temperature and precipitable water vapor (blue circles). The red dots represent data calculated with an empirical fit to the data.

$$L_{sky50^o} = 0.5383 pwv^2 + 0.0223 T_k pwv - 3.6365 pwv + 0.1018 T_k - 22.197 \text{ [W·m}^{-2}\text{·sr}^{-1}] \tag{2.7}$$

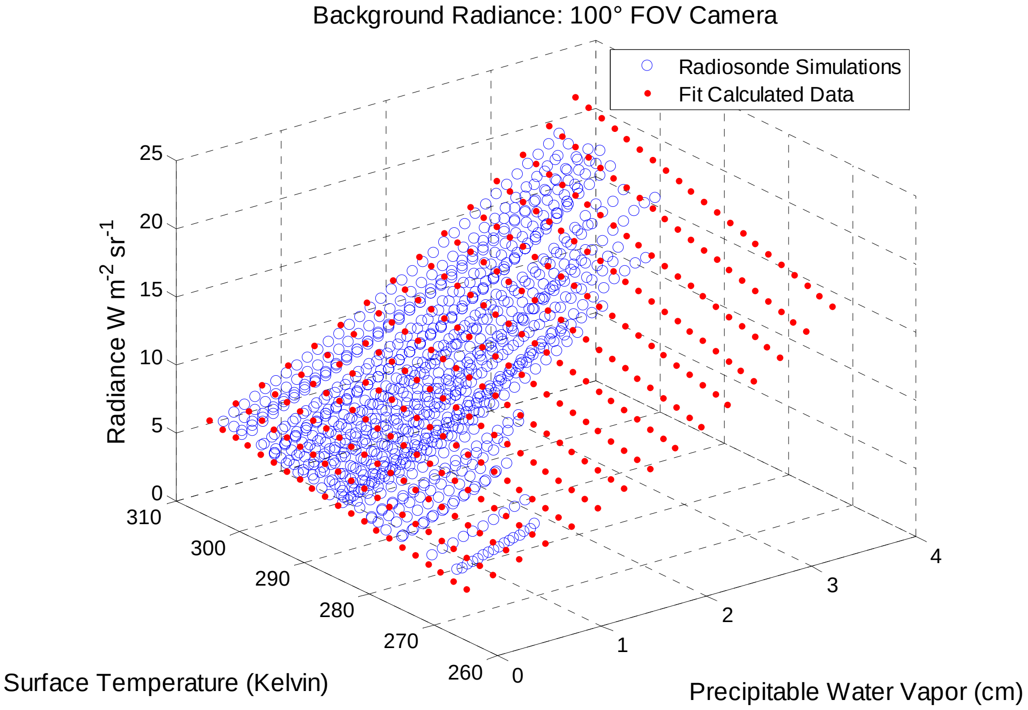

Figure 2-15. Background atmospheric radiance for the 100° fov camera, calculated for a set of radiosondes with varying near-surface air temperature and precipitable water vapor (blue circles). The red dots represent data calculated with an empirical fit to the data.

$$L_{sky100^o} = 0.5164 pwv^2 + 0.0209 T_k pwv - 3.5897 pwv + 0.0811 T_k - 17.6704 \, [\mathrm{W \cdot m^{-2} \cdot sr^{-1}}] \tag{2.8}$$

Angle-Dependent Water Vapor Correction

The variation in the background radiance can largely be corrected by scaling the water vapor by the path-length variation based on each pixel's pointing angle. This path length dependence causes a $[\cos(\theta)]^{-1}$, or $\sec(\theta)$, correction to the water vapor amount. Simulations using MODTRAN were developed to simulate sky radiance with increasing zenith angle using the U.S. 1976 Standard Atmosphere. Then this emission was integrated across the bandwidth of each camera. To remove the atmospheric background radiance, the sky radiance equation developed for each camera, Equations 2.7 and 2.8, were used, but with a $[\cos(\theta)]^{-1}$ added to the precipitable water vapor term. The simulations using the 50° fov camera bandwidth are shown in Figure 2-16, and the corresponding sky radiance equation in Equation 2.9. Similar simulations using the 100° fov camera bandwidth are shown in Figure 2-17, and the corresponding sky radiance equation in Equation 2.10.

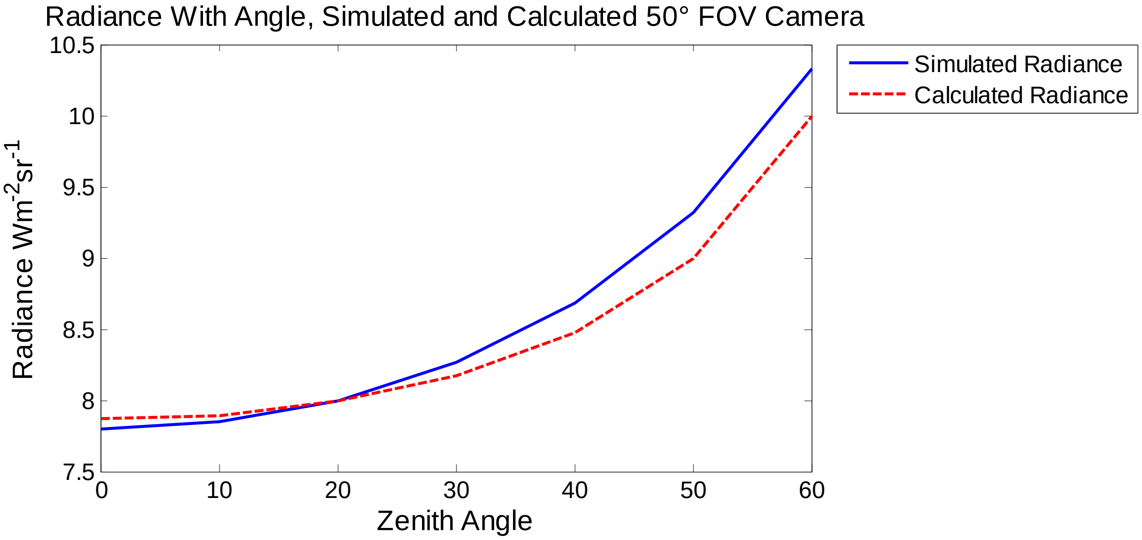

Figure 2-16. Integrated Radiance using the 50° fov camera bandwidth, with increasing angle from the zenith, both simulated with MODTRAN and calculated using Equation 2.9.

$$L_{sky50^o} = 0.5383\left(\frac{pwv}{\cos\theta}\right)^2 + 0.0223T_k\left(\frac{pwv}{\cos\theta}\right) - 3.6365\left(\frac{pwv}{\cos\theta}\right) + 0.1018T_k - 22.197 \tag{2.9}$$

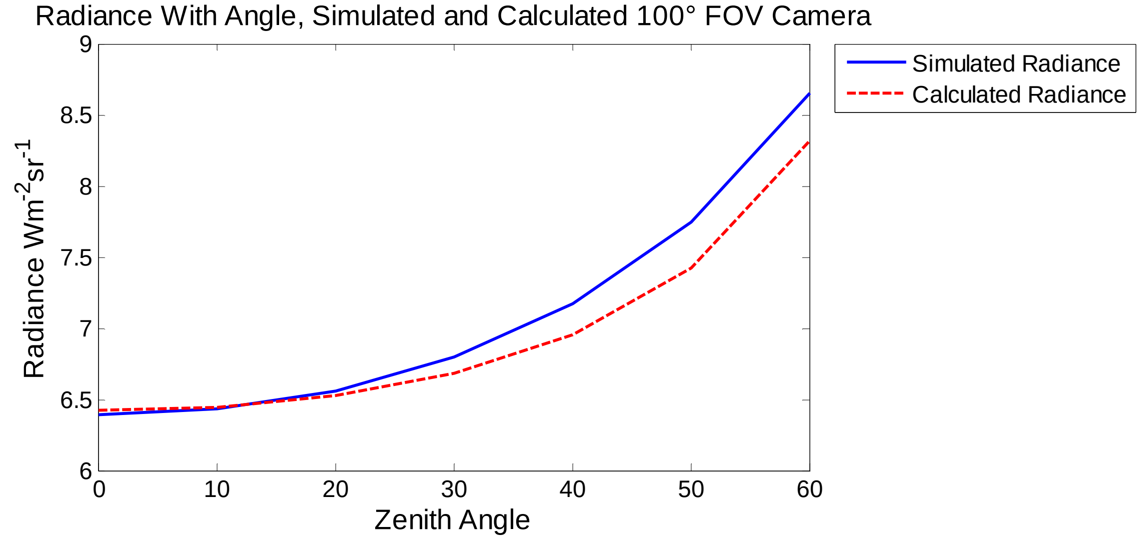

Figure 2-17. Integrated Radiance using the 100° fov camera bandwidth, with increasing angle from the zenith, both simulated with MODTRAN and calculated using Equation 2.9.

$$L_{sky100^{o}} = 0.5164\left(\frac{pwv}{\cos\theta}\right)^{2} + 0.0209T_{k}\left(\frac{pwv}{\cos\theta}\right) - 3.5897\left(\frac{pwv}{\cos\theta}\right) + 0.0811T_{k} - 17.6704 \tag{2.10}$$

Figures 1-26 and 2-17 show that only accounting for the path length change and scaling the precipitable water vapor does not fully account for the radiance variation seen over the camera's field of view. This may be due to the fact that the sky radiance calculation equation does not account for the temperature profile of the atmosphere. By using a combination of radiosonde profiles this equation is for an average Bozeman atmosphere and certainly contains some profiles that have temperature inversions, and thus have higher than normal radiance. Simply accounting for the increasing precipitable water vapor allows for an accurate sky radiance calculation within 0.25 W·m^{-2}·sr^{-1} or less over the camera's entire field of view. For the initial processing presented here, this is accepted. More robust calculation of this relationship will be required in the future.

Threshold-Based Cloud Detection with Simulated Data

With the fov-dependent atmospheric radiance equations in hand, the images can be processed. Once the water vapor has been scaled, the atmospheric radiance can be calculated and subtracted from the calibrated image in a per-pixel manner. Once removed, a threshold can be applied to the image to determine cloud presence and cloud type. To demonstrate this capability, cloud images were simulated by running MODTRAN at the angle of each pixel. To start, spatial cloud templates were made. These black-and-white images had four levels representing clear sky, cirrus clouds, altostratus clouds, and cumulus clouds. Calibrated sky images were simulated for each camera using these black-and-white cloud templates (to indicate cloud type in each pixel), the measured camera field of view, and the MODTRAN calculations for a 1976 U.S. Standard Atmosphere. This simulated sky radiance image is the left-most panel of each figure. For this image the clear-sky atmospheric radiance was calculated using the precipitable water-vapor and near-surface air-temperature from the 1976 U.S. Standard Atmosphere model. This radiance was subtracted from the sky radiance image to give a residual radiance image, shown in the center panel of the figures. To the residual radiance image a multi-level threshold was applied to determine cloud presence and cloud type. This gave a cloud mask, the right-most panel of each figure. These clouds masks could be compared with the original templates to determine the effectiveness of these algorithms.

These simulations were conducted for two cloud templates. The first was thin cirrus clouds with extinction coefficient of 0.5 with a cloud base at 9 km and a thickness of 200 m (550 nm optical depth of 0.1). The processing results with this simulated cloud are shown for the 50° fov camera in Figure 2-18, and for the 100° fov camera in 2-19.

The second simulation set contained three cloud types: thin cirrus clouds with the same parameters as before, altostratus clouds with a cloud base at 2.4 km, a cloud top at 3 km, and an extinction coefficient of 128.1 (550 nm optical depth of 77), and cumulus clouds with a cloud base at 0.066 km, a cloud top at 3 km, and an extinction coefficient of 92.6 (550 nm optical depth of 272). The processed results of these simulations are shown in Figure 2-20 for the 50° fov camera, and Figure 2-21 for the 100° fov camera. The cloud detection thresholds used for these results were: level 1, subvisual cirrus clouds (0.8 $W\cdot m^{-2}\cdot sr^{-1}$), level 2, thin cirrus clouds (2 $W\cdot m^{-2}\cdot sr^{-1}$), level 3, cirrus clouds (5 $W\cdot m^{-2}\cdot sr^{-1}$), level 4, mid-level clouds (10 $W\cdot m^{-2}\cdot sr^{-1}$), 1evel 5, thick mid-level clouds (15 $W\cdot m^{-2}\cdot sr^{-1}$), level 6, thick low-level clouds (22 $W\cdot m^{-2}\cdot sr^{-1}$).

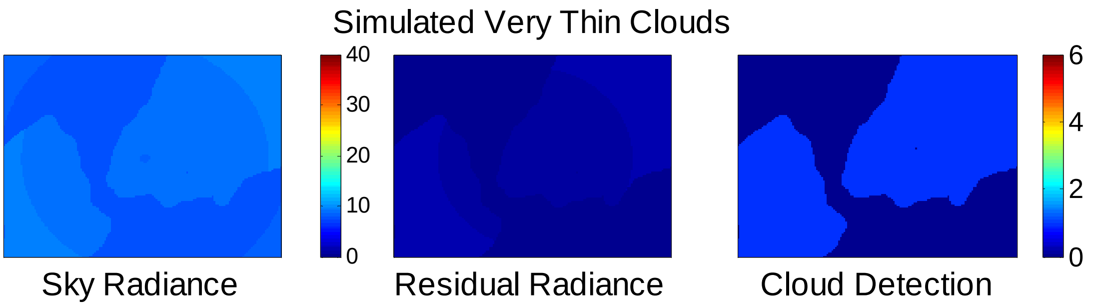
Simulated Very Thin Clouds

Sky Radiance
Residual Radiance
Cloud Detection

Figure 2-18. Simulated clouds for the 50° fov camera. The three panels show sky and cloud radiance (right panel), residual radiance after removing atmospheric emission (center panel), and actual cloud presence and type (left panel).

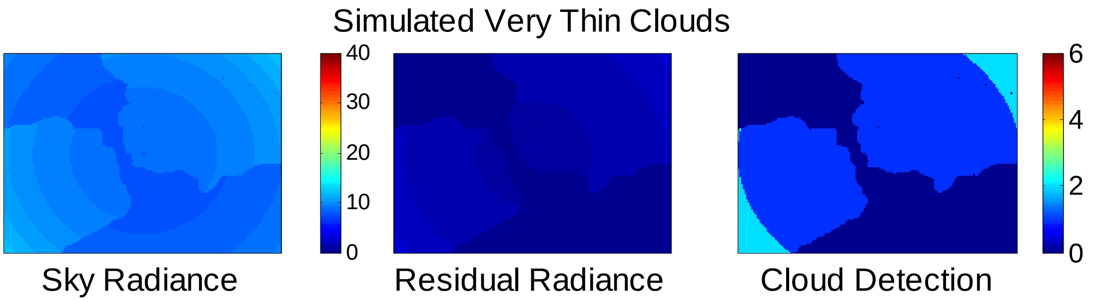
Simulated Very Thin Clouds

Sky Radiance
Residual Radiance
Cloud Detection

Figure 2-19. Simulated clouds detected with the 100° fov camera's bandwidth. In This case an error occurs where very thin cirrus clouds (level 1 clouds) are mis-identified as thin cirrus (level 2 clouds) near the image corners.

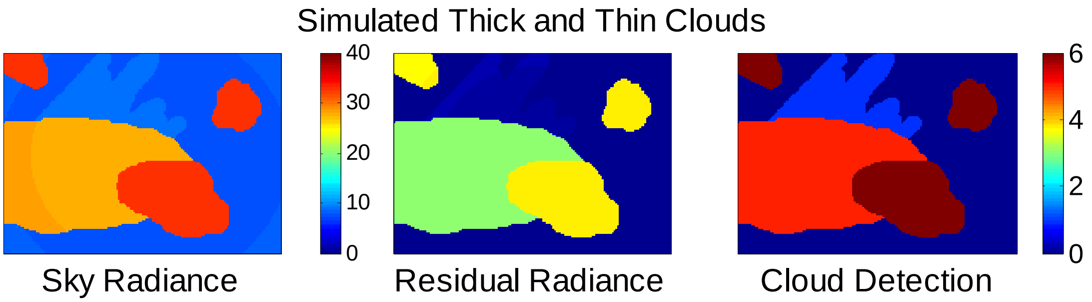

Figure 2-20. Simulated thick and thin clouds detected with the 50° fov camera's bandwidth. In this case the advantage of a radiometric calibration is apparent in that the cloud-detection algorithm has no problem identifying the different cloud types, even if the cloud layers are overlapping.

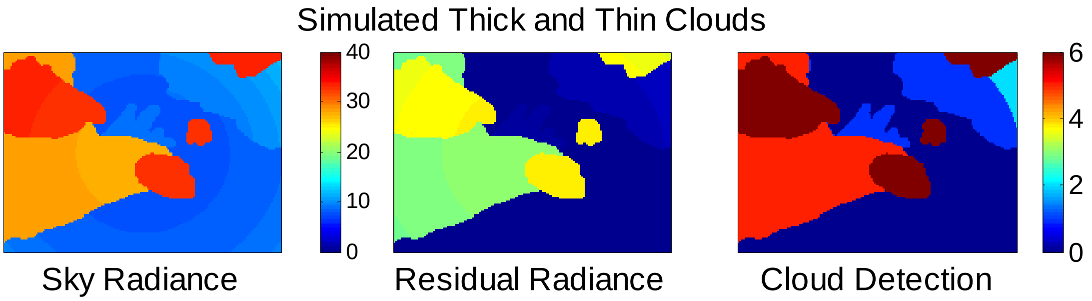

Figure 2-21. Simulated thick and thin clouds detected with the 100° fov camera's bandwidth. Again as in the cirrus-only case, the very thin cirrus clouds are mis-identified near the corner of the image, corresponding to large zenith angles.

Optically thin cirrus clouds pose a problem for cloud-type classification by thermal imaging systems if the field of view is sufficiently wide. In optically thin clouds, such as the cloud of extinction coefficient 0.5 used in these simulations, The ICI systems can see through the cloud layer. Thus, the optical path through the cloud, or the effective cloud thickness, increases for increasing angles away from the zenith. This is very similar to the effective water vapor path demonstrated in Figure 2-5. For these clouds the effective thickness of the cloud increases, and thus the level of thermal emission from the cloud increases. For optically thick clouds this is not a problem as the imager does not see through the cloud. Thus, to develop an accurate detection method for optically thin cirrus clouds, a field-of-view-dependent correction may need to be applied when thin clouds are detected.

Overall the ICI cloud detection method has been effectively extended to account for the increased field of view for the second-generation ICI cameras. This has required the development extended processing techniques based on the techniques developed for the original ICI system. These extensions are primarily required by the angular dependence of atmospheric emission. The improvement of these techniques has extended the capabilities of this system to include the capability to classify the overhead clouds into multiple cloud types. This should improve the ability of the ICI systems to provide the desired data for both optical communications and climate research.

PHOTON CORE CAMERA CALIBRATION

The Infrared Cloud Imager (ICI) instruments are calibrated to produce a radiometric measurement of the down-welling atmospheric and cloud radiance. The purpose behind this calibration is two-fold. Radiometric calibration allows for the removal of the emission from the atmosphere, thereby isolating the cloud signature [*Thurairajah and Shaw 2005, Shaw et al. 2005*]. The second reason is that a radiometric calibration allows for the measurement of cloud properties such as cloud type.

Introduction to Radiometric Calibration

As mentioned in the previous chapter these calibrations were conducted to provide measurements of scene radiance, not scene temperature. This is opposed to the method common to industrial thermal imagers of calibration in a temperature space, which provides an approximate measurement of scene temperature. Thermal radiance (in $W \cdot m^{-2} \cdot sr^{-1}$) has been selected as the preferred method for this project for both engineering and scientific reasons.

The first reason for a radiometric calibration has to do with the physics of the objects under study. Perfect blackbodies are a non-realistic radiator which emits with a power spectrum that perfectly fits the Planck blackbody radiation equation [*Planck 1932*], shown in Equation 3.1.

$$L(\lambda) = \frac{2hc^2}{\lambda^5} \frac{1}{e^{\frac{hc}{\lambda kT}} - 1} \quad [W \cdot m^{-2} \cdot sr^{-1} \cdot m^{-1}] \tag{3.1}$$

In this equation: $L(\lambda)$ is the radiance emitted from an object at wavelength λ, the constant $h = 6.6260\text{x}10^{-34}$ J·s is Plank's constant, the constant c is the in vacuum speed of light, the constant $k = 1.381\text{x}10^{-23}$ J·K^{-1} is known as Boltzmann's constant, and the variable T is the temperature of the object in Kelvin. With natural objects, such as the overhead clouds and sky, this criterion of perfect Planck radiation is rarely met. Therefore, the energy from the object will always be less than predicted by the Planck equation. The ratio between the energy from a perfect radiator and a perfect Planck blackbody defines the emissivity of the object. Most objects have an emissivity less than one, and thus when viewed over a significant bandwidth they appear to emit the equivalent energy of a blackbody at a temperature lower than the actual temperature of the object (the "brightness temperature"). Thus, to make an accurate temperature measurement, the emissivity of the object being measured needs to be known. Working in a radiometric sense avoids this problem, as radiance is a direct measurement of the energy emitted from the object.

From an engineering standpoint, a radiometric calibration is preferable. This is because, although these cameras can be considered temperature-sensing cameras, the response of the detector is linear with incident power, and thus scene radiance, not temperature. Figure 3-1 shows a band-integrated radiance emitted for a perfect blackbody over a wide range of temperatures. For these data the signal was integrated over a 7 μm to 15 μm wavelength range. The relationship between the emitted energy due to thermal emission and temperature of the emitting object is not a linear relationship. This curve is approximately linear over a narrow region, allowing for a direct temperature calibration.

The dynamic range expected from overhead sky measurements require the imager to be calibrated in a radiometric and not a thermometric sense.

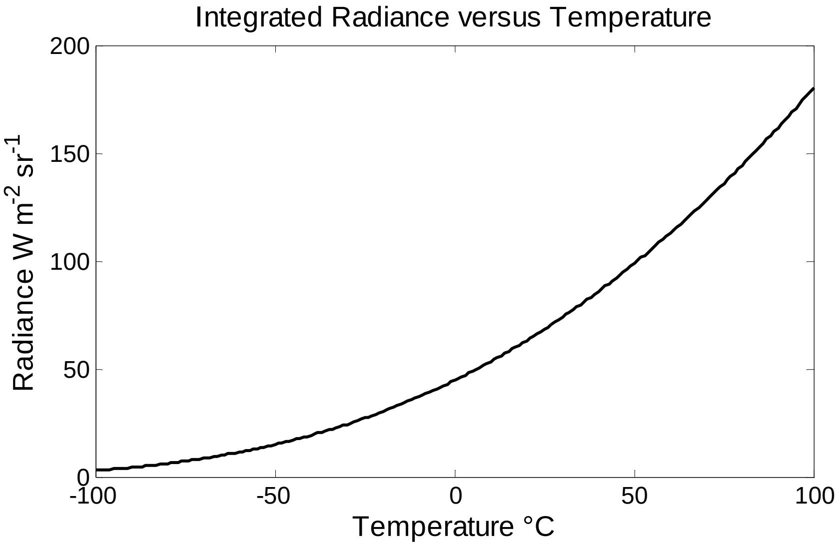

Figure 3-1. Integrated Radiance from 7 μm to 15 μm for a perfect blackbody over a temperature range from -100 °C to 100 °C. The non-linear relationship between energy emitted from an object and temperature can be seen.

For these reasons, along with reasons related to cloud processing discussed in the previous chapter, the ICI instruments have been designed to operate in a radiometric calibrated mode. Due to this radiometric calibration, when a camera output is referred to it will be referred to as digital number (D#) in the case of uncalibrated data, or as radiance ($W \cdot m^{-2} \cdot sr^{-1}$) in the calibrated data. When temperature is referred to, it is either talking about the temperature set point on a blackbody calibration target, or the internal temperature of the camera, and not the temperature of a scene or measured output from the camera.

The Camera Radiance to Digital Number Function

The method for calibrating a system such as this camera can be explained by viewing the system as a function which takes in the current scene radiance and the properties of the camera, and outputs a digital number. This number represents the signal on the detector, but is not a direct absolute measurement of scene radiance. Figure 3-2 shows a block diagram of the camera from this perspective. All the properties of the camera that determines how scene radiance is transferred into a digital number are contained within this *S(L)* camera function, where *L* is the scene radiance.

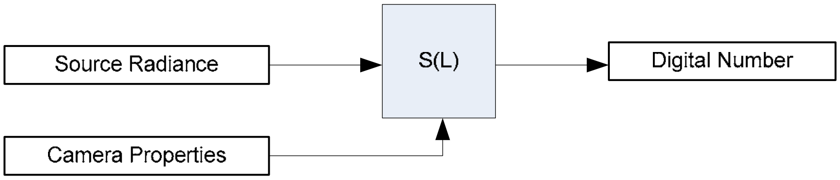

Figure 3-2. The block diagram of the camera viewed as a function with scene radiance and the camera properties as inputs and a digital number as an output.

The variables included in the camera properties are such parameters as the camera digitization settings, camera optical properties, random drift in the camera offset or gain, temperature of the detector array, and other unknown parameters. If these parameters are measured, or if their effect on the system is measured, a calibration function can be developed to produce a measurement of the scene radiance integrated across the camera's bandwidth. This is the method of calibration was used to calibrate these cameras. Such a system with a calibration function, *C(D#)*, added in line with the data flow is shown in Figure 3-3. This system allows for the measurement of scene radiance integrated across the camera's bandwidth.

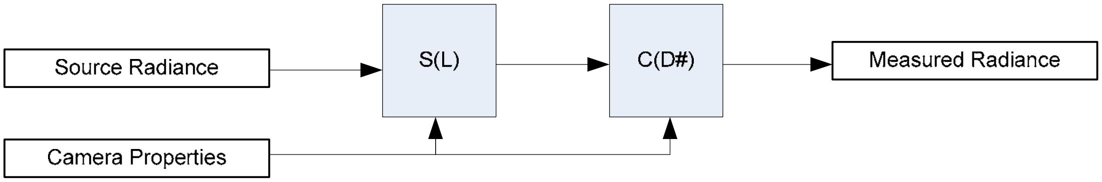

Figure 3-3. The block diagram of a calibrated camera. *S(L)* converts scene radiance to a digital number and *C(L)*, the calibration, takes digital number and gives a measured radiance.

Calibration for the First-Generation ICI Systems

Characterization of the *S(L)* function for the first-generation ICI was conducted through a unique two-point blackbody calibration for each sky image. Two blackbody calibration targets were viewed in series with each image of the sky. From these two points a linear calibration equation was derived, relating output digital values from the camera to the scene radiance. During the first-generation ICI calibrations, one of these calibration targets was set to 50 °C and the other was allowed to drift at ambient, but the instantaneous temperature of this ambient blackbody was measurable. These two calibration targets allowed for a two-point calibration as shown in Figure 3-4. The blackbody radiance at the temperature of each calibration target was calculated by integrating the Planck equation over a camera bandwidth. However, the blackbodies used in these calibrations had a high but non-unity emissivity of 0.995. Thus, the observed signal from the calibration target is 99.5% of the blackbody target radiance and 0.05% of the reflected background radiance. Therefore, the actual observed radiance from the blackbody was determined using a calculated background radiance and Equation 3.2.

$$L_{Actual} = 0.995 L_{BB} + (1 - 0.995) L_{AMB} \quad [\mathrm{W \cdot m^{-2} \cdot sr^{-1}}] \tag{3.2}$$

This equation accounts for the non-ideal emission from the blackbody calibration target and for the reflectance term. In this equation L_{Actual} is the actual measured radiance, L_{BB} is the radiance of a perfect blackbody at the temperature of the calibration target, integrated from 8 µm to 14 µm, and L_{AMB} is the radiance of the ambient background integrated over this same bandwidth. For the ambient calibration target this non-ideal emission is not an issue, as the target and background radiance are approximately the same and thus can be ignored. However, for the 50 °C blackbody case, this non-ideal emissivity had to be considered. With these two radiance calculations and associated calibration images, a full two-point linear calibration could be calculated on a per-pixel basis. An example of such a calibration is shown in Figure 3-4 and a resulting calibration equation in Equation 3.3, where m is the "gain" and b is the "offset" for the linear calibration equation.

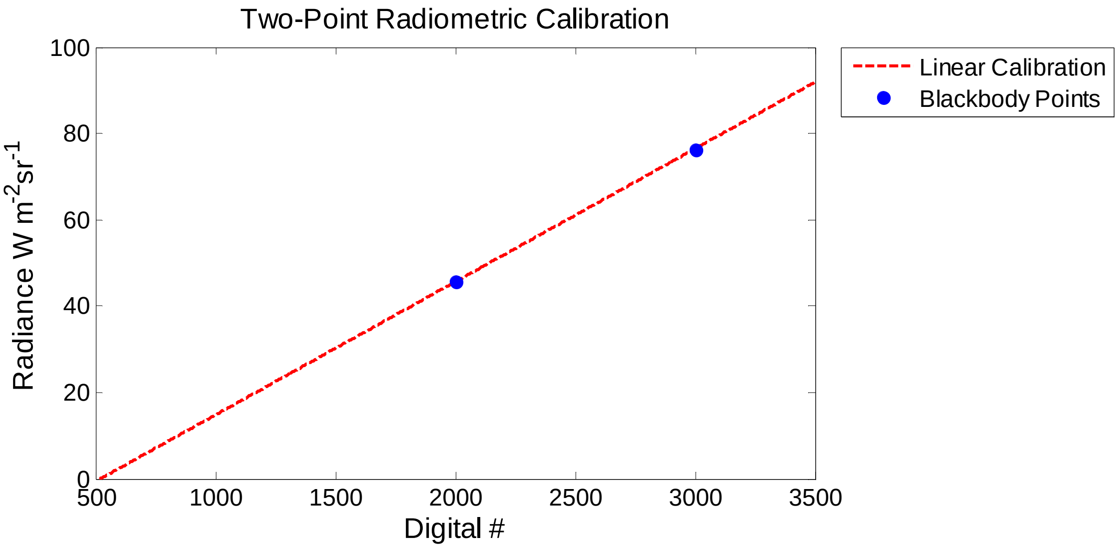

Figure 3-4. An example linear calibration using two blackbody radiances.

$$L_{Sky} = mD\#_{Sky} + b \quad [\mathrm{W \cdot m^{-2} \cdot sr^{-1}}] \tag{3.3}$$

Calibration for the Second-Generation ICI Systems

Performing a unique two-point calibration for each individual sky image, as done in the first-generation ICI, required that two blackbody calibration targets needed to be sent into the field as part of the ICI system. These calibration targets were the largest components of the first-generation ICI. Therefore, it was determined from the beginning of this project to try to run with as few of these targets as possible. To accomplish this goal, a different calibration process was needed.

Two different methods have been used to perform calibrations in this project. The first method was similar to the first-generation ICI and two different blackbody radiance standards were used to produce a linear calibration curve defined by unique offset and gain terms. However, the two references were obtained from one blackbody by cycling the blackbody temperature between two points with a four-hour period. This required that the camera's transfer function remain stable over this time period. To accomplish this, response changes due to temperature changes on the camera's focal plane array (FPA) needed to be characterized and removed. This characterization is discussed in the following sections. The second method was to use a laboratory calibration, based on a series of blackbody reference images to calibrate the gain of the camera, and use the shutter of the camera as a real-time calibration source to determine the offset term during deployment. This calibration relied on the validity of three assumptions: 1) the camera's gain remains acceptably stable with time, 2) the shutter is at the same temperature as the camera's FPA where an internal temperature reading is available, and 3) any radiometric differences between viewing a blackbody through the lens and viewing the shutter without the lens could be characterized. This second method has been used during the extended deployments of the camera, such as the deployment at JPL’s Table Mountain Facility (TMF), and during the second deployment at Bozeman, MT during summer 2007.

The details of these calibration methods are described in the following section. It is important to note that for each step the calibration is constructed on a per-pixel basis, with each pixel having a unique calibration. It is not practical to present an equation here for each pixel due to the 82,944 pixels in the detector array. Therefore, when calibration equations are presented with numbers, they are meant to represent the mean across the detector array and not the unique calibration for each pixel.

FPA Temperature-Dependent Data Drift

The Photon camera has been designed to operate without a temperature-stabilized detector, although usually a thermo-electric cooler / heater (TEC) is used to stabilize the detector temperature in microbolometer cameras. This allows the detector focal plane array (FPA) to drift with changes in camera temperature, which tends to follow the ambient temperature. This drift posed a problem for radiometrically calibrating the camera. The drift in FPA temperature produces a drift in the output digital data. Experimentally, it was found that for an increase in the camera FPA temperature there was a decrease in digital number detected from a constant-radiance scene produced with a constant temperature blackbody. Similarly, a decrease in camera FPA temperature caused an increase in the digital number output, again while viewing a constant-radiance scene.

Temperature-Dependent Camera Function

These changes are related to the FPA temperature dependence. This can be represented by separating the camera's radiance-to-digital-number function *S(L)* in two parts: a temperature-independent *s(L)* and a temperature-dependent *s(T)*. Such a two-part function, dependent on scene radiance and camera temperature, is shown in Figure 3-5.

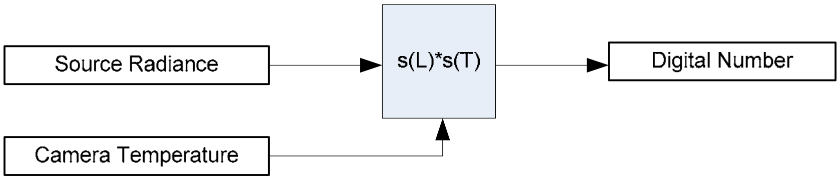

Figure 3-5. Block diagram of a TEC-less camera with the output digital number dependent on scene radiance and the temperature of the camera's detector.

With characterization of the FPA temperature-dependent variation in the output, a post-processing routine can be applied for correcting the output and removing the FPA temperature dependence. Figure 3-6 shows such a system's camera function, in which the impact of *s(T)* on the output digital data has been measured and a correction, $C_T(T)$, has been applied. With this correction, the system dependence on FPA temperature can be greatly reduced if not removed entirely. The level to which the FPA temperature dependence can be corrected depends on the level to which this dependence can be separated from all other components of the camera function.

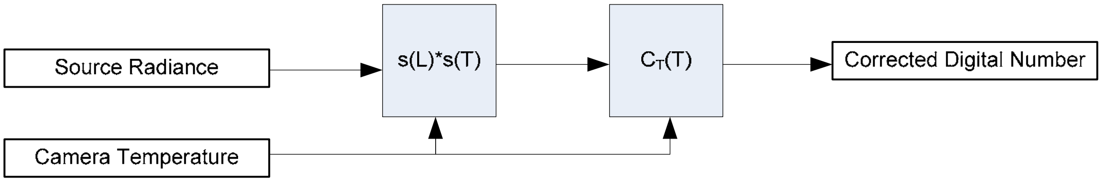

Figure 3-6. The block diagram of a TEC-less camera corrected to compensate for the dependence on the temperature of the detector.

Data Error Related to Camera FPA Temperature

The initial characterization of the relationship between the drift in the digital output with camera temperature took place with the 50° fov camera during summer 2006. To make this characterization the camera was placed in a temperature-controlled chamber that could provide air temperature stabilized to ±0.3 °C. The camera and three blackbody sources at 60 °C, 40 °C, and 20 °C were placed inside the chamber and the temperature was cycled. Each blackbody source filled a portion of the camera's field of view and was controlled to maintain a constant temperature as the thermal-chamber temperature was cycled. The temperature of the camera was monitored by five thermo-couple probes placed at various locations on the camera body. Changes in the camera temperature caused a significant variation in the digital output, as shown in Figure 3-7.

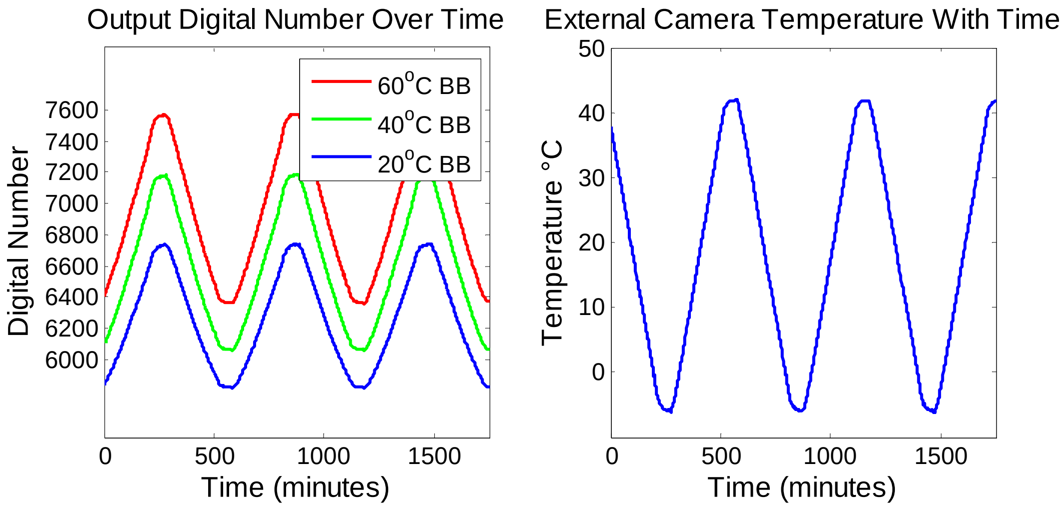

Figure 3-7. The variation in digital number (left) from the infrared camera viewing three blackbody sources at 60 °C, 40 °C, and 20 °C with variation in camera body temperature (right).

The right-hand figure shows the average temperature of the camera body, driven by the air temperature inside the chamber as it was cycled sinusoidally, and the left-hand figure shows the corresponding camera output for the average across each of the three blackbody targets in the camera image. Table 3-1 summarizes the changes in output digital number experienced during this experiment.

Table 3-1: Digital Number for a Constant Source and Variable Camera Temperature

Blackbody Temperature	Mean Digital Number	RMS Deviation
60 °C	6945	407.3
40 °C	6593	378.6
20 °C	6151	311.1

To ensure that the observed drift was caused by changes in the camera temperature, and to determine how stable the camera could be at a constant temperature, the following experiment was conducted. The chamber was set to a constant temperature of 20 °C. The camera and two blackbodies were placed inside the chamber. Both blackbodies were set to a temperature of 20 °C. The FPA temperature of the camera and the digital output were monitored. As seen in the Figure 3-8 for a constant temperature, the digital output of the camera remained steady. Table 3-2 provides a summary of the data from this experiment.

When the camera FPA temperature was kept stable, the output digital number for a constant source also remained stable. This suggests that the primary source of the drift observed in the previous experiment was related to changes to the camera FPA temperature. This also suggests that if the camera were kept at a constant temperature, the calibration should remain stable.

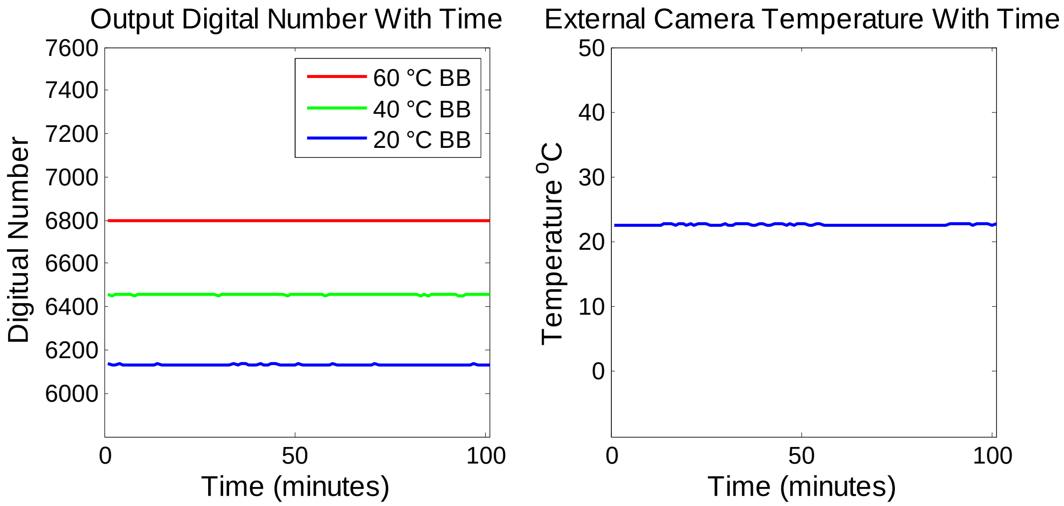

Figure 3-8. The output data from the infrared camera while viewing two constant-brightness blackbody sources in a constant-temperature chamber.

Table 3-2: Digital Number for a Constant Source and Constant Camera Temperature

Blackbody Temperature	Mean Digital Number	RMS Deviation
60 °C	6797	0.825
40 °C	6455	1.144
20 °C	6132	1.020

Initial Corrections of the FPA Temperature-Dependent Drift

Sufficient characterization of the drift in the digital data required accurate and synchronized control of the environment around the camera. The chamber used in the previous experiments was not available at the time, and it did not have the desired level of external control. However, the Space Science and Engineering Laboratory (SSEL) at MSU had a chamber which could be controlled by the same computer that controlled the camera and blackbodies. This allowed for accurate control of the chamber and allowed for coordination of blackbody temperature changes with the changes in chamber temperature. Also, the chamber had an output port through which the camera could view the blackbody, which allowed the blackbody to be placed in an environment that remained at a nearly constant temperature while allowing the camera's ambient temperature, thus camera FPA temperature, to be varied. During these experiments the FPA temperature of the camera was measured using a computer to read the output of a temperature sensor placed near the FPA inside the camera. This sensor provided digital readings of the FPA temperature to within 0.1 °C. Initially it was assumed that this reading accurately represented the temperature of the focal plane array and any separation between the array and the sensor was insignificant. This assumption proved to be false, but the FPA temperature readings still provided adequate information to produce a correction to the digital data.

The results of this experiment were consistent with those of the previous experiment, as seen in Figure 3-7, except that only a single blackbody was used. The digital data were found to drift with the camera FPA temperature. As the camera FPA temperature increased, the digital output recorded with the camera viewing a constant-temperature blackbody source decreased. Thus, the data displayed an inverse relationship, where a decrease in camera FPA-temperature caused an increase in the digital number. Figure 3-9 shows a set of data from this experiment. Unlike the previous experiment, this experiment only used a single blackbody operated at 20 °C. The other black bodies, which were part of another system that was now being operated elsewhere, were no longer available. The use of one blackbody source meant that testing at multiple blackbody temperatures required subsequent runs, but had no other affect on the accuracy of the experiment.

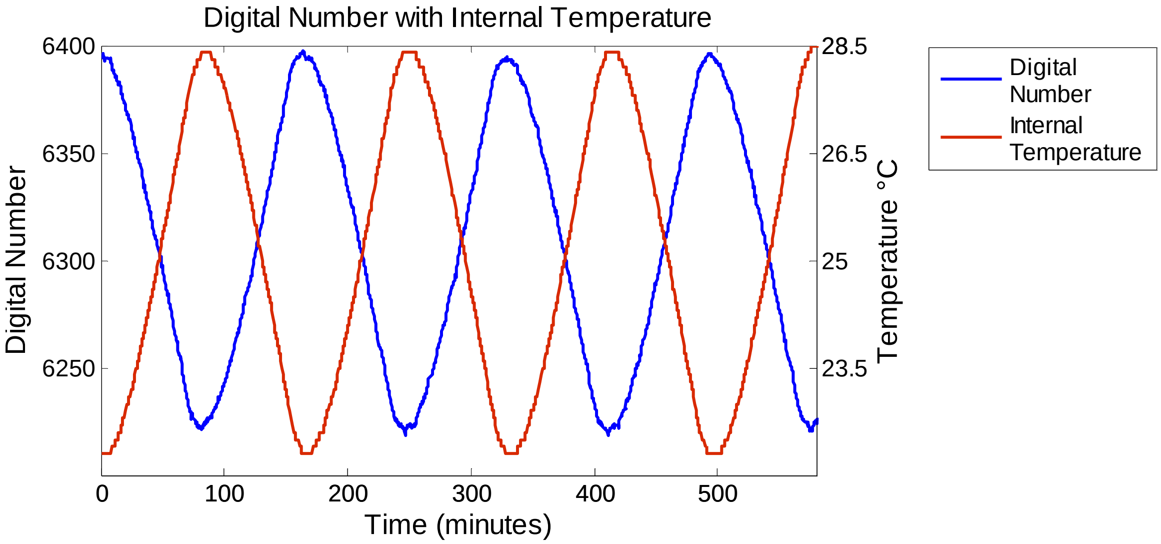

Figure 3-9. The change in camera output digital number (blue line) with change in camera FPA temperature (red line) while viewing a constant blackbody source at 20 °C

When these data are viewed as a plot of output digital number versus camera FPA temperature, the resulting graph appears relatively linear, falling along a negatively sloped line, as seen in Figure 3-10. This was observed while viewing a constant blackbody source.

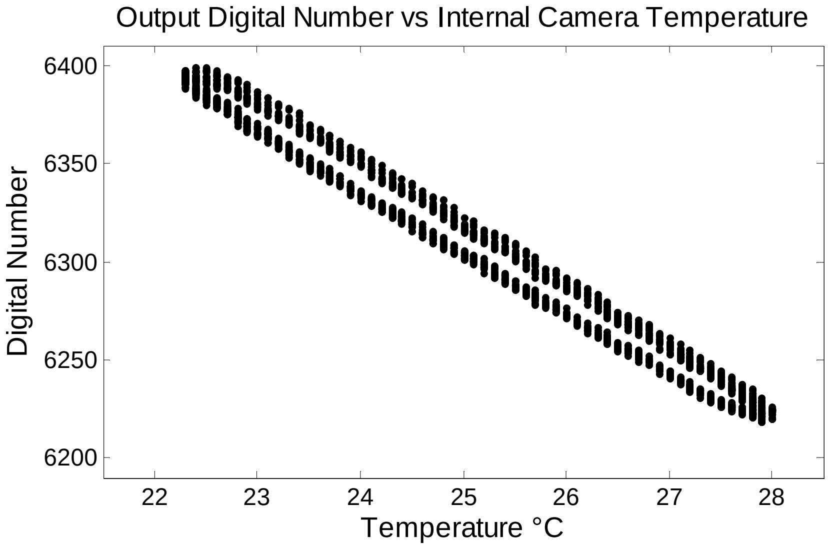

Figure 3-10. The change in the digital data versus reported FPA temperature.

These data fall along one path for increasing camera FPA temperature and along a different path for decreasing FPA temperature. This characteristic of the data can be explained as a time delay between the change in the output data and the reported FPA temperature of the camera. In Figure 3-11 the change in camera temperature and change in the data have been normalized and plotted on the same scale; the change in the data has also been inverted to remove the inverse relationship so that the timing difference can be seen more easily.

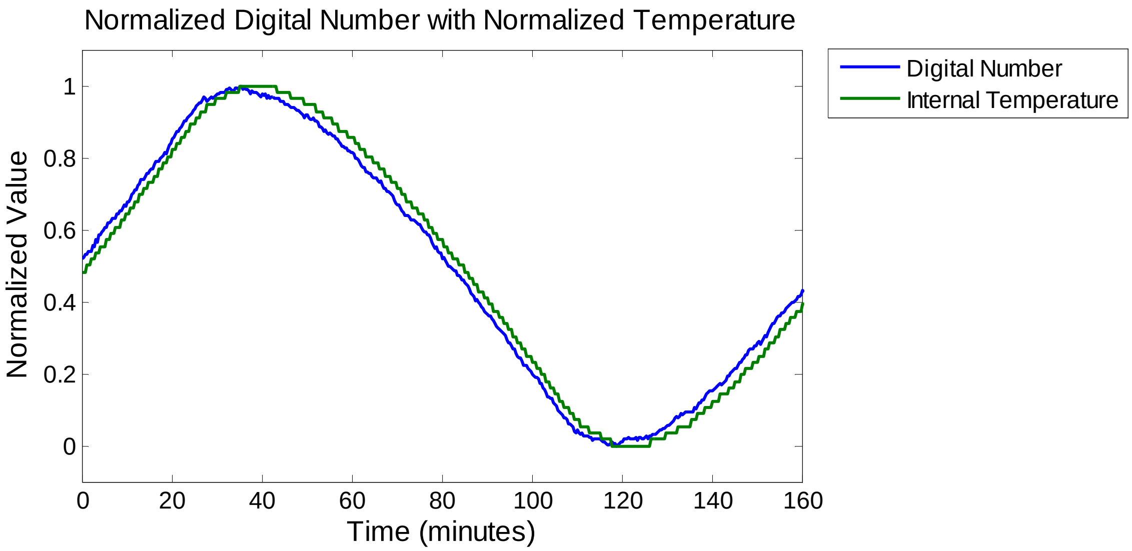

Figure 3-11. The normalized change in digital number plotted with normalized change in internal camera temperature. The digital data have been inverted to remove the inverse relationship so that the timing difference can be more easily observed. The time delay between the two signals is 160 seconds.

The delay in FPA temperature readings can be accounted for by adjusting the timing between the response in the digital number and the FPA temperature reading during post processing. The temperature readout was found to lag the internal-temperature-dependent changes in the digital output by 160 seconds. This corresponded to a shift of 8 data points for the current data set. Once this shift was applied, the linear fit of signal change with FPA temperature was greatly improved. Figures 3-12 and 3-13 show the same data as Figures 3-10 and 3-11, but with a shift of 8 data points on the FPA temperature data. This delay is likely due to the spatial separation between the temperature sensor and the microbolometers of the FPA.

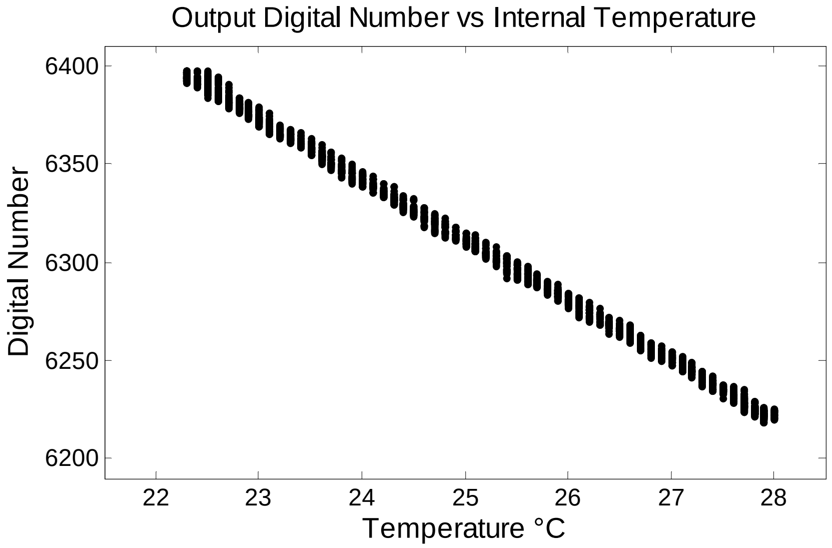

Figure 3-12. The same data as represented in Figure 3-4, but with a 160-second delay on the digital number data.

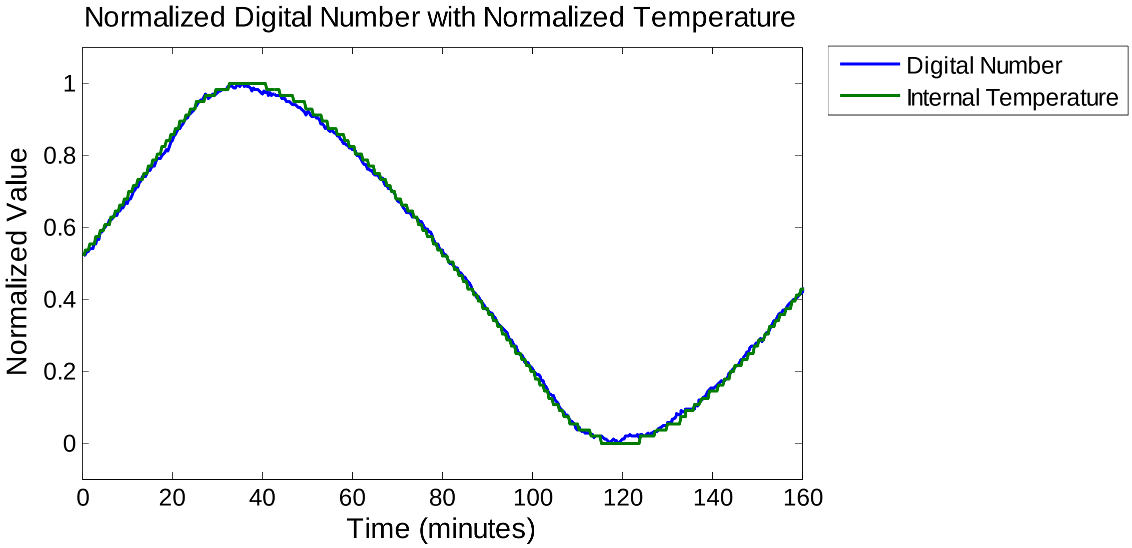

Figure 3-13. The data from figure 3-5 with a 160-second delay on the digital number data.

With the 160-second lag in the FPA temperature readings removed, the relationship between FPA temperature and change in the digital data is improved. The data no longer appeared to follow different paths while heating and cooling. Rather, the relationship appeared to be nearly linear. This relationship can be characterized by a linear equation that expresses the change in digital number for a change in temperature. This linear equation is of the form shown in Equation 3.4

$$\Delta D\# = m\Delta T + b \tag{3.4}$$

In this equation $\Delta D\#$ is the change in digital number, ΔT is the change in temperature, m is the slope of the correction, and b is the offset of the correction. Both $\Delta D\#$ and ΔT were referenced to a given time or point in a data set. The digital data can be corrected by removing $\Delta D\#$ through a linear correction as in Equation 3.5.

$$D\#_{COR} = D\# - m\Delta T - b \tag{3.5}$$

In this equation $D\#$ is the output digital number, $D\#_{COR}$ is the corrected digital number, and ΔT is the change in FPA temperature since the last calibration. This equation can be applied to the data used in Figure 3-9 using the initial FPA temperature as the value from which ΔT is referenced. Figure 3-14 shows the original digital number data and the digital number after this type of correction has been applied. For the correction in Figure 3-8, $m = -30.7039\ D\#/°C$ and $b = -1.1962\ D\#$, with an r^2 value of 0.998.

Applying this correction to the digital output data from the camera stabilized the output camera's response. The digital data were kept close to the value of the data point at which the temperature reference was taken. This could allow the camera to operate in a calibrated mode where the temperature reference was taken at the point of calibration and thus the digital values could be kept stable. Table 3-3 summarizes these results of this experiment before and after the correction was applied.

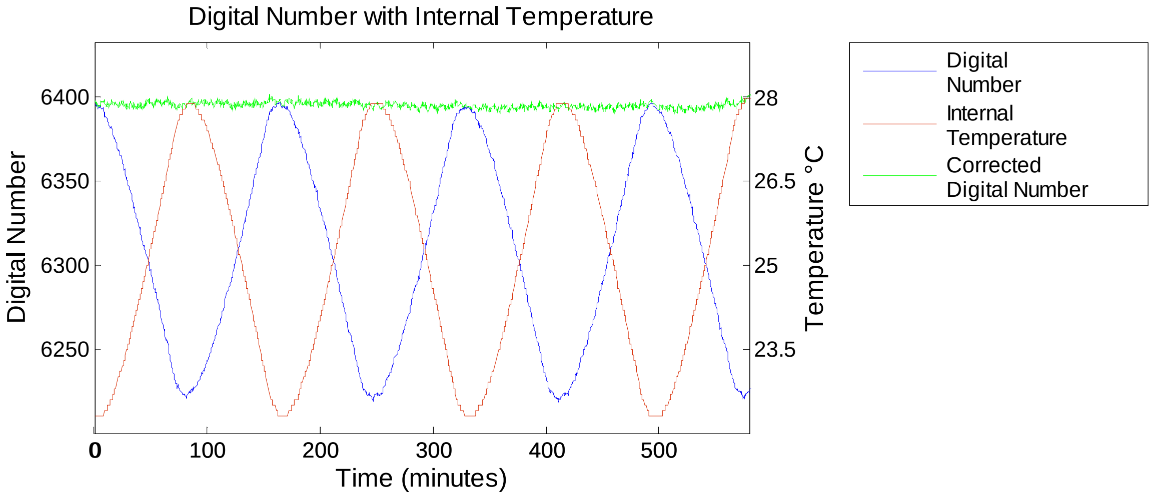

Figure 3-14. The corrected camera output (green line) and raw camera output (blue line) with change in internal camera temperature (red line) for a constant blackbody source at 20 °C.

Table 3-3: Variation in Digital Number Before and After Correction

	Max-Min Digital #	RMS Change
Before Correction	180.7	59.2
After Correction	14.6	2.4

Extending the Correction to Multiple Scene Temperatures

Correcting these data in this manner initially looked promising; however, the drift in these data was found to not remain constant if the temperature of the scene changed. The thermal chamber was used to cycle the camera’s ambient temperature from 15 °C to 30 °C while viewing a blackbody source with its temperature increasing from 10 °C to 50 °C in 5 °C increments. For each blackbody temperature, a correction similar to Equation 3.5 could be applied, but the *m* and *b* coefficients differed for each blackbody scene temperature. This could correspond to both offset and gain of the camera having a dependence on the camera's FPA temperature. Figure 3-15 shows the relationship between output digital number and internal camera temperature for three different blackbody scene temperatures of 10 °C, 30 °C, and 50 °C.

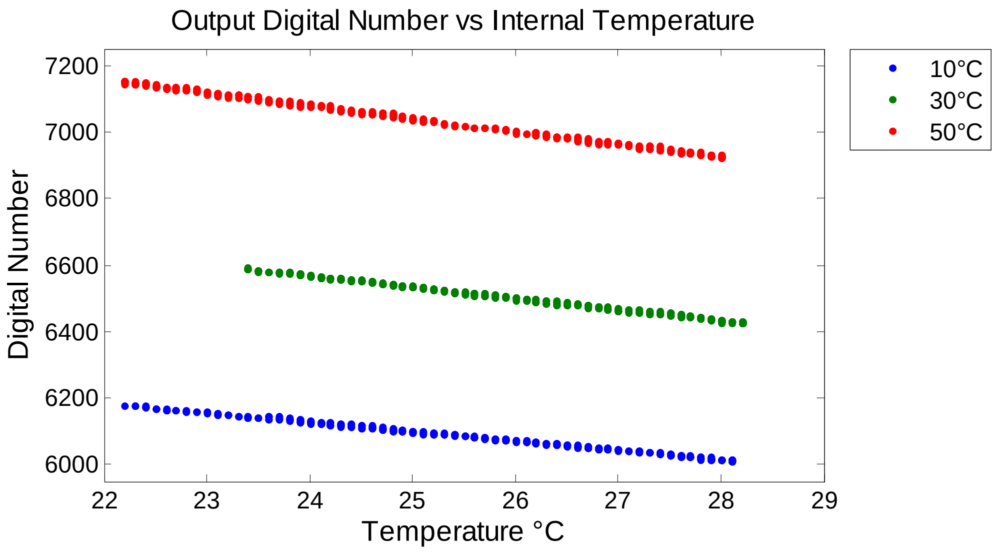

Figure 3-15. The change in the digital data versus reported internal camera temperature for blackbody sources at 10 °C, 30 °C, and 50 °C.

The data in Figure 3-15 have different slopes for each blackbody scene temperature, but this is difficult to distinguish by eye. Table 3-4 offers a better description of these data, showing the slope of the curves in Figure 3-15 for each blackbody source temperature. These data show that the slopes of the curves of digital number change versus internal camera temperature decrease with scene temperature.

Table 3-4: Slope of the Linear Fit for Different Scene Temperatures

Blackbody (Scene) Temperature	ΔD / ΔT
50 °C	-38.8 D# / °C
30 °C	-33.5 D# / °C
10 °C	-28.1 D# / °C

The correction used before for a single blackbody temperature of 20 °C cannot be applied for a scene temperature other than 20 °C. This correction would under-correct for scene temperature greater than 20 °C and over-correct for lower scene temperature. This is a significant problem when trying to image a scene in which multiple temperatures are present, as with clouds against a clear sky.

At any given camera temperature, the values for a series of blackbody radiances should fall along a straight line. The slope and offset of this line has been observed to change with temperature, but this should not change the fundamental linearity of the camera at any given camera temperature. By determining the way in which this linear response changes with temperature, the temperature-dependent portion of the camera's transfer function can be determined.

The data from the multiple-blackbody scene temperatures were broken up by corresponding blackbody temperature. The data were shifted so that the delay in the FPA temperature readings was corrected. Then mean digital number was calculated for each blackbody scene temperature, using data for which the camera FPA temperature was 25 °C. The change in digital number from this value for all other camera temperatures was calculated. The linear fit for change in digital number from the 25 °C versus the actual digital number reading for each temperature was determined. The slope and offset of each of these lines were then viewed as a function of internal camera temperature and a linear fit calculated for each data set. The following flow diagram, Figure 3-16, provides a visual representation of the process used to build the correction. Figure 3-17 and 3-18 show the slope and offset of the change in digital number with digital number, plotted as a function of scene temperature.

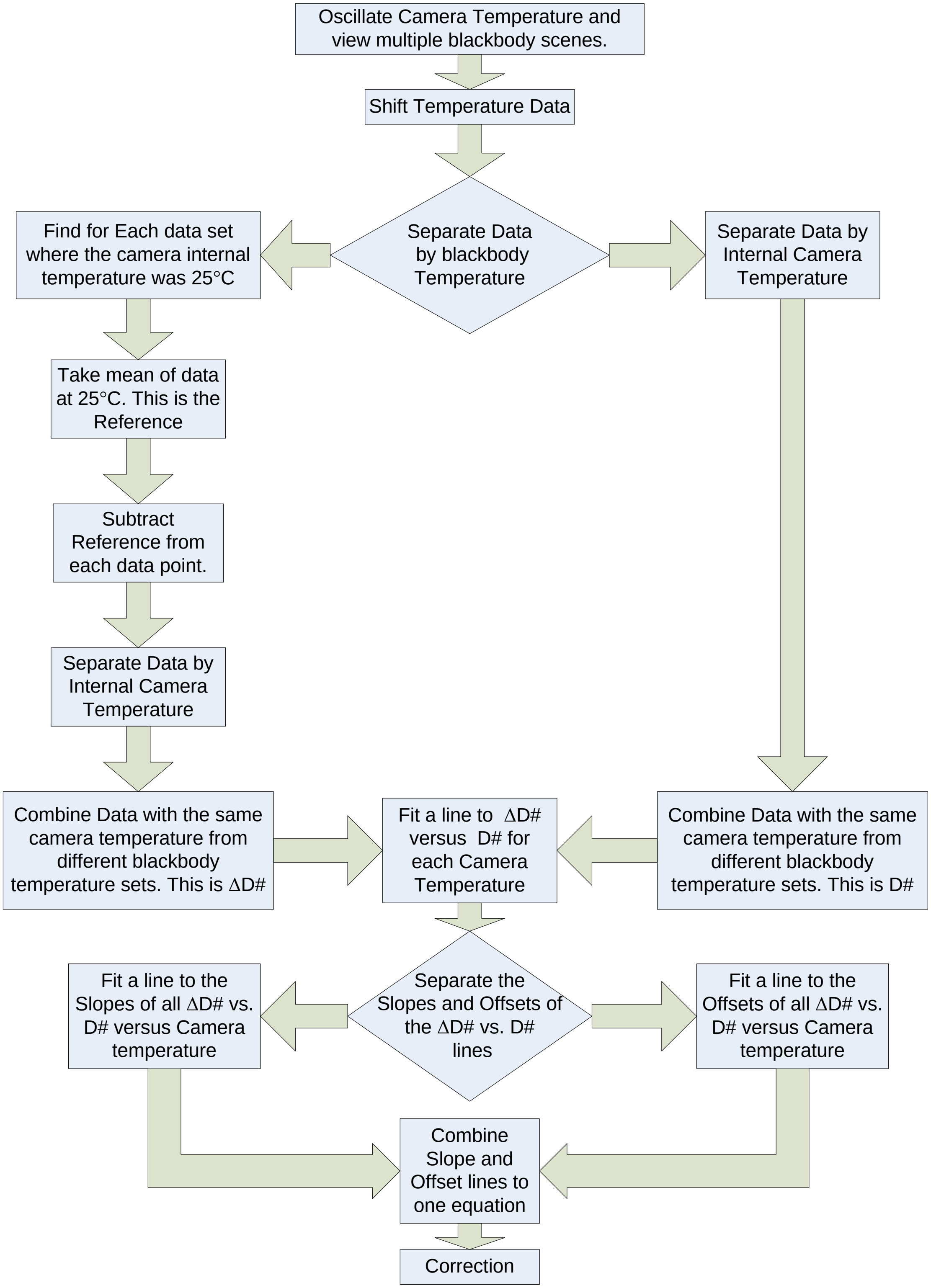

Figure 3-16. The process diagram for the development of the correction capable of accurately calibrating multiple scene temperatures.

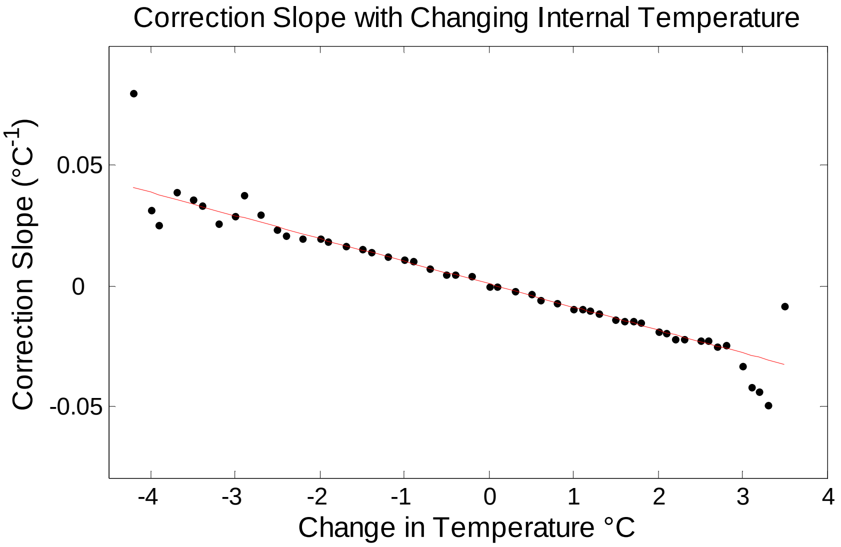

Figure 3-17. The slope of the ΔD# versus D# curves as a function of internal camera temperature

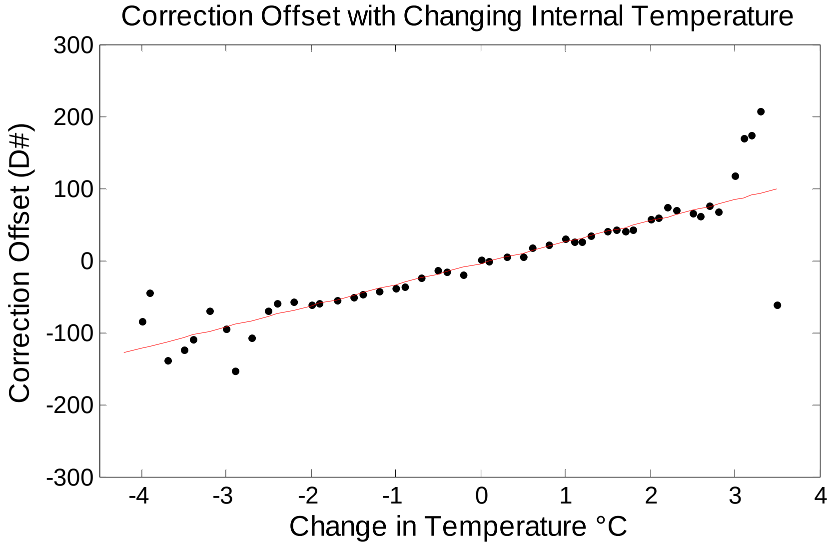

Figure 3-18. The offset of the ΔD# versus D# curves as a function of internal camera temperature.

The two functions plotted in Figs. 3-17 and 3-18 can be used to correct any digital number output, given the internal camera temperature. The correction adjusts the digital number to the value the camera would read for an internal camera temperature of 25 °C. This correction for the camera is an empirical fit to the data change with FPA temperature change and the mean values across the array for this correction are shown in Equation 3.6. In this equation ΔT_{25} is the difference of the current internal camera temperature from 25 °C, not the change since the last calibration as in Equation 3.5.

$$D\#_{Cor} = D\# - (D\#(-0.0118\Delta T_{25} - 0.0018) + (43.506\Delta T_{25} + 11.8871)) \qquad (3.6)$$

This equation contains both temperature-dependent and temperature-independent functions. The intent of developing this correction was to simply remove the FPA temperature dependence of the camera's transfer function. These temperature-independent portions of this function can be dropped, giving Equation 3.7. In this equation the remaining coefficients can be seen as a temperature-dependent change in gain, *ΔGain* the first part of the equation dependent on $D\#$ and ΔT_{25}, and a temperature-dependent change in offset, *ΔOffset,* dependent only on ΔT_{25}.

$$D\#_{Cor} = D\# + 0.0118 D\# \Delta T_{25} - 43.506\Delta T_{25} \qquad (3.7)$$

To determine the correction accuracy, it was applied to the data which had been used to build the correction. Figures 3-19 through 3-22, show the reprocessed data. Before correction the output data varied by ±95 digital numbers, and after correction the data were stabilized to ±9 digital numbers with an rms deviation of 3.7 digital numbers. Table 3-4 summarizes the corrected versus uncorrected data for each source temperature.

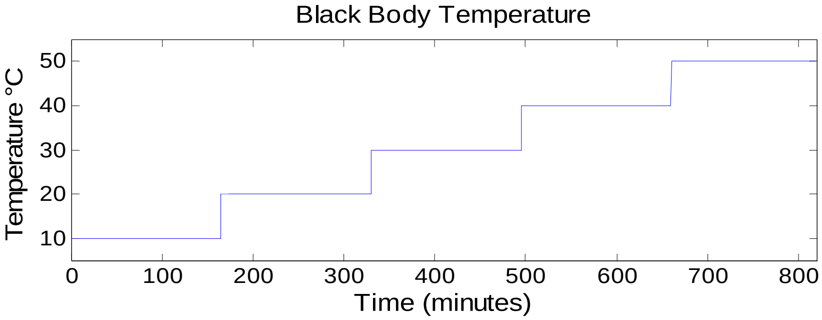

Figure 3-19. Blackbody temperature during the experiment.

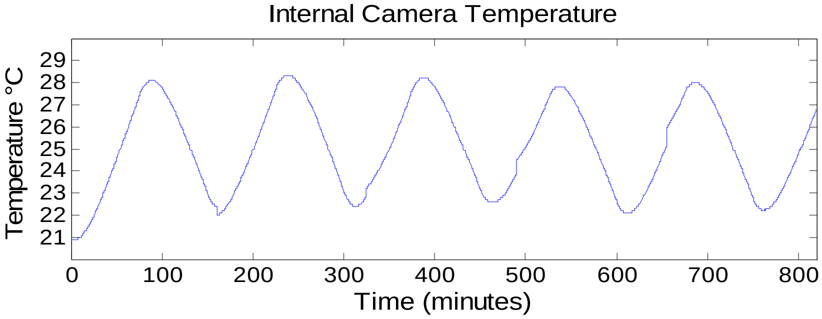

Figure 3-20. Internal camera temperature during the experiment.

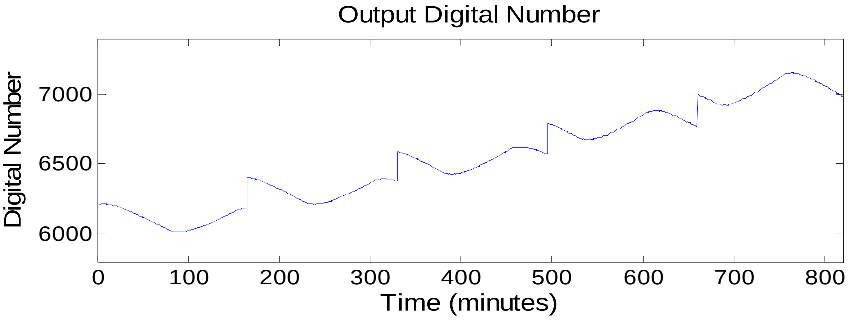

Figure 3-21. Digital number from the camera viewing the blackbody.

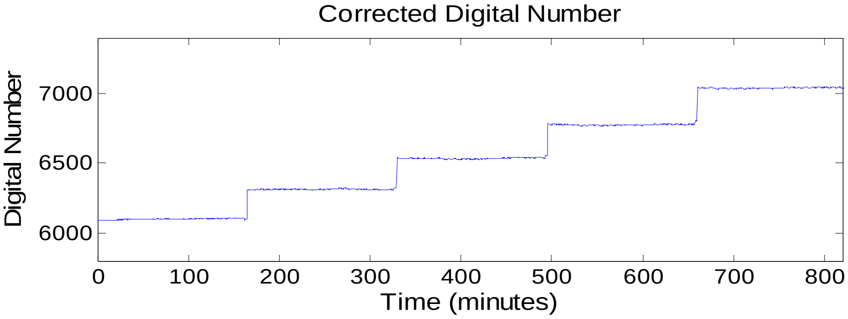

Figure 3-22. Corrected digital number after applying Equation 3.7.

Table 3-4: Variation in Digital Number Before and After Correction

Blackbody Temperature	Max – Min Digital #	RMS Change
Before Correction		
10 °C	205.2	66.2
20 °C	174.3	50.8
30 °C	195.4	57.1
40 °C	214.8	76.4
50 °C	228.5	79.0
Mean	203.7	65.9
After Correction		
10 °C	19.4	4.2
20 °C	16.3	3.3
30 °C	19.5	3.7
40 °C	16.4	3.5
50 °C	17.5	3.9
Mean	17.8	3.7

As evidenced in Table 3-4, the correction works equally well over the various blackbody scene temperatures. The rms deviation is within 3 to 4 digital numbers for a range of scene temperatures between 10 °C and 50 °C. The rms change found when the camera was held at a constant temperature was around 1 digital number. This suggests that the correction does not correct for all the effects of changing ambient temperature on the camera, and that the camera could potentially be even more stable. The camera FPA temperature is only accurate to 0.1 °C and thus adds some of this uncertainty. The uncertainty expected from a temperature accuracy of 0.1 °C is 2.5 digital numbers, accounting for a large portion of the uncertainty in the correction.

Testing the Correction

The reliability of the FPA temperature-correction routine was tested in the thermal chamber using simulated temperature changes for a typical day. Twenty-four hours of data from the MSU weather station were used as the input to the SSEL environmental chamber to simulate a typical summer day and evening for Bozeman MT. The temperature of the blackbody was varied throughout the 24-hour period. Figure 3-23 shows the digital data from the camera before and after the correction routine has been applied.

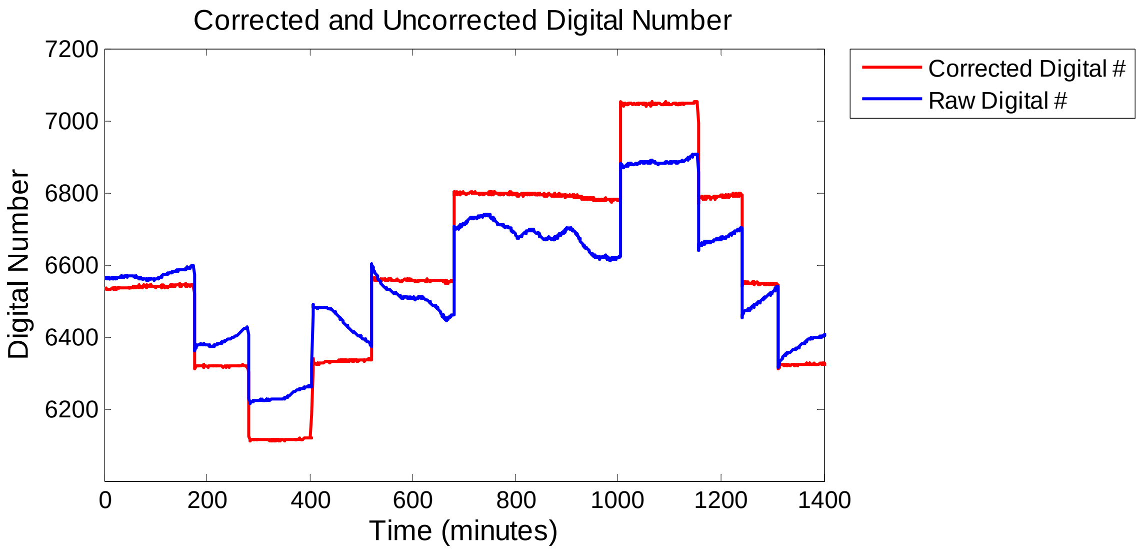

Figure 3-23. The digital number from the camera before and after the correction.

Once the data have been corrected for the FPA temperature-induced variations, the data can be calibrated radiometrically. Using two of the blackbody set points, a calibration of the form shown in Figure 3-4 can be made. These calibrated data compared well with the actual set points of the blackbody, as is shown in Figure 3-24. The difference between the calibrated data and the blackbody set-point temperature, along with the expected error, are shown in Figure 3-25.

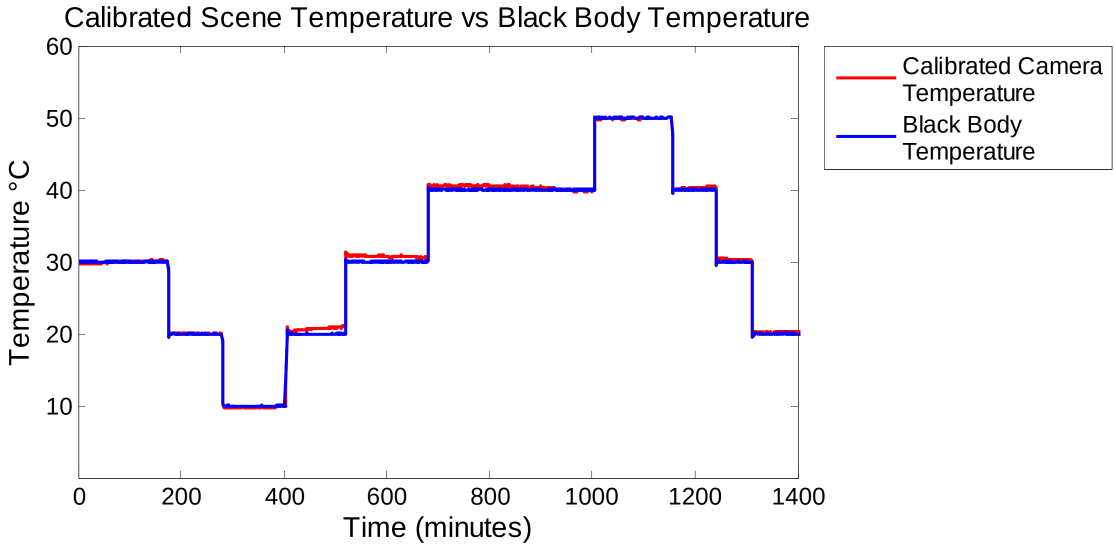

Figure 3-24. The calibrated temperature readings from the camera and the control points for the blackbody emitter during the experiment.

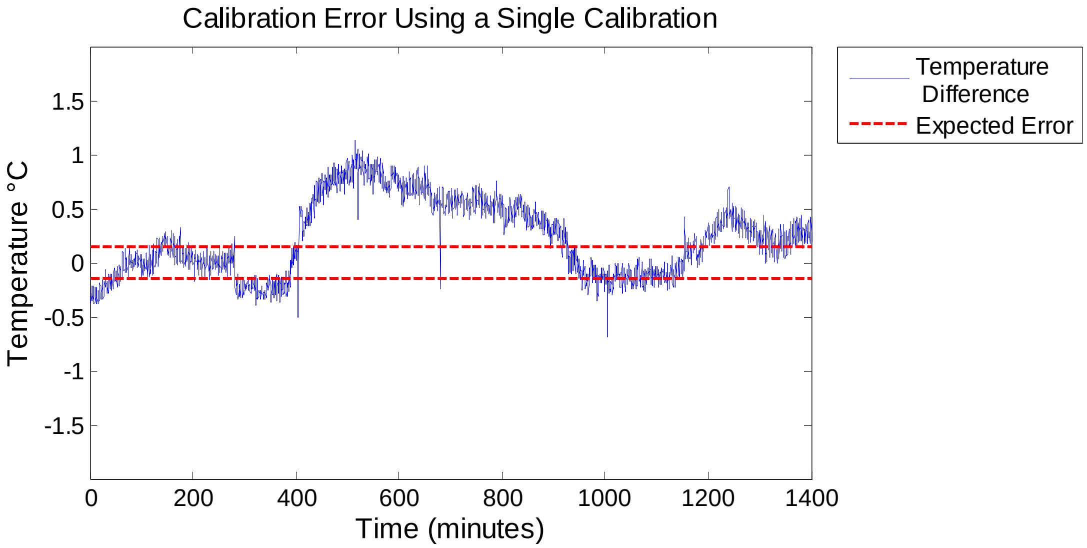

Figure 3-25. The difference between the calibrated camera data and the blackbody control points.

In Figure 3-25 the red lines are the expected error from a ±0.1 °C uncertainty in the camera temperature sensor and a ±0.1 °C uncertainty in the blackbody controller, which are independent errors and can be combined as a sum of squares to give a total expected error of within ±0.14 °C. The calibrated camera data do not fall within these bounds. However, the maximum error is 1 °C, which is larger than desired but is quite good for a single calibration that is applied to all data collected over a 24-hour period.

Thus, there is evidence that the correction of Equation 3.7 reduces FPA temperature-induced error, but is not sufficient to hold the camera in calibration over a full 24-hour period. The increase of the error away from the calibration points, around 200 and 1200 minutes, suggest a slow drift in the camera's transfer function with time. This most likely lies within the temperature-independent portion of the transfer function, S(x). This portion of the transfer function most likely contains time-varying quantities that cannot be directly attributed to the FPA temperature of the camera, and thus are not compensated for by Equation 3.7.

FPA-Temperature Correction for the 100° fov Camera

In May 2007 a second Photon Core camera was sent by JPL to Montana State University for calibration. This camera was different from the original camera in that the 50° fov lens had been replaced with an aftermarket lens that provided the 100° fov with the different lens it was not expected that the camera would have the same performance characteristics as the previous system. However, changing the lens should have no effect on the process used to determine and remove the FPA temperature dependence, even with the increased field of view.

Stability of the 100° fov Camera: Before performing the test to determine FPA temperature dependence, the stability of the camera for a constant FPA temperature was investigated. To accomplish this, the camera was paced inside an environmental chamber which was held at a constant 20 °C. The camera viewed a blackbody source that filled the entire camera fov. This blackbody source was set to a constant temperature of 25 °C. Once the first test was completed, the test was repeated with the blackbody set to a temperature of 40 °C. The results of these tests are shown in Figure 3-26 and Table 3-5.

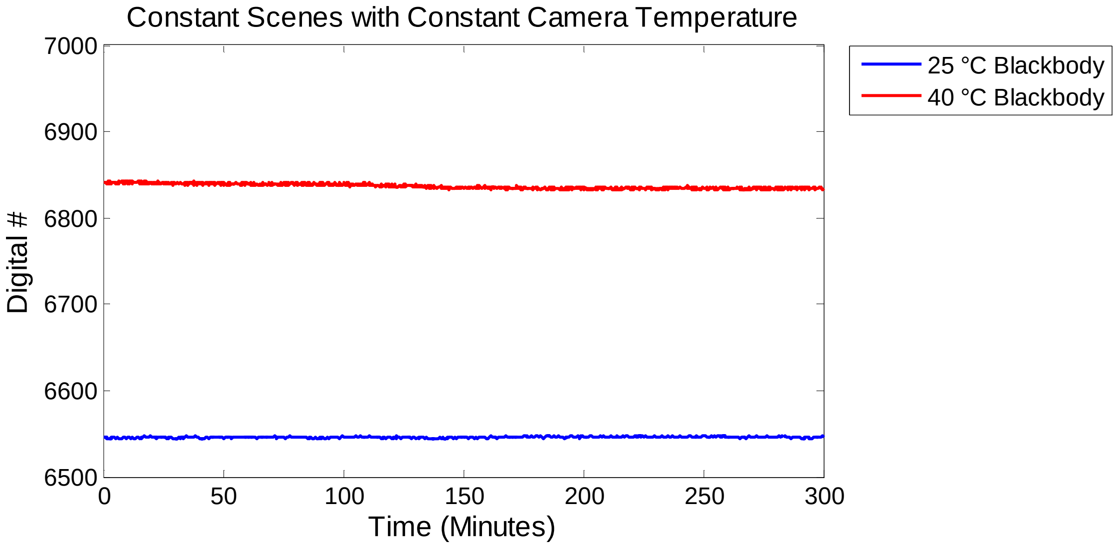

Figure 3-26. Output digital number from the 100° fov camera while viewing two different blackbody sources (25 °C and 40 °C) and a constant ambient temperature of 20 °C.

Table 3-5: Digital Number for a Constant Source and Constant Camera Temperature

Blackbody Temperature	Mean Digital Number	RMS Deviation	FPA ΔT
20 °C	6546	0.823	0.1 °C
40 °C	6837	2.801	0.4 °C

Over each test, the camera's output remained stable. While viewing the 25 °C blackbody the camera exhibited rms variation of 0.82 D#, and while viewing the 40 °C blackbody source it exhibited rms variation of 2.80 D#. During this first test the camera temperature was kept stable to within 0.1 °C, but during the second test the camera temperature increased over the test by 0.4 °C. This temperature increase may be caused by thermal coupling between the warmer 40 °C blackbody and the cooler 25 °C camera. This thermal change didn't take place when the blackbody was set to 25 °C because the temperature of the camera and blackbody were similar. These experiments set a baseline level to which the camera can be expected to be held stable.

<u>FPA-Temperature Correction for the 100° fov Camera:</u> The process used to build the FPA-temperature correction for the 50° fov camera was applied to the 100° fov camera. This camera was placed inside an environmental chamber and viewed a constant-temperature blackbody source while the temperature of the camera's FPA temperature was varied by increasing or decreasing the ambient temperature. As before, this process was repeated for various blackbody scenes ranging in blackbody temperature from 10 °C to 50 °C in steps of 5 °C made every nine hours.

As with the 50° fov camera, it was found that the output for constant scene radiance was found to change as the camera's FPA temperature changed. Also as before, the magnitude of this change was dependent on scene radiance, or blackbody temperature. From these data a correction was built using the process described in Figure 3-27. The temperature-independent portions of this correction were dropped and the resulting FPA temperature correction for the 100° fov camera is shown in Equation 3.8.

$$D\#_{Cor} = D\# + 0.0107 D\# \Delta T - 53.2562 \Delta T \tag{3.8}$$

As done with the 50° fov data, the data used to build the correction were run through equation 3.7 to determine the effectiveness of the correction. The results of this correction are shown in Figure 3-27, and a summary of the corrected and uncorrected data are presented in Table 3-6.

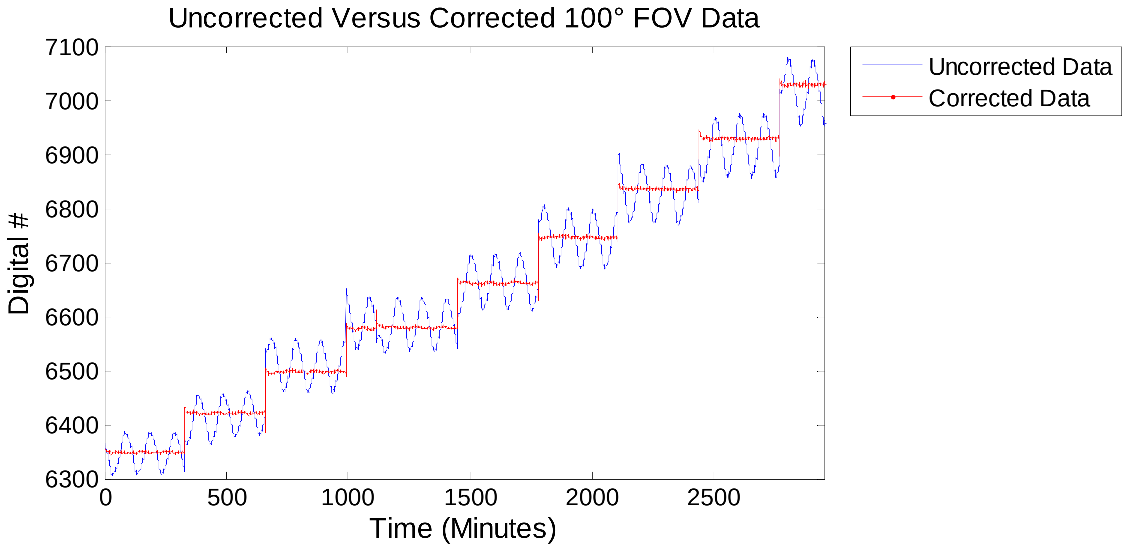

Figure 3-27. Output digital number from the 100° fov camera while viewing a constant blackbody ranging from 10 °C to 50 °C. The temperature around the camera varied from 15 °C to 30 °C causing the output to vary (blue line). After the application of Equation 3.8, the output follows the blackbody (red line).

Table 3-6: 100° fov Variation in Digital Number Before and After Correction

Blackbody Temperature	Max – Min Digital #	RMS Change
Before Correction		
10 °C	81.51	25.54
15 °C	101.06	29.91
20 °C	102.67	32.75
25 °C	105.33	32.78
30 °C	106.67	34.62
35 °C	118.72	36.42
40 °C	113.65	36.47
45 °C	121.60	38.09
50 °C	126.77	40.14
Mean	108.66	34.08
After Correction		
10 °C	9.58	1.6304
15 °C	10.58	1.7107
20 °C	11.07	1.8892
25 °C	10.52	1.8656
30 °C	11.84	2.0498
35 °C	10.31	1.8006
40 °C	10.20	1.6128
45 °C	11.23	1.7987
50 °C	14.60	2.2755
Mean	14.46	1.8481

Testing the 100° fov Camera FPA Temperature Correction: The test using the temperature from the MSU weather station was conducted for the 100° fov camera. This test used the same temperature data and blackbody set points as before to simulate a twenty-four hour summer day and evening for Bozeman MT. After the simulation was complete the digital data were corrected using Equation 3.8. Figure 3-28 shows these data before and after correction. These data were then calibrated radiometrically, using two of the available blackbody set points. These calibrated data compared against the actual set points of the blackbody quite well, and are shown in Figure 3-29. The difference between the calibrated data and the blackbody set temperature along with the expected error are shown in Figure 3-30. This error is a combination due to a ±0.1 °C error in the blackbody temperature and a ±0.1 °C error in the readings of the camera FPA temperature, which when combined as a sum of squares give a total of ±0.14 °C.

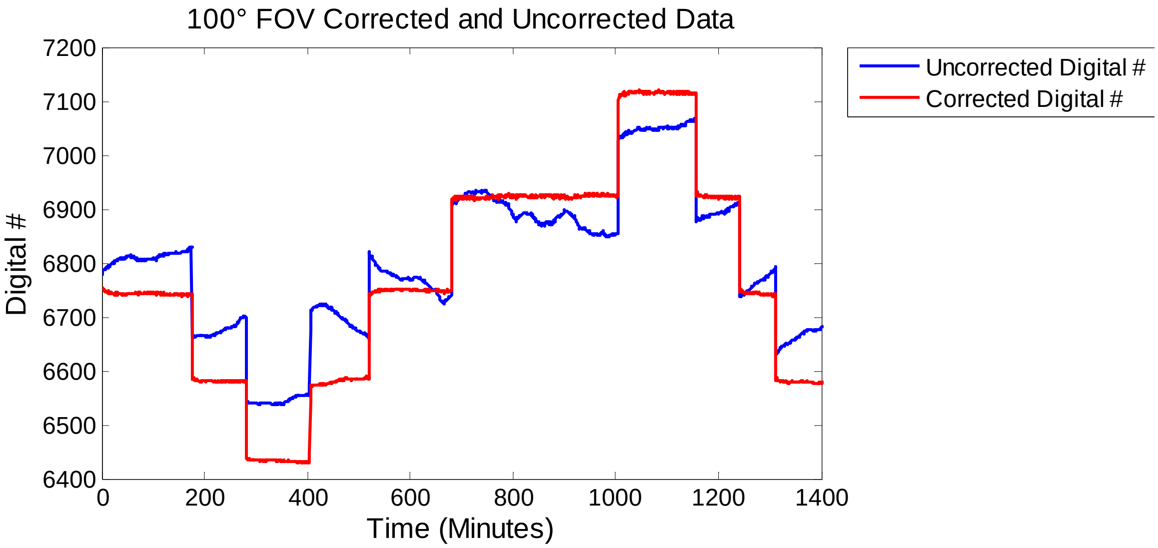

Figure 3-28. Corrected (red) and uncorrected (blue) digital data for a simulated summer day and evening in Bozeman MT.

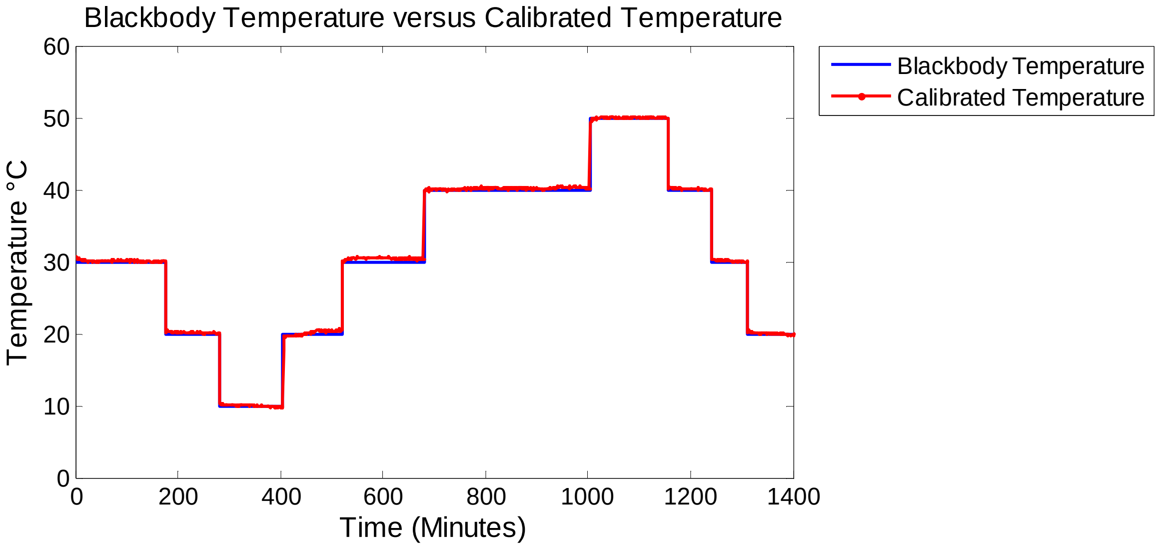

Figure 3-29. The calibrated temperature readings from the 100° fov camera (red) and the control points for the blackbody calibration target (blue) during the experiment.

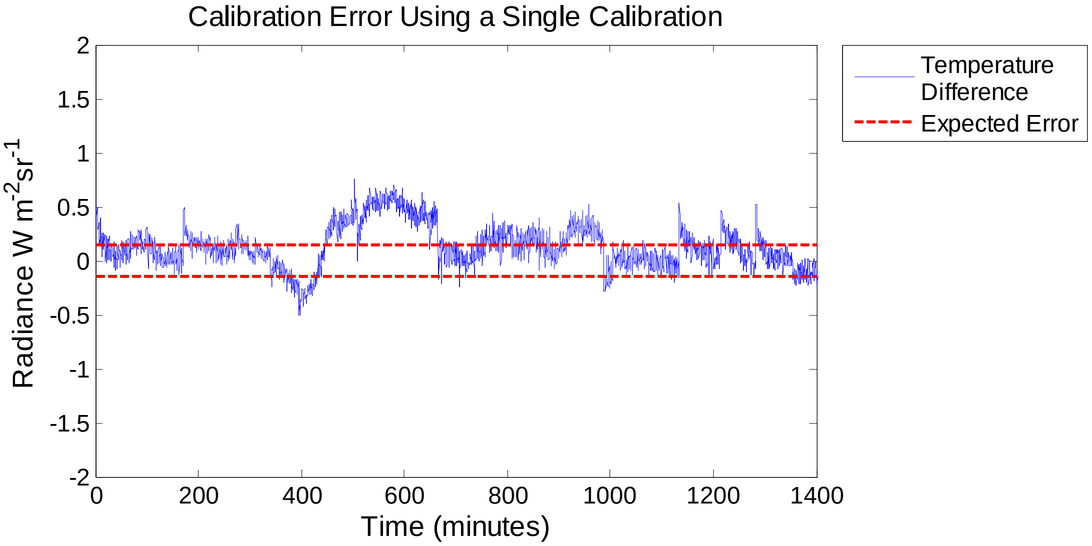

Figure 3-30. The difference between the calibrated camera data and the blackbody control points (blue), along with the expected error due to the uncertainties during the test (red).

The calibrated camera data fall nearly within the expected error bounds. The maximum error is 0.7 °C, less than experienced with the similar test for the 50° fov camera seen in Figure 3-25. This 0.7 °C error is still larger than desired, but again this is quite good for a single calibration for a 24-hour period.

Stability of the FPA Correction over Time

The effectiveness of the FPA correction routines had been shown during the previous experiments; however, the long-term stability of these corrections had not been investigated. An opportunity to do so arose during the summer of 2007 when the 50° fov camera was returned to MSU after a deployment at JPL's TMF. This provided an opportunity to determine if the coefficients of the FPA temperature correction for the 50° fov camera (Equation 3.7) had changed over a one-year period.

One limitation of the accuracy of this assessment was that the camera had been returned to MSU with the focus changed somehow. The camera was originally focused at the hyper-focal distance, for this camera approximately five meters in front of the camera. When the camera arrived at MSU the camera was focused at approximately 0.5 m in front of the camera. Such a change in the focus of the camera was expected to change the calibration of the camera. Therefore, without the focus set back precisely to the position during the original test, it is almost certain that the calibration equations would have changed. The focus was reset as best as possible to the factory settings that had been used to develop the original FPA temperature correction.

With the focus corrected, the tests used to make the original FPA temperature correction were repeated. These tests provided a unique set of data which was reprocessed to determine the coefficients of the FPA temperature correction shown in Equation 3.9. These two correction equations are shown below, with Equation 3.7

repeated for convenience. The coefficients of these equations and the percent difference between the two are shown in Table 3-7.

2006 Correction

$$D\#_{Cor} = D\# + 0.0118 D\# \Delta T_{25} - 43.506 \Delta T_{25} \qquad \text{(From 3.7)}$$

2007 Correction

$$D\#_{Cor} = D\# + 0.0108 D\# \Delta T_{25} - 44.063 \Delta T_{25} \qquad (3.9)$$

Table 3-7: Changes in the 50° fov camera 2006 and 2007 FPA temperature corrections

Coefficient	2006	2007	% Difference
ΔGain	0.0118	0.0108	8.04%
ΔOffset	-43.506	-44.063	1.28%

The change observed in the offset of the camera was most significant for the temperature-dependent gain of the camera, with an 8.04% change. The temperature-dependent change in offset of the camera remained stable within 1.8%, which is within the tolerances of the measurement error for these values. The change in the temperature-dependent change in gain could be due to an actual change in camera characteristics over time or could be due to the focus change. Most likely this change is a combination of both characteristics of the camera changing with time and changes caused by having to reset the focus of the camera.

Laboratory-Based Gain Calibrations

During the 2006 deployment of the ICI system at Bozeman, MT, it was possible to use a blackbody-based calibration for the camera. However, the Optical Communications Group at JPL had determined that the system was to run without blackbody calibration targets during deployment at the TMF. Possible solutions for running without a blackbody were to use an average calibration developed in laboratory setting, or to use the gain from such a laboratory setting and update the offset of this calibration by using the internal shutter as an approximate blackbody reference.

An opportunity to study these two calibration methods arose during summer 2006 when a prototype second-generation ICI was developed using the 50° fov camera. During July and August 2006 this prototype was developed and run at Bozeman, MT. During this deployment this system used a two-point blackbody calibration to calibrate the sky images. The calibrations taken during these experiments allowed for the stability of a direct calibration over time to be observed, and for the ability of using a shutter-based blackbody reference to be observed. Table 3-8 shows the calibration coefficients for each linear calibration developed over the time period of this experiment. The calibration of the camera tended to drift slowly with time, which is a commonly accepted trait of microbolometer based thermal cameras.

Table 3-8: Calibration Coefficients for the summer 2006 experiments

Calibration	Calibration Gain	Calibration Offset
1	0.0338	-161.15
2	0.0342	-163.23
3	0.0341	-162.60
4	0.0342	-163.61
5	0.0353	-168.87
6	0.0344	-163.29
7	0.0356	-170.96
8	0.0366	-177.25
9	0.0350	-167.04
10	0.0370	-179.38
11	0.0364	-175.65
12	0.0369	-178.72
13	0.0356	-170.61
Mean	0.0353	-169.41
RMS Deviation	0.00109	6.325
Percent Deviation	3.07%	3.73%

To investigate the effectiveness of a fully constant calibration and a calibration with only a constant gain, a simulation was developed. The mean of each coefficient of the thirteen linear calibrations was calculated. Each calibration was inverted to give the digital number which would be observed by the camera for a 1 W·m^{-2}·sr^{-1}, 6 W·m^{-2}·sr^{-1}, and a 30 W·m^{-2}·sr^{-1} scene. Two calibrations were used to calibrate each of these simulated scenes, an average gain and offset from the thirteen calibrations for the experiment, and an average gain from these calibrations but with the offset updated using the 30 W·m^{-2}·sr^{-1} scene reference. The results of this simulation showing the results of the two calibration methods for the 1 W·m^{-2}·sr^{-1} and 6 W·m^{-2}·sr^{-1} scenes are shown in Figure 3-31. Table 3-9 shows the tabulated errors experienced with each calibration method during this experiment.

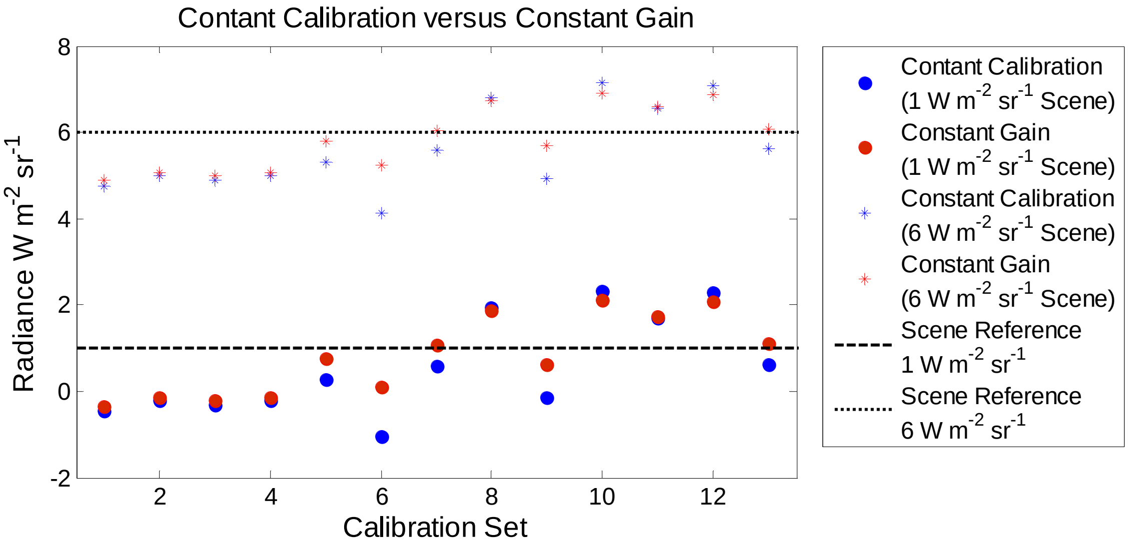

Figure 3-31. Simulation of the errors associated using a constant linear calibration and a linear calibration with a constant gain but an updateable offset.

Table 3-9: Constant Calibration versus Constant Gain: RMS Calibration Errors

Blackbody Scene	Constant Calibration	Constant Gain
1 W·m^{-2}·sr^{-1}	1.17 W·m^{-2}·sr^{-1}	0.90 W·m^{-2}·sr^{-1}
6 W·m^{-2}·sr^{-1}	1.02 W·m^{-2}·sr^{-1}	0.74 W·m^{-2}·sr^{-1}

The updatable calibration has a slightly improved performance than the strictly average calibration. This may seem like a very small improvement; however, it has been shown experimentally that this improvement can be much more than observed in these simulations. After the removal of the 100° fov lens to allow for a bandwidth measurement, the offset of the calibration for this camera greatly changed. Using an average calibration, a clear-sky scene of approximately 5 $W \cdot m^{-2} \cdot sr^{-1}$ appeared to be nearly 25 $W \cdot m^{-2} \cdot sr^{-1}$ when using a strictly average calibration, but was accurate if the internal shutter-based calibration was applied.

The calibration method that was selected to be used during the deployments at JPL's TMF was a laboratory-based gain calibration and updateable offset, adjusted by using the internal shutter of the camera as a blackbody source. This calibration required that the gain of the camera be measured in a very accurate manner. To make these measurements, both cameras were individually placed inside an environmental chamber which was held at a constant temperature of 22 °C. The cameras viewed a blackbody source that was varied from 10 °C to 50 °C every four hours. The radiance of each of these sources was calculated using the known bandwidth of the camera, the temperature set-point of the calibration targets, known temperature of the environmental chamber, and the FPA temperature correction for each camera. The data output by the camera during this test still had a dependence on the camera's FPA temperature, so this temperature was corrected using the FPA temperature correction equation for each camera. From these values, a linear equation was derived relating scene radiance and corrected camera digital number, to represent the response of each pixel of the FPA. The fit calculated for the 100° fov camera, shown in Figure 3-32, relates corrected output digital numbers to calibrated radiance values. The gain or slope of this linear fit was used as the camera gain in the overall calibration of the camera.

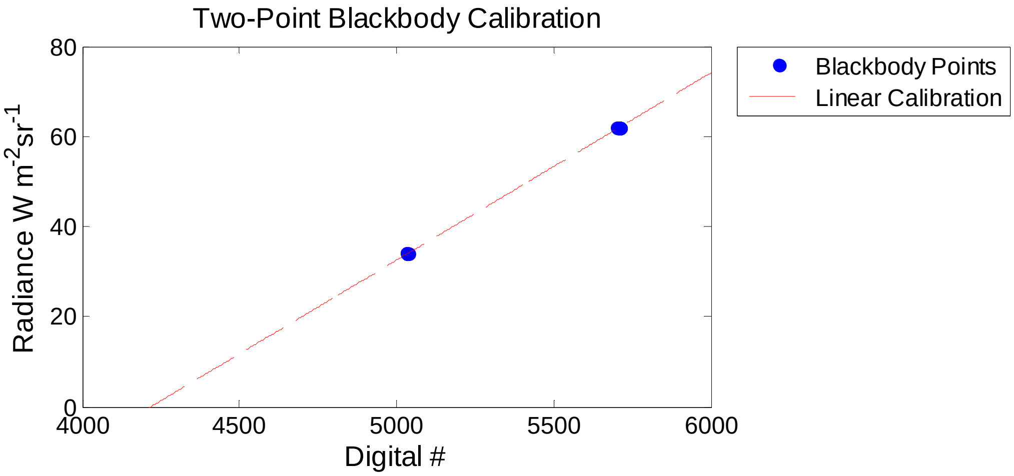

Figure 3-32. Average calibration for the 100 fov camera. The slope of this linear fit is the gain of the camera, which was found to be stable. The offset of this line is the offset for the camera which was found to be variable.

Internal-shutter-based Calibrations

The camera shutter was selected as an alternative blackbody source to track the changes in camera offset during deployment. This shutter is an internal shutter that is used to produce a flat field non-uniformity correction every few minutes during normal operation. It was possible to close this shutter on command and record an unfocused image of the back of the shutter. With proper characterization, this shutter could be used as a blackbody source during a deployment.

The radiometry is quite different between viewing a blackbody source outside the camera and viewing the shutter as an internal blackbody source.. Figure 3-33 shows a geometric optical diagram of a single pixel on the detector viewing an external blackbody source. In the diagram Ω_L is the solid angle over which the pixel views the blackbody scene, filling the pixel's field of view. The radiometric equation representing the camera in this case is shown in Equation 3.10.

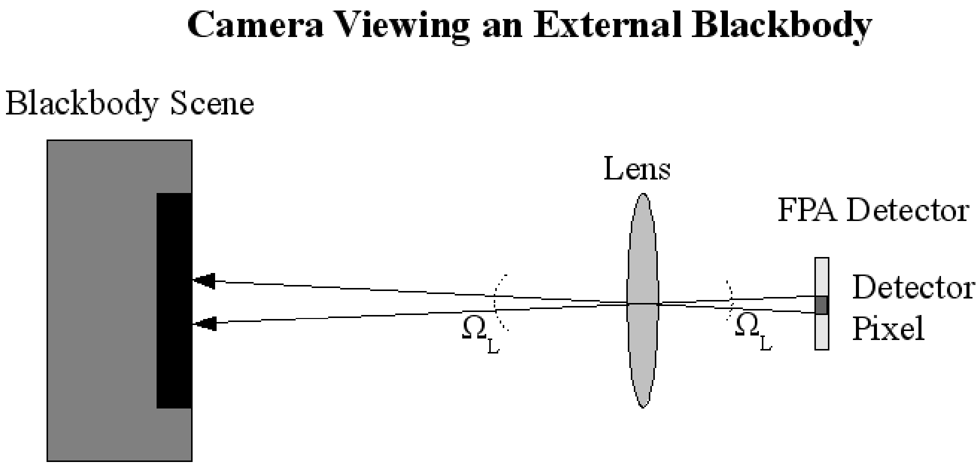

Figure 3-33. Geometric optical layout of the camera viewing an external blackbody.

$$P_{DL} = L_{BB} A_L \Omega_L T_L T_F \text{ [Watts]} \qquad (3.10)$$

In this equation the power on the detector is given as P_{DL}, the power collected on the detector through the lens. This value is a function of the following: the radiance emitted from the blackbody, L_{BB}, the area of the lens, A_L, the projected solid angle defining the field of view for the lens detector-pixel system, Ω_L, transmission of the lens, T_L, and the transmission of the filter attached to the focal plane array, T_F.

The radiometry changes with the shutter closed. This is mostly because the detector no longer views the scene through the lens, but rather it views the shutter directly. Figure 3-34 shows a geometric optics diagram of this case. In this diagram Ω_L

has been replaced by *Ω*Ω_S, the solid angle over which the detector views the shutter. The radiometric equation for this case is shown in Equation 3.11.

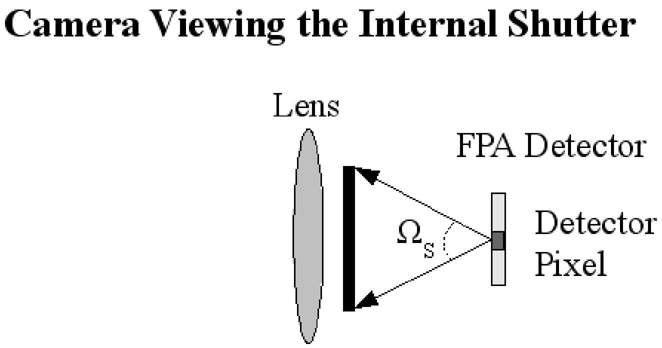

Figure 3-34. Geometric optics layout of a detector pixel viewing radiance from the shutter without passing through the lens.

$$P_{DS} = L_S A_P \Omega_S T_F \text{ [Watts]} \qquad (3.11)$$

In this equation the power on the detector is given as P_{DS}, the power on the detector while directly viewing the shutter. This value is a function of the following: the radiance emitted from the shutter, L_S, the area of a single detector pixel, A_P, projected solid angle field of view for the detector and shutter system, Ω_S, and the transmission of the filter attached to the focal plane array, T_F.

If the external blackbody was set to be the same temperature of the camera, then the radiance from the shutter and the radiance from the external blackbody would be the same. Solving for the radiance values in Equations 3.10 and 3.11 gives the following:

External Blackbody:

$$L_{BB} = \frac{P_{DL}}{A_L \Omega_L T_L T_F} \text{ [W·m}^{-2}\text{·sr}^{-1}\text{]} \qquad (3.12)$$

Internal Shutter:

$$L_{BB} = \frac{P_{DS}}{A_P \Omega_S T_F} \quad [\mathrm{W \cdot m^{-2} \cdot sr^{-1}}] \tag{3.13}$$

With equal blackbody and shutter radiance achieved by controlling the blackbody temperature, equations 3.12 and 3.13 are equal and can be rewritten to give the following:

$$\frac{P_{DL}}{A_L \Omega_L T_L T_F} = \frac{P_{DS}}{A_P \Omega_S T_F}. \tag{3.14}$$

This function in Equation 3.14 can be rearranged to give P_{DL}, the power measured by the detector when viewing an external blackbody. T_{F}, the transmission of the FPA filter, appears on both sides of Equation 3.14. Therefore, this value cancels out, leaving:

$$P_{DL} = P_{DS} \frac{A_L \Omega_L T_L}{A_P \Omega_S} \quad [\mathrm{W}]. \tag{3.15}$$

In this equation the only difference between P_{DL} and P_{DS} is a scaling factor, dependent on properties of the camera. These values should remain constant, but may be dependent on the position in the camera's field of view. Also the transmission of the lens T_L, or other parameters, may cause a slight dependence on the temperature of the camera. These values can be rewritten as Equation 3.16. The combination of these values can be measured as a per-pixel ratio of images with the camera viewing a blackbody and viewing the internal shutter. Once measured, the inverse of this ratio can be applied to the shutter, allowing the shutter to act as an equivalent external blackbody source.

$$\frac{P_{DL}}{P_{DS}} = \frac{A_L \Omega_L T_L}{A_P \Omega_S} \tag{3.16}$$

To make these measurements, the camera was again placed inside an environmental chamber to allow for control of the camera temperature. The environmental chamber was held at a constant temperature, 14 °C to start, and viewed a blackbody which was set to track the FPA temperature of the camera. Once the blackbody and FPA temperature had stabilized to be the same for one hour, a series of images were taken. First a flat field non-uniformity correction was applied to the camera. Then an image of the blackbody was taken. The internal shutter was then closed and an image was taken. This cycle was repeated twelve times. It was found that if these images followed in rapid succession, the movement of the shutter would heat up the camera, and thus the camera and blackbody would no longer be at the same temperature. To avoid this problem, a five-minute delay was placed between each cycle. The chamber temperature was then increased by 2 °C and the measurements were repeated at an increased camera FPA temperature. These tests were conducted until the chamber reached 30 °C. Once this test was completed, the per-pixel P_{DL} / P_{DS} ratio was calculated for each internal-shutter and blackbody pair. This ratio was calculated for each FPA temperature. Then a linear fit was calculated to relate this ratio to FPA temperature, accounting for the temperature dependence of these calculations.

An example of data measured with a shutter-based equivalent blackbody and an actual external blackbody is shown in Figure 3-35. Using the camera's FPA temperature, 27.6 °C for this case, the per-pixel P_{DL} / P_{DS} ratio was calculated, and the shutter was multiplied by the inverse of this ration to make it appear as an external blackbody source. The shutter-based blackbody in this example is higher by 1.4 digital numbers, with a standard deviation of 1.11 digital numbers. This small difference is within the image-to-image noise of the detector.

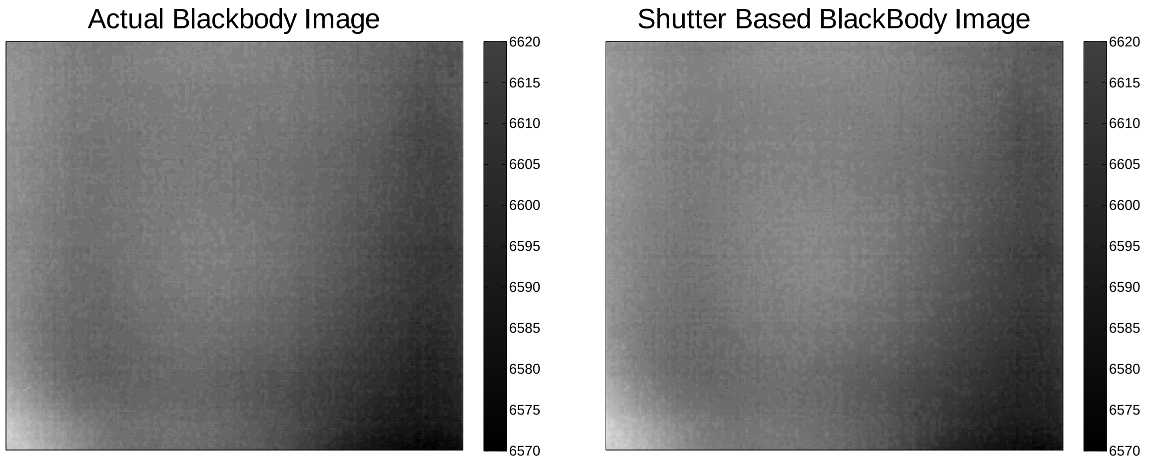

Figure 3-35. An actual image of an external blackbody at 27.6 °C (right) and a simulated external blackbody using an image of the shutter and the P_{DL} / P_{DS} ratio calculated for a 27.6 °C camera.

Each scene is assumed to be a perfect blackbody at the same temperature. Therefore the two scenes can be assumed to be the same values only with one scaled by the effect of the lens. Likewise, the two radiometric equations are equal to each other. The ratio of the two scenes is therefore equal to the effect of the lens. This value can be measured on a pixel-by-pixel basis. Then by applying this effect to each pixel of the shutter image, an image of a blackbody outside of the camera can be approximated.

This calibration is based on three assumptions. First, the camera's gain remains relatively stable with time within a level of uncertainty that can be corrected with a single-point offset correction. Second, the internal shutter is the same temperature as the FPA where the temperature reading is available. This is true only if the camera has a uniform temperature. If there is a temperature gradient across the shutter then it does not act as a blackbody and the calibration will fail. Third, the radiometric differences between viewing the internal shutter and viewing an external blackbody have been characterized and these differences are stable over long periods of time. If any of these three assumptions prove to be false then this calibration will fail. To date, it appears that these assumptions are valid, and this method provides an adequate calibration of the cameras.

Completed Calibration of the Camera

The full calibration of theses cameras consists of three main elements; FPA temperature correction, average gain, and shutter-to-external blackbody conversion. The combination of these three elements allows for a full radiometric calibration to be made of the scene radiance over the camera's bandwidth. The process used to calibrate these cameras is the following: 1) obtain images of the scene and internal shutter, 2) read FPA temperature, 3) convert shutter image to a shutter-based blackbody image, 4) use FPA temperature to correct scene image and shutter-based blackbody image, 5) use laboratory gain and corrected shutter-based blackbody image to calculate the camera offset, 6) use laboratory gain and calculated offset to calibrate the corrected scene image. The flow diagram of this process is presented in Figure 3-36.

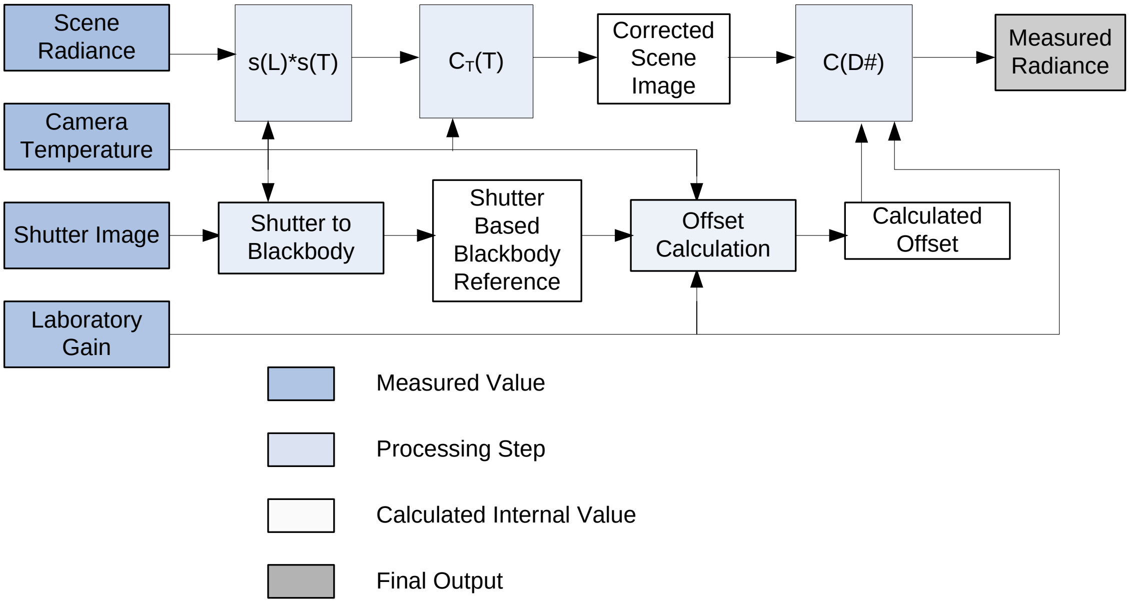

Figure 3-36. A diagram of the processing routine for obtaining calibrated data form the camera.

The internal temperature of the camera shows up as an input in almost every processing step of the calibration process. Thus, the accuracy of this measurement of 0.1 °C is a limiting factor of the accuracy of this calibration. Stabilization that helps avoid rapid temperature changes in the camera may lessen the dependence on the internal-temperature measurement accuracy. Such stabilization has been achieved through the addition of a thin layer of insulation on the outside of the camera. This also helps keep the camera within a temperature range near 15 °C to 30 °C, the range over which the FPA temperature correction routines have been determined.

Radiometric Accuracy of the Calibration

To determine the accuracy of the calibration described in this text an error propagation analysis was conducted. There are two routes from which the system uncertainty can be determined. The first is fundamental limit imposed on the system from noise, typically specified as the noise equivalent temperature difference (NETD). The second is the uncertainty expected in the radiometric calibration of each system.

The NETD for these cameras with the 50° fov lens was specified by the manufacturer to be 65 mK. The NETD for the camera running the after-market 100° fov lens was calculated to be 72 mK. These values were assumed to be specified at room temperature or 300 K. From this information the noise equivalent radiance difference (NERD) can be calculated. Using the assumption of a 300 K base for the NETD, each camera's bandwidth, and the Planck equation, (equation 3.1), the NERD? was calculated for each camera. For the 50° fov system the NERD was 0.0485 $W\cdot m^{-2}\cdot sr^{-1}$, and for the 100° fov system the NERD was 0.0496 $W\cdot m^{-2}\cdot sr^{-1}$. This NERD acts as the limiting factor of the calibration. If all camera properties were to be characterized perfectly, the calibration would be limited by this noise in the system.

The second approach to characterizing the uncertainty of the radiometric calibration is with the general method for the propagation of errors [*Bevington 1969*]. The uncertainties of the system used for this analysis were the following: blackbody uncertainty ±0.05 °C, camera FPA temperature uncertainty ±0.05 °C, and the output digital number stability ±1.5 D# as shown in Tables 3-2 and 3-5. Many of these components enter into the calibration routine at multiple locations; thus, to simplify the error propagation a reduced calibration equation was used. This allowed for the errors due to each value, for example the camera FPA temperature, to be grouped.

This error propagation required the use of actual values for the hot blackbody reference, the cold blackbody reference, internal camera temperature, and digital numbers from the scene. These values were selected to be realistic values for each camera based on known operating conditions and a clear sky. For the 50° fov camera the values were the following: 50 °C blackbody source (7000 D#), 10 °C blackbody source (6300 D#), observed scene (5000 D#), and an internal camera temperature from 15 °C to 35 °C. For these values the calibration uncertainty was calculated to be ±0.36 $W \cdot m^{-2} \cdot sr^{-1}$. For the 50° fov camera different values had to be used: 50 °C blackbody source (5800 D#), 10 °C blackbody source (5000 D#), observed scene (4200 D#), and an FPA temperature from 15 °C to 35 °C. Using these values the calibration uncertainty of the 100° fov system was determined to be ±0.51 $W \cdot m^{-2} \cdot sr^{-1}$. This higher uncertainty for the 100° fov camera is due to the lower transmission of the after-market lens. This causes the same range of scene radiance to fall over a smaller range of digital bins, and thus the same error in digital numbers equates to a higher error in calibrated scene radiance.

In both cameras the calibration uncertainty is nearly an order of magnitude higher than the NERD. This suggests that the calibration of the system could be further improved. Achieving a calibration uncertainty that matched the NERD of the system is most likely not achievable with the current readout resolution of detector array temperature, etc.

In addition to the calibration error, there is additional uncertainty of the atmospheric emission removal algorithms, which produced an accuracy of ±0.25 $W \cdot m^{-2} \cdot sr^{-1}$. This error is independent of the calibration error, and thus the addition of these errors need be done as a sum of squares. This gives a total error expected for the 50° fov system of ±0.44 $W \cdot m^{-2} \cdot sr^{-1}$. For the 100° fov system this error increases to ±0.57 $W \cdot m^{-2} \cdot sr^{-1}$. For accurate detection of a cloud, the threshold above the background needs to be greater than this uncertainty. This is largely due to increased uncertainty due to a nonuniform distribution of water vapor in the atmosphere. If a level near the uncertainty of the systems was selected, it could lead to water vapor variations being detected as clouds. Thus, for these systems, minimum cloud-detection thresholds of 2 $W \cdot m^{-2} \cdot sr^{-1}$ for the 50° fov system and 1.8 $W \cdot m^{-2} \cdot sr^{-1}$ for the 100° fov were selected. These thresholds may leave out the thinnest clouds, but should allow for detection of all other clouds.

For this work errors not attributed to the directly measurable values were not considered, including: error in the camera bandwidth values, error in the temperature correction coefficients, and any error in the internal shutter to external blackbody conversion. To make a full accurate determination of the expected error these components would need to be considered. Also a full analysis would need to include the spatial non-uniformity of the blackbodies along with variation of all other errors across each camera’s full fov.

EXPERIMENTS USING THE PROTOTYPE SYSTEM

With the calibration of the cameras completed, experiments were run at Bozeman, MT during July 2006 and just over one year later during October 2007. A long-term deployment of the 50° fov camera also took place at JPL's Table Mountain Facility (TMF) from December 2006 through April 2007. The 2006 experiment only used the 50° fov camera as it was the only system available at the time. The second experiment, during fall 2007, used both the 50° fov and the 100° fov cameras. The results of these deployments are discussed in this chapter. The goal of these deployments was to demonstrate the capability of the Photon cameras to provide the calibrated data necessary to provide cloud cover statistics. This was proven during the deployment at Bozeman in July, 2006 and the deployment at TMF from December, 2006 through April, 2007. The goals of the second experiment in Bozeman were to demonstrate the capability of the increased 100° fov system to operate successfully and to compare the calibrations and capabilities of these two systems. The following chapter shows the major results from these experiments, demonstrates the capabilities of these systems to operate as cloud detection systems for the development of cloud cover statistics, and demonstrates the capability of these systems to be accurately calibrated.

Summer 2006 Experiments in Bozeman MT

During summer 2006 the initial calibration routines were completed and the components needed to build a prototype second-generation ICI based around the 50° fov FLIR Photon Camera were available. Such a prototype was completed during July 2006, and was operated over a two-week period when weather permitted. Figure 4-1 shows an image of this prototype system.

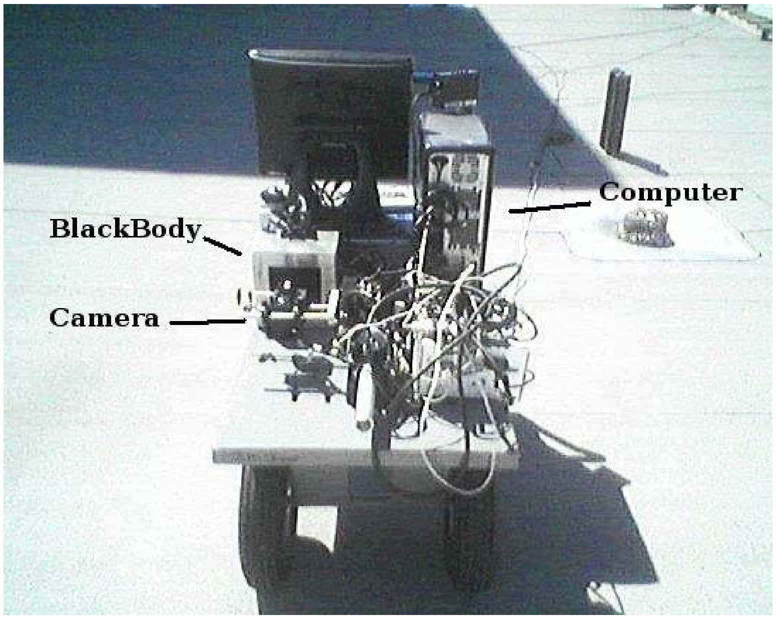

Figure 4-1. The prototype 50° fov ICI system constructed during July 2006. (Photo by P. Nugent)

This prototype was designed to be simpler than the first-generation ICI. During the initial deployments in August 2006 the system used a two-point blackbody based calibration; however, the system also took images of the internal shutter with each sky image. This was done to track the calibration of the system, but later allowed for the investigation of the shutter-based calibration techniques.

Blackbody-Based Calibration

The camera was mounted on a rotation stage so that it could look at both a blackbody source and the sky. The camera would take a blackbody reference image, then look upward, viewing the sky while the blackbody changed its temperature alternating between 50 °C and 20 °C over a four-hour period, and then turn back to the black body and take a reference image. This allowed one blackbody source to provide the two references needed for a two-point calibration. The FPA-temperature correction routine was used to keep the camera's calibration stable during the time periods between blackbody calibration points.

During these operating times radiosondes were used to provide the required measurements of precipitable water vapor, and the MSU ORSL weather station provided near-surface air temperature and dew-point measurements. The precipitable water vapor and surface temperature at the time of the launch were used to update the *a* coefficient in the Reitan equation (Equation 2.6). The *b* coefficient for the Reitan equation had been calculated using Bozeman radiosonde data collected over a two-year time period prior to these measurements. This allowed for changes in precipitable water vapor to be estimated through near-surface dew-point measurements. This increased the accuracy of the atmospheric radiance removal routines before or after each radiosonde.

Once the ICI had measured the downwelling sky radiance, these data were processed with a three-step process as shown in Figure 4-2. The first step is to calibrate each sky image using the FPA-temperature, a 50 °C blackbody reference, a 20 °C blackbody reference, and the camera bandwidth. The second step is to calculate and remove the atmospheric background radiance from the calibrated sky image. The emission from the atmosphere can be calculated using the camera bandwidth, precipitable water vapor, near-surface air temperature, and the camera's field of view. During the August 2006 experiments the bandwidth and field of view for the 50° fov camera were estimated. The bandwidth was estimated to be square from 7.5 μm to 13.5 μm. The field of view was estimated to be 50°x38°, with no distortion and with equal-angle steps for each pixel. With the atmospheric emission removed from the data, only residual-radiance due to cloud emission remains. The final step of the processing is to threshold the residual radiance data. During the August 2006 experiments it was determined that a combination of the residual radiance from a clear sky and the calibration uncertainties of the system led to a minimum detectable cloud radiance level of 2 $W \cdot m^{-2} \cdot sr^{-1}$. This threshold was used for cloud detection during these experiments, and only provided detection of cloud presence but not cloud type.

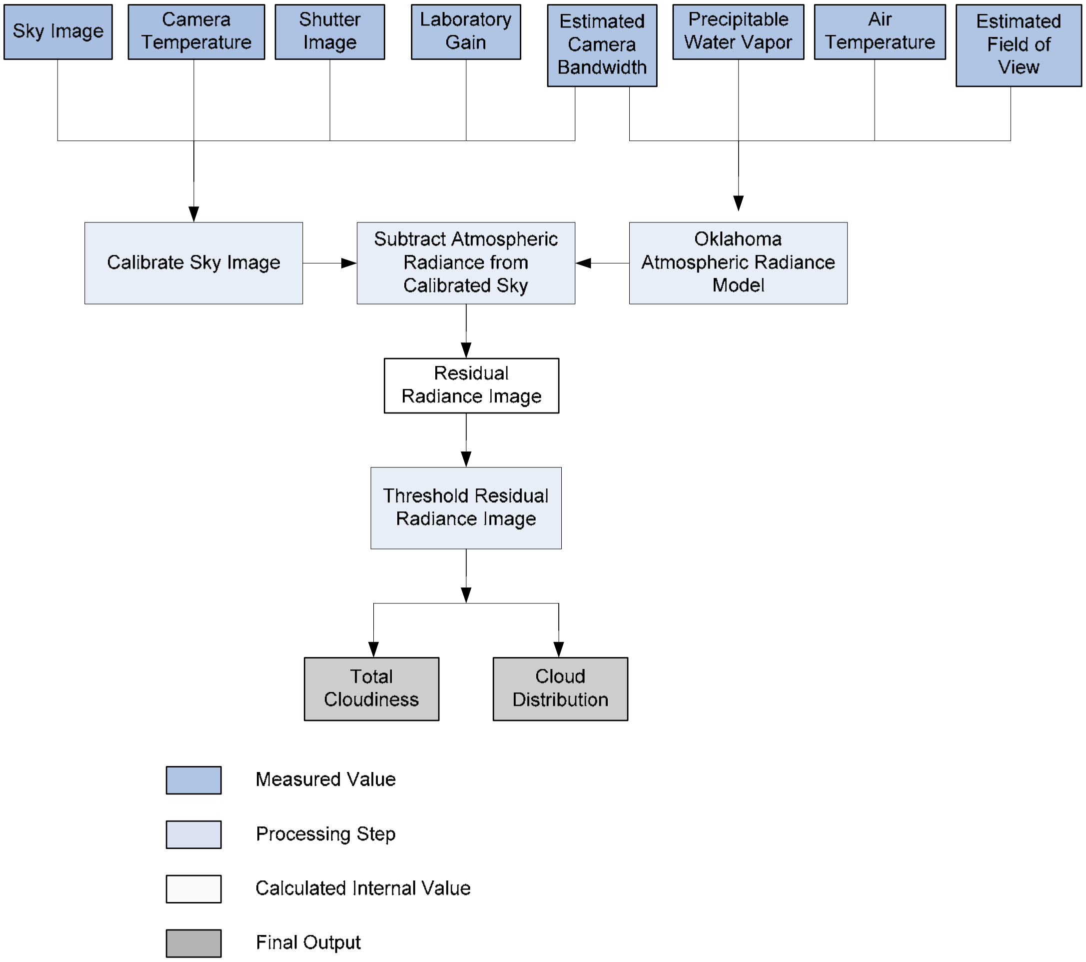

Figure 4-2. The processing routine used to process the August 2006 ICI data.

Two examples of processed data from this deployment are shown in Figures 4-3 and 4-4. In each of these three-panel figures the left panel is the calibrated sky radiance image, the center panel is the residual radiance image after the removal of atmospheric emission, and the right panel is the cloud mask after applying a cloud detection threshold. The cloud mask images have cloudy regions shown as white and clear regions as black.

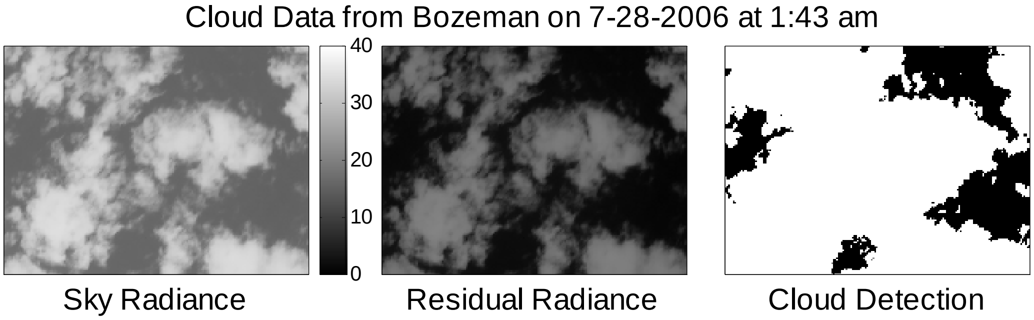

Figure 4-3. Processed data from Bozeman, MT on 28 July, 2006 at 1:43 am Mountain Daylight Time.

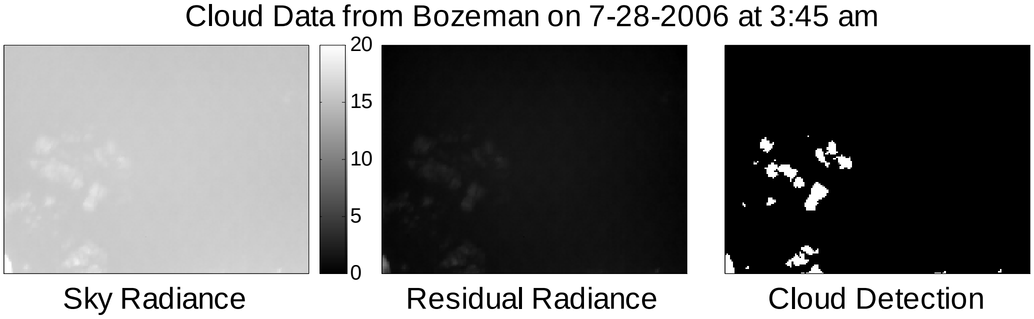

Figure 4-4. Processed data from Bozeman from the same night as Figure 4-3, but at 3:45 am Mountain Daylight Time.

During these experiments the ICI 50° fov camera was able to detect the presence of both thick and thin clouds reliably. The ability to maintain the calibration of the camera in a non-laboratory setting was demonstrated. The use a threshold of 2 $W \cdot m^{-2} \cdot sr^{-1}$ suggests that all but the thinnest cirrus clouds should be detectable with this version of the second-generation ICI.

Internal Shutter-Based Calibration

The JPL Optical Communications Group wished to run the ICI systems at their Table Mountain Facility (TMF). This facility is a remote telescope site located in the mountains of southern California. It had been determined by the group at JPL that the second-generation ICI systems they wished to deploy should run without the aid of an external blackbody calibration target. This posed a problem, since to update the calibration of these systems, at least a single blackbody calibration source was needed. It was determined that the internal shutter of the camera could serve as a blackbody source through the method described in the previous chapter. During the August 2006 deployment at Bozeman the prototype 50° fov system had taken an image of the internal shutter before each sky image. This internal shutter image was then used after the experiment to recalibrate the data and determine how accurately the internal shutter could act as a calibration source.

The shutter-calibrated data were compared with the blackbody-calibrated data, which were used as a reference because of the known accuracy of the blackbody-based calibration. Figure 4-5 shows a comparison of data calibrated using each calibration method and a background clear-sky emission signal calculated using a modified version of the Oklahoma model with precipitable water vapor from a radiosonde and near-surface air temperature as inputs. It was found that these two calibration methods did not agree well during the calibration period, and neither appeared to agree with the calculated atmospheric background signal.

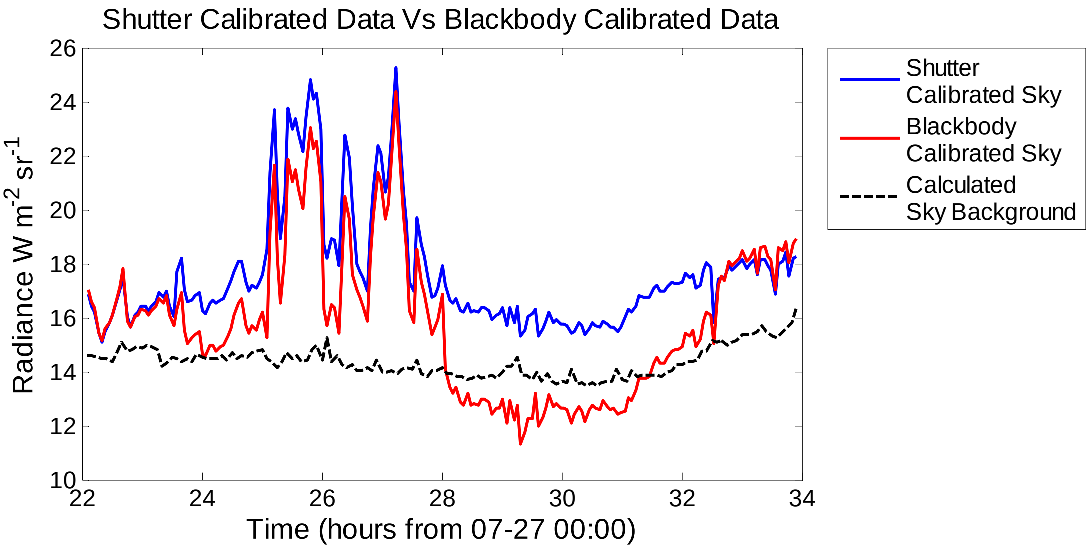

Figure 4-5. Comparison between the blackbody-calibrated data, internal shutter-calibrated data, and a calculated clear-sky background signal.

The cameras measured nearly identical results during the clear-sky periods 22:00 to 24:00 on 07-27-2006 (22 to 24 on the graph) and 8:00 to 10:00 on 07-28-2006 (32 to 34 on the graph) and during a period of clouds from 00:00 to 4:00 on 07-28-2006 (24 to 28). However, from 4:00 to 8:00 on 07-28-2006 (28 to 32) the blackbody calibration measured much lower measured sky radiance. Neither the internal-shutter nor the blackbody-based calibration compare well with the simulated background radiance during any of these time periods.

One possible explanation for the difference between the shutter and blackbody calibration could be instability in the 50 °C blackbody reference due to cool ambient temperatures outdoors and wind blowing across the blackbody face (in this experiment the blackbody operated outdoors, open to the ambient air). Evidence of such an error is found in the timing of the jumps in the blackbody-calibrated data. The blackbody reference is updated every 1.5 hours, at 23.5, 25, 26.5, 28, 29.5, 31, and 32.5. All these blackbody reference changes, except the reference change at 31, are accompanied by an observable jump in the calibrated radiance, sometimes by up to a few W·m^{-2}·sr^{-1}.

Another possible source for this error, or increased error, could be due to the FPA-temperature used at the time, as an early version of this FPA correction was used with these data. Such an error would cause the blackbody calibrated data to follow the internal-temperature of the camera shown in Figure 4-6. There is some evidence that the blackbody-calibrated data may have shown this trend.

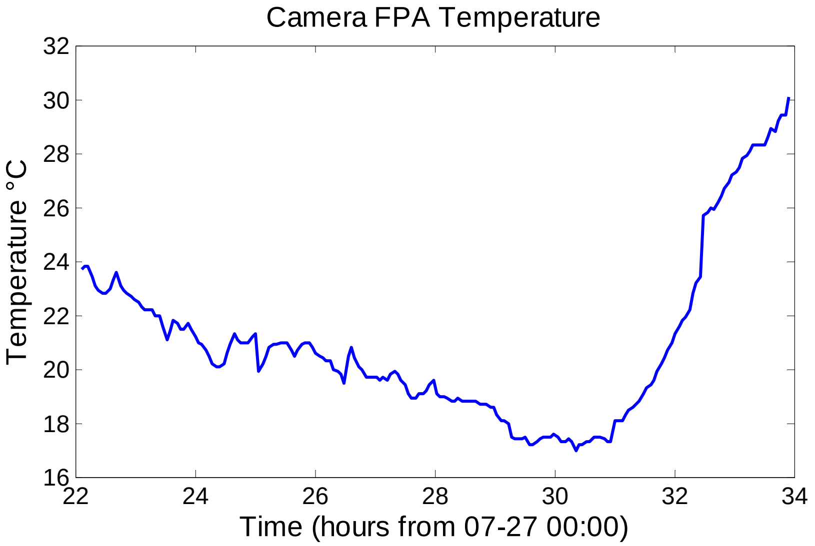

Figure 4-6. Camera FPA temperature during the calibration method experiment.

The internal shutter-based calibration may be less sensitive to this because it measured the offset for each image at the FPA temperature. Thus, the calculated offset is a full measurement of the offset containing both temperature-independent and temperature-dependent components. Therefore, by measuring the shutter and image consecutively the temperature-dependent portion of the offset is compensated for and cancels out of the calibration equation. Therefore when operated in a shutter-based calibration mode only, the FPA-temperature-dependent gain needs to be corrected. The temperature-dependent change in gain is a smaller change than the temperature-dependent change in offset. The two blackbody references are not taken at the same time as the sky image, thus the calibration is fully dependent on the FPA-temperature correction. During this experiment an early version of the FPA-temperature correction was used, but subsequent work has greatly improved this correction.

The possible explanations for the difference between the shutter-based calibration and the blackbody-based calibration do not explain why neither method compares well with the simulated background radiance. The likely explanation for this is found in the radiosonde profile from the night of the experiment. Figure 4-7 shows the first 1 km of a temperature profile from a radiosonde launched on 07-27-2006 at 22:30.

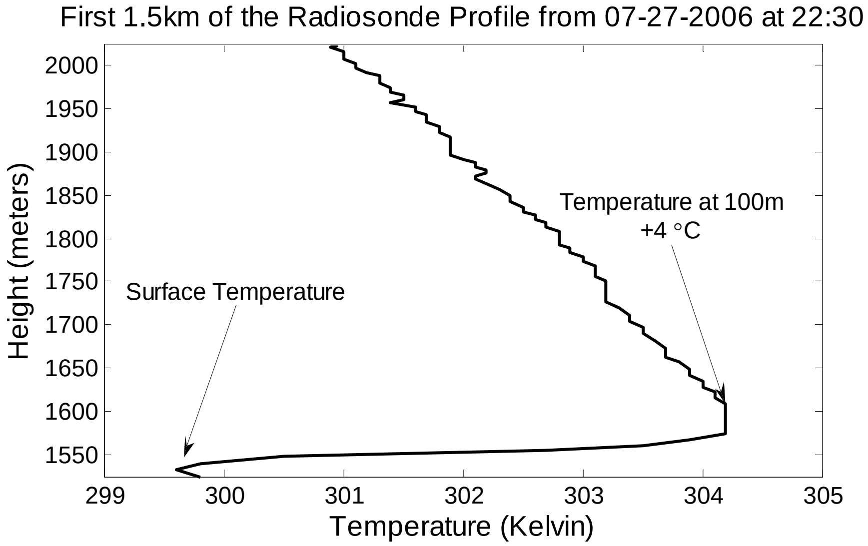

Figure 4-7. The temperature profile in the first 1 km of the atmosphere on 07-27-2007. There exists a strong temperature inversion in the data, with the air 100 m above the surface reading just over 4 °C higher than the near-surface readings.

During this experiment there existed a temperature inversion, as seen by warmer air overlying colder near-surface air. On this night the air 100 m above the surface was just over 4 °C warmer than the near-surface temperature readings. During times of temperature inversions the near-surface air temperature does not accurately represent the temperature of the atmosphere. In this case, the temperature-dependent atmospheric background radiance algorithm underestimates the radiance from a clear sky. This is a possible explanation why during periods where both calibrations compare well, neither compares well with the simulated background. The internal-shutter-based calibration is consistently higher than the calculated background radiance, where the blackbody-based correction has periods of being both higher than and lower than the background. The consistent higher radiance during a time period where the atmospheric emission routines are expected to under-calculate the background radiance suggests that the shutter-based calibration was producing the expected data. Thus, it is believed that the internal-shutter-based calibration will provide adequately calibrated data for cloud detection. Despite the inversion, during this experiment the internal-shutter calibration gave mean radiance within 2 $W \cdot m^{-2} \cdot sr^{-1}$ of the clear-sky radiance except during periods where clouds were present. Based on these experiments it was determined that the shutter based calibration was capable of providing an on-deployment calibration for these systems.

Deployment at Table Mountain

With the proven ability of the internal-shutter-based calibration to provide cloud detection, this calibration method was used during deployment of the 50° fov second-generation ICI at the TMF from December 2006 through May 2007. The availability of accurately calibrated data from this deployment demonstrated the capability of operating over an extended time period while using the internal shutter as a blackbody source.

Extensive processing of the data from this deployment has not taken place; however, some processing of select times has taken place. Water vapor measurements were acquired from an Aerosol Network (AERONET) solar radiometer located at the TMF. The solar radiometer measurements were highly sporadic and thus were used to update a Reitan relationship equation to provided water vapor information between the gaps in the data. Air-temperature and dew-point temperature were acquired from a weather station located at TMF. The cloud threshold used for these data was a value of 2 W·m^{-2}·sr^{-1}. Figures 4-8 and 4-9 show processed images from this deployment.

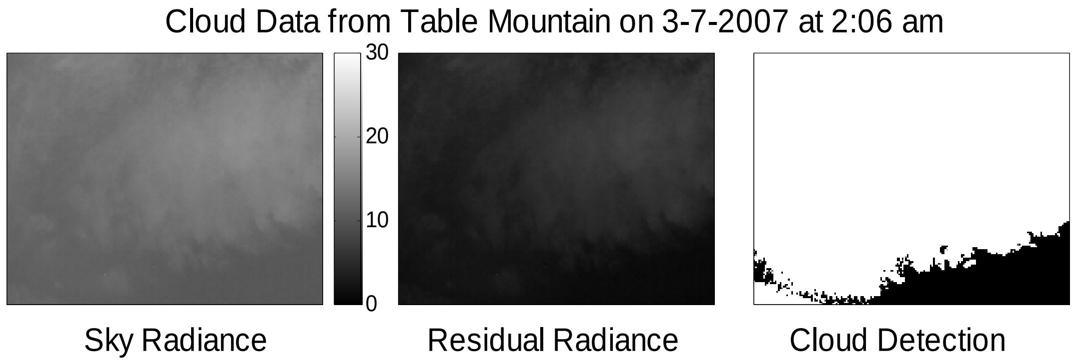
Cloud Data from Table Mountain on 3-7-2007 at 2:06 am

Sky Radiance

Residual Radiance

Cloud Detection

Figure 4-8. Processed 50° fov data from the JPL Table Mountain Facility, showing a sky nearly overcast with thin cirrus clouds.

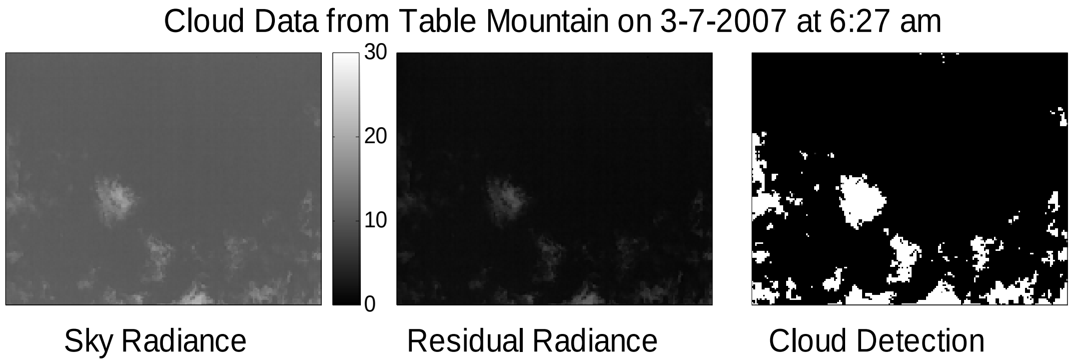
Cloud Data from Table Mountain on 3-7-2007 at 6:27 am

Sky Radiance

Residual Radiance

Cloud Detection

Figure 4-9. Processed 50° fov data from JPL Table mountain facility showing scattered thin clouds.

Most of the data from the TMF deployment has not been sent to MSU for processing, and is not expected to be. Rather, these data are being used by the Optical Communications Group at NASA JPL. The data examples presented here are intended to demonstrate that the second-generation ICI systems can operate using the internal shutter as a calibration source. This type of calibration appears to be possible even during extended deployments, such as this deployment at TMF.

Fall 2007 Deployment at Bozeman MT

The 50° fov camera was returned to Bozeman after the deployment at the TMF for recalibration and testing, along with the newly acquired 100° fov camera. Both these cameras were calibrated successfully. With calibrations completed, prototype second-generation ICI systems were constructed to allow for comparisons between these two cameras. Both these prototypes systems were run without the aid of an external blackbody calibration target, rather they used an internal-shutter-based calibration.

Originally these data were to be compared with data from the first-generation ICI system. However, the camera in the first-generation ICI failed shortly after its return from the deployment at Poker Flat Research Range in AK, and these comparisons could not be made. Instead, it was determined that the two cameras would be compared to each other, and simulated clear-sky radiance based on radiosonde profiles would provide a standard to which the comparison could be made. This was not the ideal comparison, but it was determined to be adequate for determining the calibration accuracy of the two systems.

The Optical Communications Group at NASA JPL had elected to run the 50° fov system in a weather-hardened enclosure to allow for continuous deployment of the system. The prototype 50° fov system is shown inside the enclosure in Figure 4-10. The enclosure is the cylindrical object on the right, and the box on the left is a weather-proof box that contains electrical components needed to run the system.

Figure 4-10. Prototype of the 50° fov second-generation ICI during the 2007 deployment at Bozeman, MT. The camera is inside the enclosure on the right and the electronics are in the box on the left. In the photo the front plate with the IR window is on the enclosure. (Photo by J. Shaw)

The camera looked out the enclosure through a germanium window. There is a reflectance off the window that causes narcissus (the camera sees the scene but also a small reflectance of itself off the window). Removing this reflectance term has proven to be difficult, so a second front plate was constructed that had an air gap in place of the window. This allowed for the camera to directly view the scene and make for easier comparisons between the two cameras. The system was run in this mode during the time periods when accurate comparisons with the 100° fov system were desired.

The prototype of the 100° fov system was much simpler. The 100° fov camera and necessary electronics were placed on a telescope mount and pointed at the sky. The camera was wrapped in a thin layer of insulation to keep the camera from getting too cold, and to also prevent any rapid temperature changes. The telescope mount was used to provide accurate pointing of the camera at a zero zenith angle. This was needed because of the strong angular dependence of the atmospheric emission removal routines, owing to the wide field of view for this system. Figure 4-11 shows this prototype 100° fov second-generation ICI during its deployment in Bozeman MT.

Figure 4-11. Prototype of the 100° fov second-generation ICI during the 2007 deployment at Bozeman, MT. The camera has been wrapped in insulation to reduce the likelihood of rapid temperature changes. (Photo by P. Nugent)

Data were taken with these two prototype second-generation ICI systems in Bozeman, MT during the first two weeks of October 2007. When referring to the data from each camera, the 50° fov camera will be referred to as Camera A, and the 100° fov camera will be referred to as Camera B. This is done to avoid confusion when talking about a 50° fov section of the 100° fov data. During this deployment the 50° fov system was run both with and without the front window. This allowed for both an accurate comparison with the 100° fov system and an approximate determination of the magnitude of the bias caused by reflections from the window. The configuration of the 100° fov was not changed in any manner during this deployment. Precipitable water vapor measurements were provided during these deployments by radiosondes launched from the site at which the cameras were running, along with near-surface air temperature and dew-point temperature readings. The following sections present the data from these experiments along with the additional processing required to make these comparisons.

Cloud Type Detection

The detection of cloud type has been talked about as a possible capability of the ICI systems since the development of the first-generation system. Knowing cloud type can help estimate the cloud optical depth at a communication laser wavelength when the system is used to study Earth-space optical communication paths. The capability of identifying cloud type is also highly desirable for climate research, especially when studying aspects of climate such as cloud radiative forcing [*Shupe and Intrieri 2004*].

To detect cloud type, a multi-level cloud threshold is used. To determine these threshold levels, MODTRAN models were run based on a 1976 standard atmosphere with standard cloud models. Various cloud types, cloud thicknesses, and cloud altitudes were simulated. The upward-viewing narrow-field-of-view integrated radiance was determined using each camera’s bandwidth. Measurements at the zenith were used to avoid any angular dependence of cloud integrated radiance. Once the total radiance was determined, the magnitude of the cloud emission was observed for the different cloud types. The cloud emission or radiance is the difference between the simulated cloud-containing atmosphere and the simulated clear-sky atmosphere. The results of these MODTRAN simulations are shown in Table 4-1 for Camera A (50° fov system) and Table 4-2 for Camera B (100° fov system).

Table 4-1 : Camera-A simulated cloud radiance

Cloud Type	Total Integrated Radiance $[W\cdot m^{-2}\cdot sr^{-1}]$	Cloud Radiance $[W\cdot m^{-2}\cdot sr^{-1}]$
Clear Sky	7.80	0.00
Very Thin Cirrus 9 km	9.05	1.25
Cirrus 9 km	9.78	1.98
Cirrus 4 km	12.08	4.28
Semi-Thick Cirrus 4 km	15.39	7.59
AltoStratus 5 km	21.88	14.08
AltoStratus 2400 m	28.04	20.24
Cumulus 3 km	26.24	18.44
Cumulus 1 km	31.78	23.98
Cumulus Low	33.04	25.24
Stratus	33.62	25.82
NimboStratus	34.30	26.50
StratoCumulus	32.90	25.10

Table 4-2: Camera-B simulated cloud radiance

Cloud Type	Total Integrated Radiance $[W\cdot m^{-2}\cdot sr^{-1}]$	Cloud Radiance $[W\cdot m^{-2}\cdot sr^{-1}]$
Clear Sky	6.39	0.00
Very Thin Cirrus 9 km	7.53	1.15
Cirrus 9 km	8.21	1.82
Cirrus 4 km	10.35	3.96
Semi Thick Cirrus 4 km	13.41	7.02
AltoStratus 5 km	19.39	13.01
AltoStratus 2400 m	25.13	18.74
Cumulus 3 km	23.46	17.07
Cumulus 1 km	28.61	22.22
Cumulus Low	29.77	23.39
Stratus	30.31	23.92
NimboStratus	30.94	24.55
StratoCumulus	29.65	23.26

From these data it was determined that there existed a difference in the integrated radiance for the two different systems when viewing the same cloud type. This difference is caused by the different spectral bandwidths of the two systems. It was determined that a single cloud-type multi-level-threshold could not be used and a unique set of thresholds were needed for each camera. These threshold sets, along with the cloud type detected, are shown in Table 4-3 for the 50 fov Camera A system, and Table 4-4 for the 100 fov Camera B system. Improvements could be made to include other cloud types based on application specific needs, and to develop a set of angularly dependent thresholds.

Table 4-3: Camera A Multi-level thresholds used for cloud type detection

Cloud Type	Cloud Radiance Threshold [$W\cdot m^{-2}\cdot sr^{-1}$]
Clear Sky	< 2
Thin Cirrus	2
Cirrus	4.5
Mid-level Clouds	9
Semi-Thick Clouds	13
Thick Clouds	22

Table 4-4: Camera B Multi-level thresholds used for cloud type detection

Cloud Type	Cloud Radiance Threshold [$W\cdot m^{-2}\cdot sr^{-1}$]
Clear Sky	< 1.8
Thin Cirrus	1.8
Cirrus	4
Mid-level Clouds	8
Semi-Thick Clouds	12
Thick Clouds	20

<u>Second-Generation ICI Camera Comparisons</u>

The side-by-side deployment of the two second-generation ICI systems at Bozeman MT during October 2007 allowed for a comparison between these systems. The calibrated radiance observed by each of these systems when viewing the same scene was analyzed within the region of overlap between the fields of view for the two systems. The average radiance across this overlapping field of view was compared for each camera.

Bandwidth Difference Problems: This comparison could not be made directly because, as the MODTRAN cloud type simulations had shown, the two cameras are not expected to measure the same radiance even when viewing the same scene. This happens because the two cameras view the scene over different bandwidths because of the different lenses used in each system. This occurs even after calibration, as the calibrations are performed in terms of radiance integrated over each camera's unique bandwidth. Thus, with different bandwidths the cameras will see different integrated radiance.

To avoid this problem, a conversion routine was made to convert the Camera A measured radiance to an equivalent Camera B measured radiance. This conversion was built using the difference between the Cloud Radiance, after removal of clear-sky emission, for Camera A and Camera B from the MODTRAN cloud simulations. Then a linear fit was made between this difference and the total Camera A radiance. This correction function allows for conversion of Camera A measured radiance, L_A, to an equivalent Camera B measured radiance, L_{BE}. This allowed for comparisons to be made between the two cameras when viewing the same scene. Figure 4-12 shows the difference data along with the linear fit to these data. The resulting linear equation is shown in Equation 4.1.

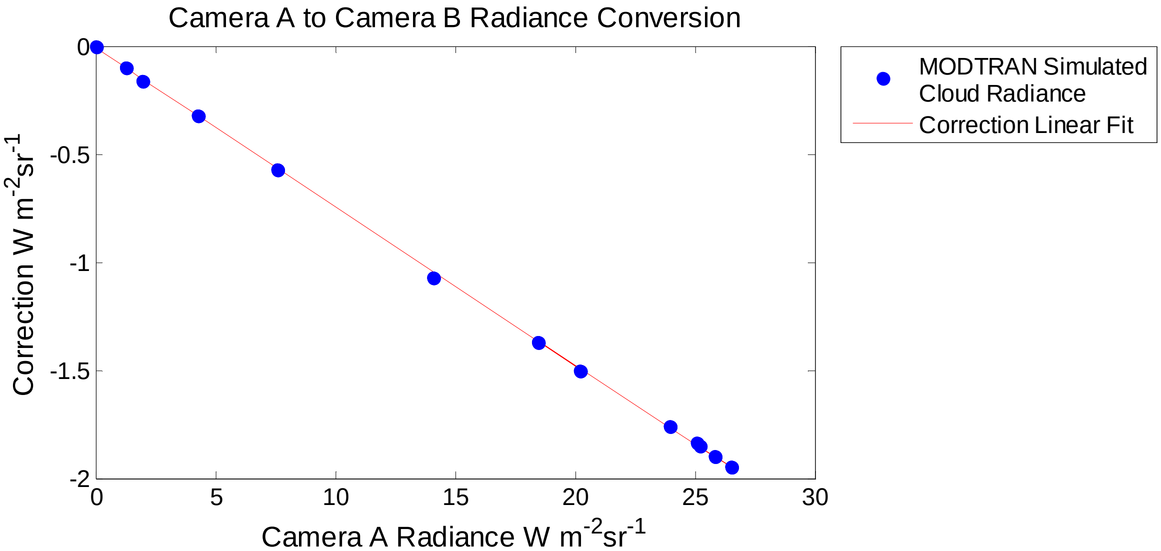

Figure 4-12. Scatter plot of the difference between Camera-A and Camera-B integrated radiance for Camera-A radiance (blue dots). The red line is a fit to these data that can be used to convert Camera-A radiance to an equivalent Camera-B radiance.

$$L_{BE} = L_A - 0.07317 L_A - 0.0122 \ [\mathrm{W \cdot m^{-2} \cdot sr^{-1}}] \qquad (4.1)$$

<u>Comparisons of the Second-Generation ICI Systems:</u> With the ability to convert between a Camera-A radiance and a Camera-B radiance, the two systems could be compared. The process of the comparison is as follows: 1) calculate and remove atmospheric emission using each camera's respective atmospheric emission equation, precipitable water vapor, and near-surface air temperature, 2) use the Equation 4.1 to convert Camera-A radiance to equivalent Camera-B radiance, 3) take the difference between the equivalent Camera-B radiance and the actual Camera-B radiance. This comparison was conducted for both Camera A viewing the scene through the germanium window on the enclosure, and for Camera A viewing the scene directly with no window. Figure 4-13 shows data from 10-02-2007, a time period when Camera A was operating through the germanium window. Figure 4-14 shows data from 10-04-2007, a time period

where Camera A viewed the scene directly. For both theses time periods Camera B viewed the scene directly.

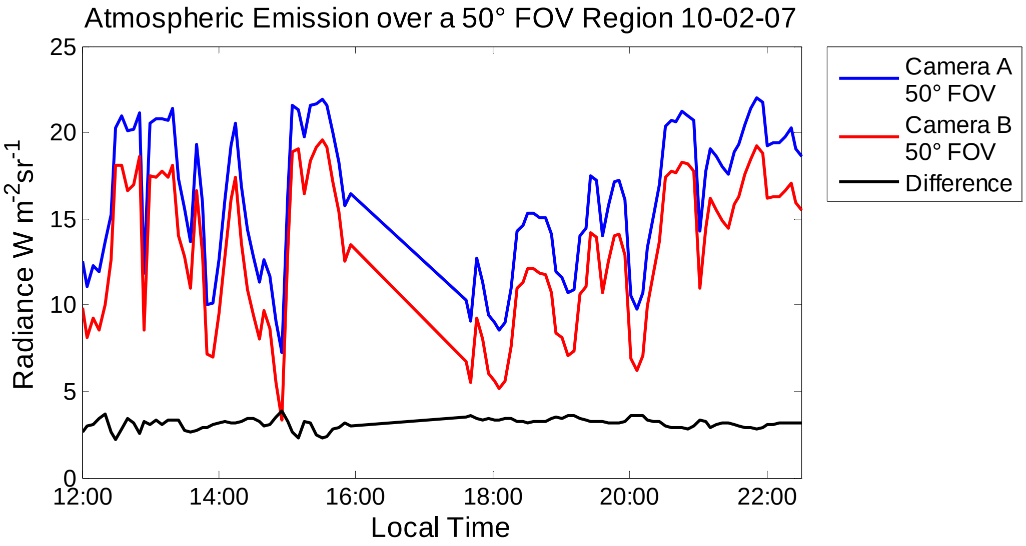

Figure 4-13. The average radiance across the full 50° fov of the Camera A system, and a cropped 50° fov from the Camera B system. For these data Camera A viewed the scene through the germanium window. Mean Calibration Difference = 3.1469 W·m^{-2}·sr^{-1}

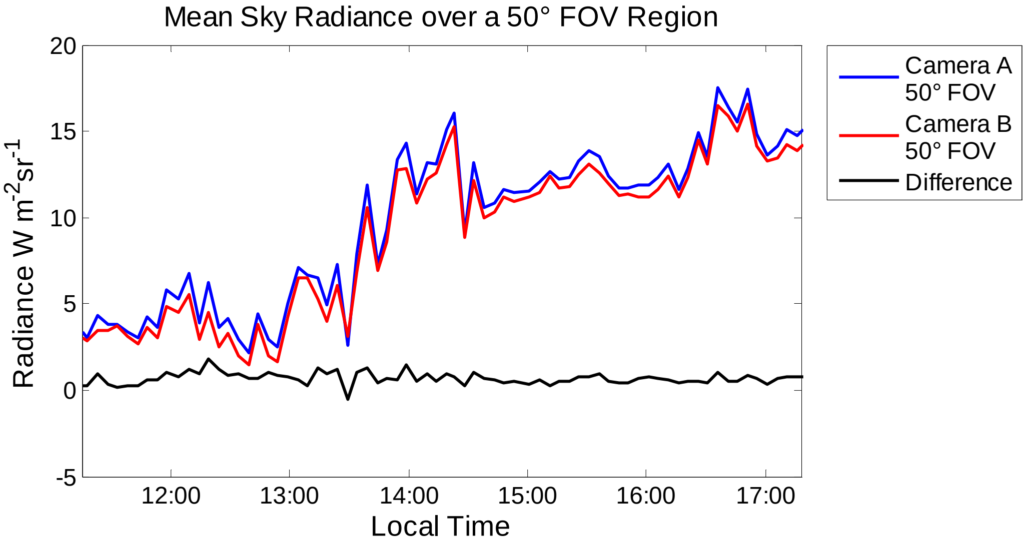

Figure 4-14. The average radiance over a matched field-of-view with both systems viewing the scene directly. The mean calibration difference during thie experiment was, 0.686 W·m^{-2}·sr^{-1}.

These comparisons show that when directly viewing the overhead sky across a matched field-of-view, both systems agree closely, within 0.686 $W \cdot m^{-2} \cdot sr^{-1}$. This difference is within the calibration uncertainty of the two systems, and could easily be accounted for by the uncertainties of the bandwidths for the two systems. However, when Camera A views the scene through the germanium window there is an additional background signal on this camera, approximately 2 to 3 $W \cdot m^{-2} \cdot sr^{-1}$. This is not an absolute determination of the magnitude of this signal, but rather a demonstration that this signal exists. If the system is to be run viewing the scene through the germanium window, then the magnitude of this signal and the variation of this signal with time would need to be determined more accurately.

<u>Clear-Sky Comparisons with Theory:</u> These experiments have demonstrated that the two systems are, within the accuracy achievable, co-calibrated. This does not, however, determine the accuracy of the calibration. To determine the level of calibration, a day when an extended period of completely clear skies was selected and the measured clear-sky radiance was compared to a calculated clear-sky radiance using the atmospheric emission equations and radiosonde measurements. This day was 10-11-2007, during which calibrated data from Camera A were not available, but Camera B data were. During this time period the sky was not completely clear, as thin cirrus clouds and small broken low-altitude thin clouds were observed.

To select regions of the image that were primarily clear sky, the data were sorted and the average of the lower quarter of the data across the entire 100° fov was calculated. These calibrated data, along with the calculated atmospheric emission which corresponded to these data, are shown in Figure 4-15. The sky was visibly clear (possible sub-visual cirrus) during a time period between 9:30 and 10:30 and for time periods around 11:00, 12:00, 14:30, and 15:40. During these time periods the camera reported a very small level of average calibrated radiance that corresponds well with the calculated atmospheric radiance, to within ±0.5 $W \cdot m^{-2} \cdot sr^{-1}$. These data demonstrate the calibration of the system to be within the level of accuracy expected from the calibration uncertainties, as described in chapter 3, and the atmospheric radiance removal algorithms, as described in chapter 2.

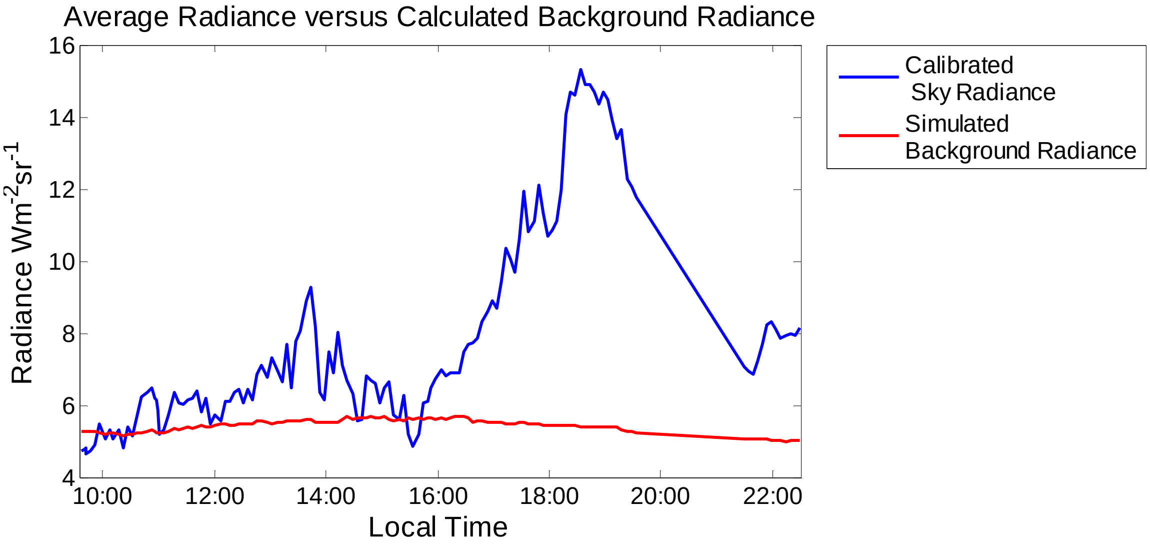

Figure 4-15. Camera-B scene radiance compared to simulated clear-sky radiance. Good agreement is seen during clear time periods between 9:30 and 10:30 and around 11:00, 12:00, 14:30, and 15:40.

<u>Loss of Calibration on the 50° fov System:</u> During the October experiments the calibration for the 50° fov second-generation ICI (Camera A) was lost. This loss of calibration limited data set for both cameras running side by side with good calibration to two days, October 2nd, 2007, and October 4th, 2007. On October 10th cold weather caused

dew to form inside the enclosure. The system was dried, but the calibration had been lost. Figure 4-16 shows a comparison between the 50° region of overlap for both systems on 10-11-2007, after the calibration was lost. In this figure the Camera A to Camera B radiance conversion, Equation 4.1 has been applied to the Camera A data.

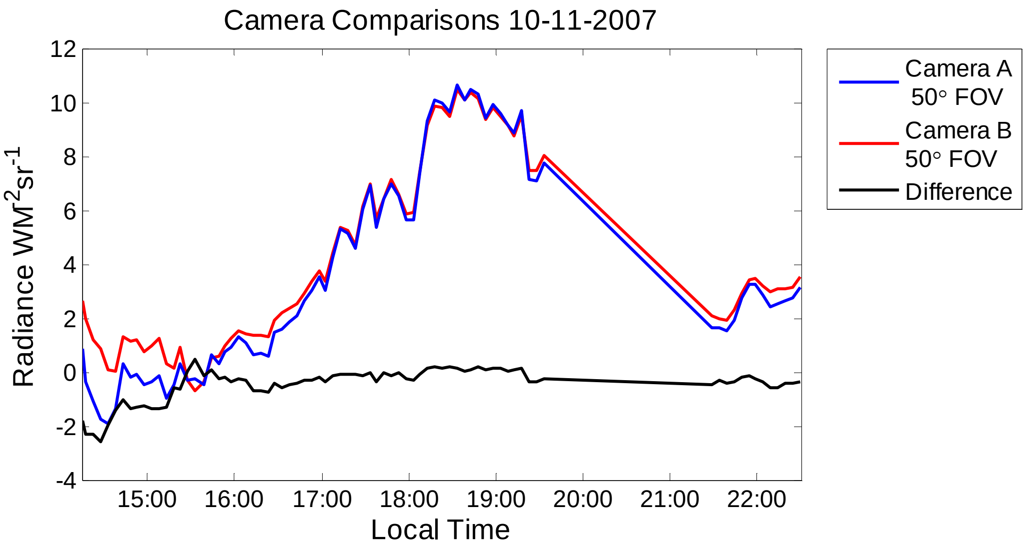

Figure 4-16. Comparisons between Camera A (blue) and Camera B (red) after the loss of calibration for Camera A. The difference between the two cameras is no longer constant, suggesting a bandwidth change in the Camera A lens due to dew inside the lens.

During this day Camera A reported lower radiance than Camera B, the opposite from what was observed before. This is significant during time periods of thin clouds and clear sky, such as from 14:15 to 15:30. This difference is not consistent with time, unlike previous experiments, shown Figures 4-13 and 4-14. It is likely that a thin film left on the lens elements slightly changes the overall transmission of the lens. Recalibration of this system should account for much if not all of these changes. Problems can be avoided in the future by running the heater that is located inside the enclosure. Another precaution that could be taken is to keep the air inside the enclosure dry either by filling the enclosure with dry nitrogen or placing a desiccant pack inside the enclosure.

Data Processing and Results

As shown in Table 4-3 and 4-4, unique thresholds for each camera can be used to provide cloud presence detection along with cloud type detection. These thresholds were used to build a multi-threshold processing routine which is shown in Figure 4-17.

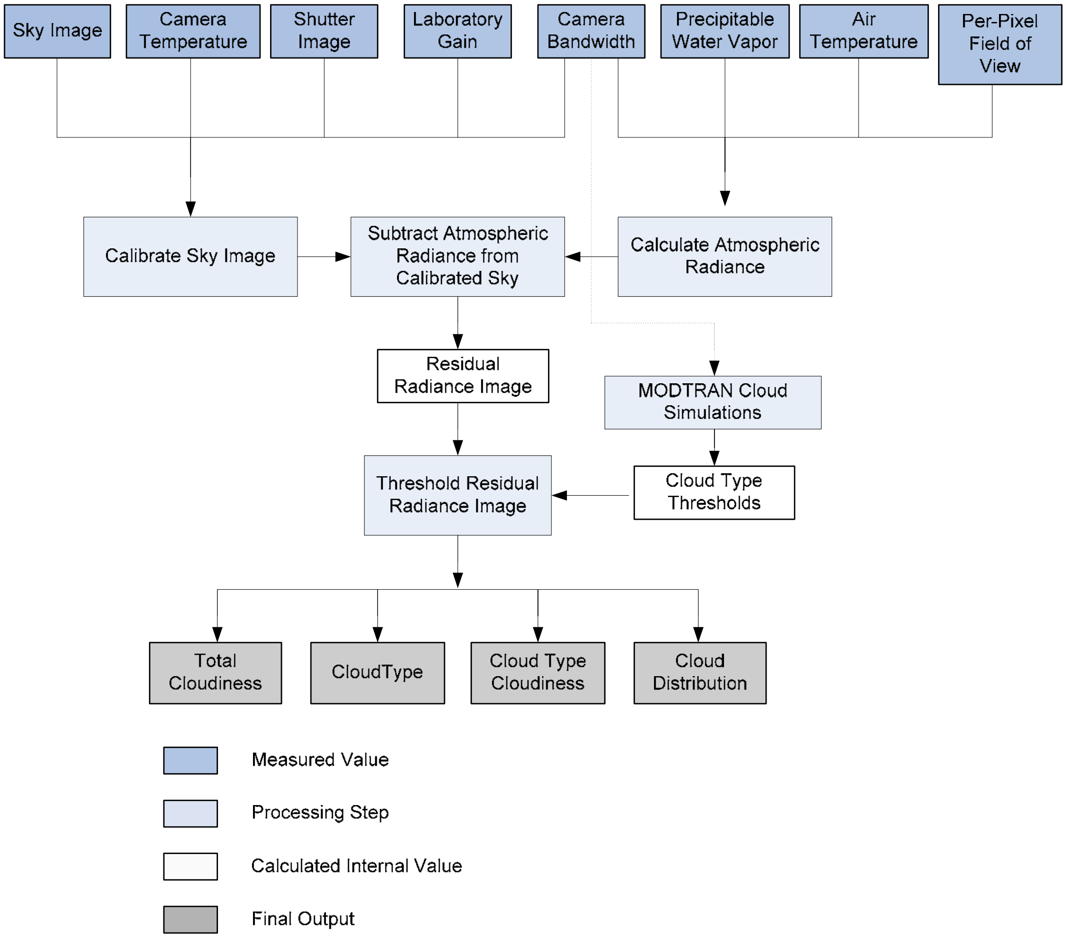

Figure 4-17. The expanded data processing routine. This routine uses a measured camera bandwidth along with a measured per-pixel field of view, and produces additional information about the overhead clouds including cloud type.

Unlike the routine used for the 2006 data this routine used a measured camera bandwidth along with a measured per-pixel field of view unique to each camera. This routine produces information about: the total amount of overhead cloud cover, cloud type classification, cloudiness separated by cloud type, and the cloud spatial distribution.

Spatial Cloud Detection Comparisons: The processing routine outlined in Figure 4-17 was used to process the data from October 4th, 2007. These data are from the only day over which both cameras were operating and Camera A was operating without the germanium window on the enclosure, for most of the day. Luckily, this day provided a variety of clouds, ranging from thin high-altitude cirrus clouds to thick low-altitude broken clouds. Figures 4-18 through 4-22 show sets of three-panel figures for times when both systems were running side by side. These three-panel figures show the processing routine for these data, the left panel is the calibrated sky radiance data, the center panel is the residual radiance after the removal of atmospheric emission, and the right panel is the cloud detection image using the multi-level cloud threshold unique to each camera. For these data the full 50° fov of the Camera A system, the top three-panel series, and the full 100° fov of the Camera B system, the bottom series, are presented. The Camera A system ran without the germanium window during this experiment except for a period from 10:00 to 11:15. Four of the five following data sets are outside of this time period, however the data from 10:13, shown in Figure 4-18, the germanium window was on the Camera A enclosure. To make these data compare a bias of 4.2 $W \cdot m^{-2} \cdot sr^{-1}$ was subtracted from the Camera A data. The other data sets, Figures 4-19 to 4-22, the enclosure window had been removed and no modifications needed to be made to these data.

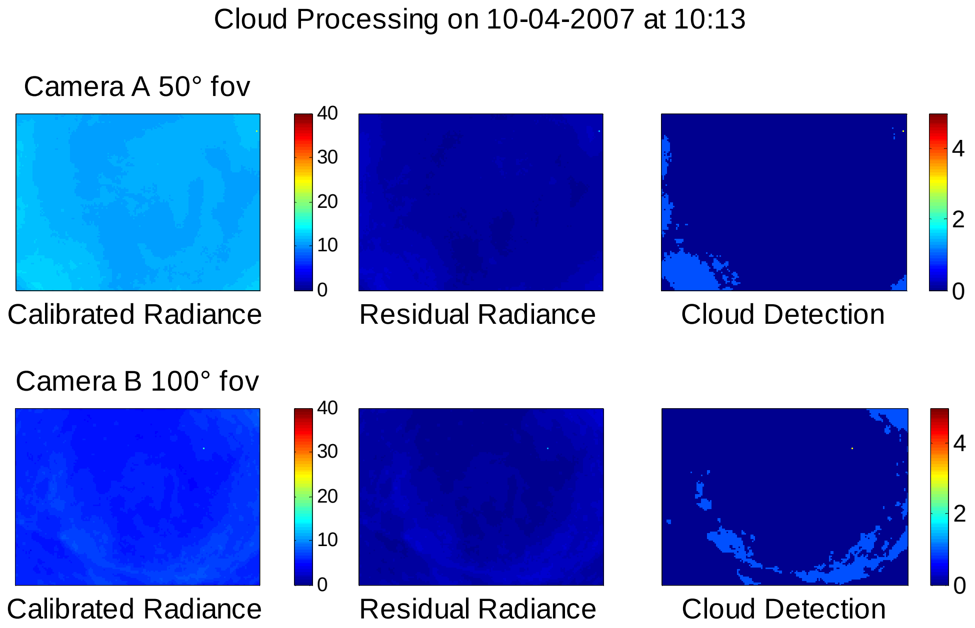

Figure 4-18. Detection of thin wispy cirrus clouds. The top series shows the cloud processing for the 50° fov Camera A, and the bottom series shows the 100 fov Camera B data. Each series is of the following: calibrated sky radiance (left), residual radiance (center), and cloud detection (right). The object in right hand corner of the images is the moon.

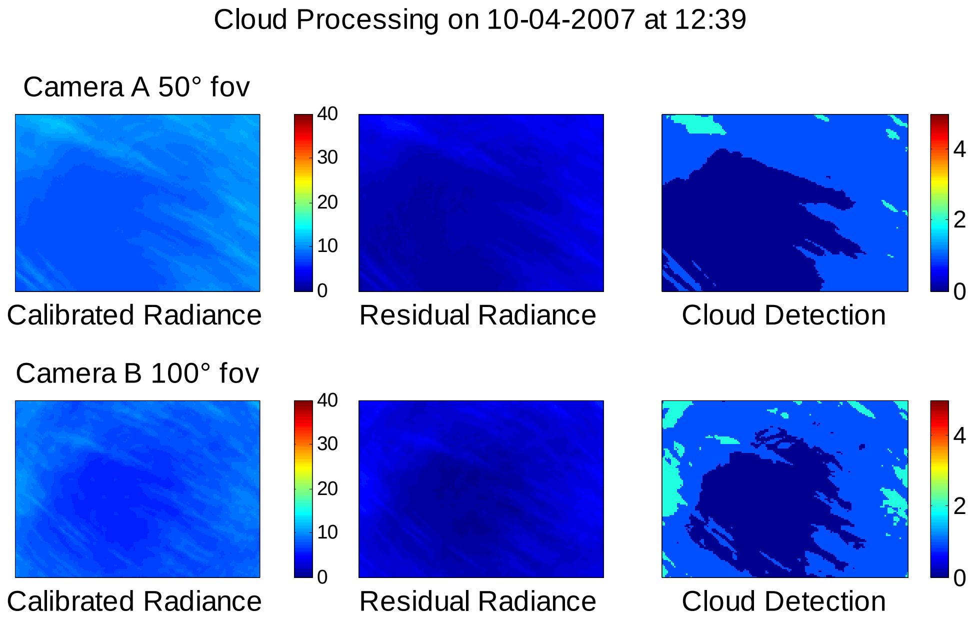

Figure 4-19. These images show thin wispy clouds with a hole near the center. Both cameras detect this hole, and show largely the same shape. The detection of thick clouds around the edges of the 100 fov camera may be due to the emission from cirrus clouds increasing with zenith angle

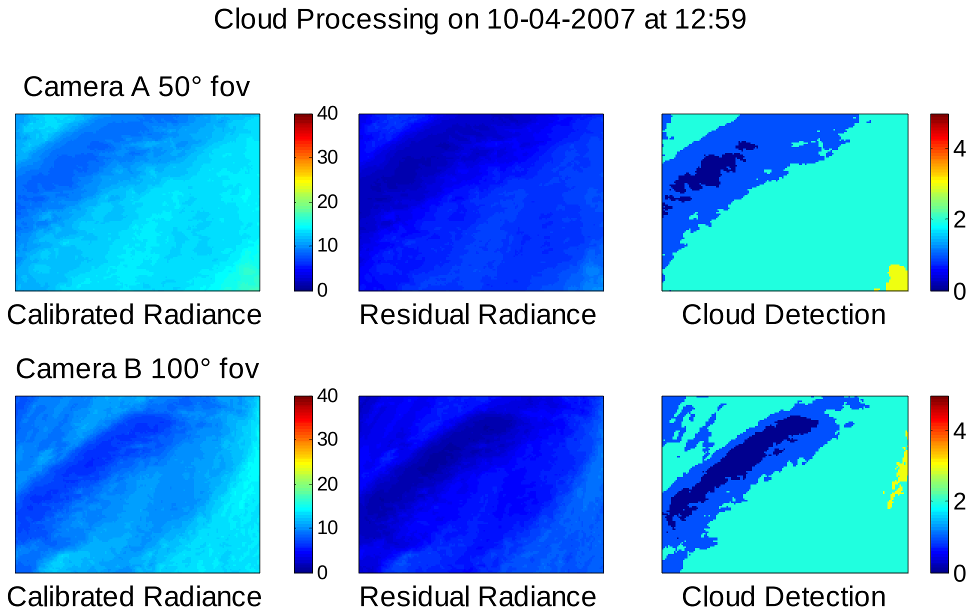

Cloud Processing on 10-04-2007 at 12:59

Camera A 50° fov

Calibrated Radiance

Residual Radiance

Cloud Detection

Camera B 100° fov

Calibrated Radiance

Residual Radiance

Cloud Detection

Figure 4-20. These images show cirrus clouds with a sligh wavelike structure shown by the thin long hole extending across the images. Looking at this hole over the matched fov regions, the center two-thirds of the 100° fov image, the region of clear sky the Camera A system reports less clear sky were the Camera B system reports a larger clear region.

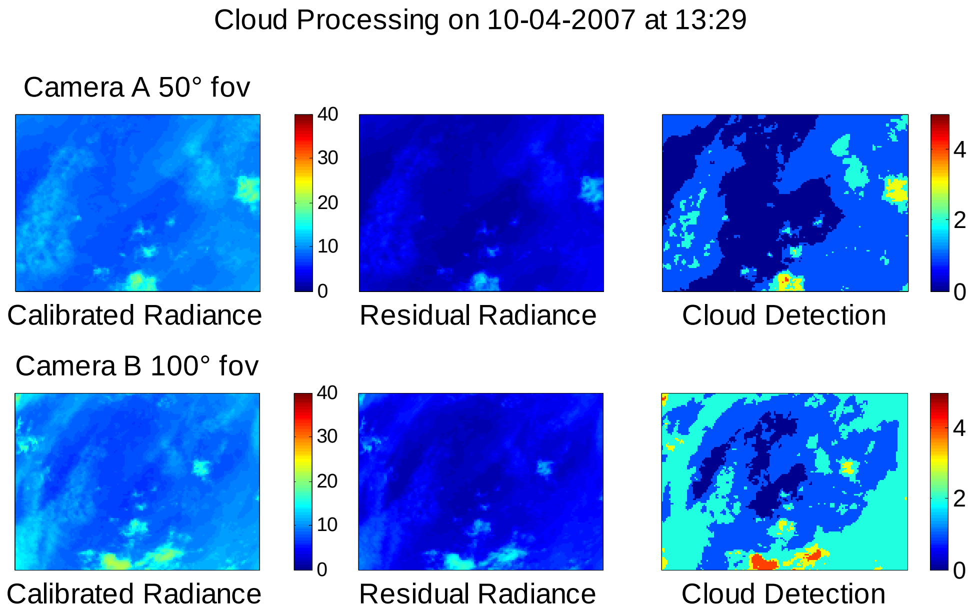

Cloud Processing on 10-04-2007 at 13:29

Camera A 50° fov

Calibrated Radiance

Residual Radiance

Cloud Detection

Camera B 100° fov

Calibrated Radiance

Residual Radiance

Cloud Detection

Figure 4-21. This figure shows a mixture of both thin and small low-altitude clouds, the warmer clouds in the images. It is of interest to note, that in this image the Camera B system reports more thin clouds over the matched fov. This is the opposite trend as observed in Figure 4-22.

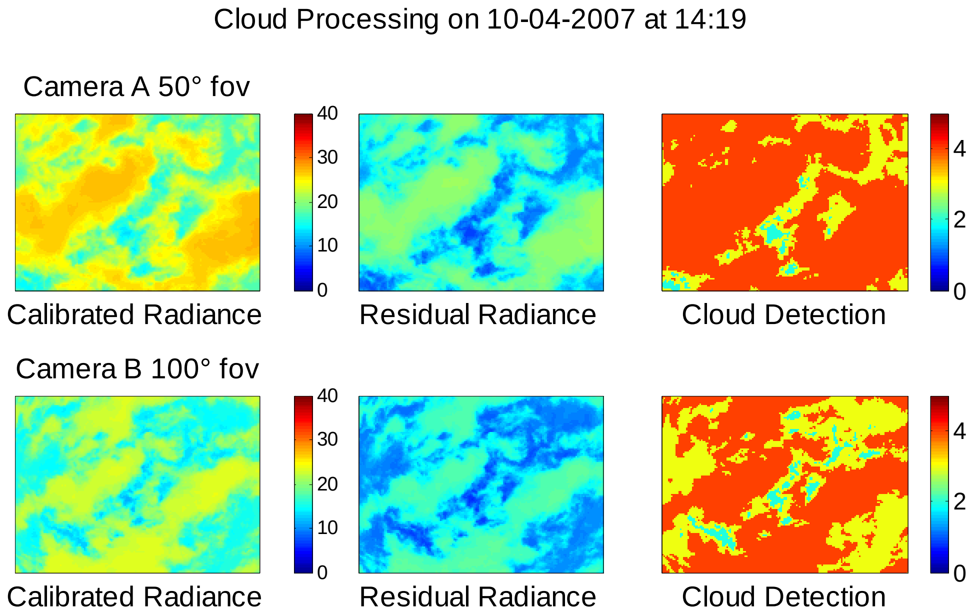

Figure 4-22. These images show the thick clouds that moved in as the experiment progressed. Both systems detect nearly identical cloud types, and cloud amounts. It is of interest to note the fractal nature of these clouds. Both images look very similar, even though the bottom image from Camera B is over a wider fov.

These data have demonstrated the ability of both these systems to provide accurate cloud cover statistics. For much of these data both cameras detected the same cloud types and cloud amounts over the 50 overlapping fov. In some cases such as in Figure 4-21 the Camera B system detects clouds where the Camera A detects clear sky, in Figure 4-20 the opposite trend is observed. This suggests that there is not a systematic bias between the systems. Rather in both these cases these thin clouds are near the minimum detection threshold of these systems. Thus, accurate cloud detection is very dependent on the calibration accuracy of the cameras, and the removal of the atmospheric emission. It is therefore expected that on an instantaneous time scale these cameras will provide slightly different cloud amounts as the ±0.61 $W \cdot m^{-2} \cdot sr^{-1}$ for the 50° fov system, and the ±0.76 $W \cdot m^{-2} \cdot sr^{-1}$ of the 100° fov system causes the detection of clouds near this threshold to vary. Overall the ability of these systems to compare well with each other in their ability to detect cloud presence and cloud type has been demonstrated. This demonstrated the accuracy of the calibration and processing routines used in this project, as two different cameras with differing: bandwidths, lenses, fov, and sensitivity have been successfully co-calibrated.

Temporal Cloud Amount Comparisons: Rather than analyzing the spatial statistics of the data, a value of total cloud amount can also be calculated for each image and the temporal statistics of the cloud-amount time series can be analyzed. For these data, cloud amount is defined as the percentage of pixels above the selected cloud threshold. An example time-series plot of such data for October 4th, 2007 is shown in Figure 4-23, and the corresponding percent-cloudiness values computed over the entire experiment time are shown in Table 4-5.

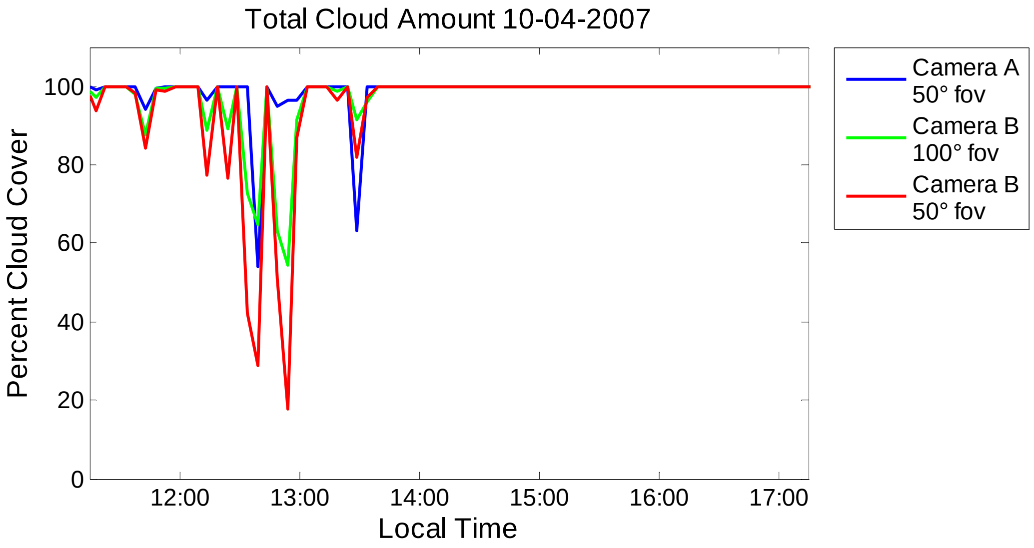

Figure 4-23. Total cloudiness observed by the second-generation ICI systems on October 4th, 2007. The data cover the entire fov for the Camera-A system (blue) and both the entire fov (red) and the center 50° (green) of the Camera-B system.

Table 4-5: Mean cloudiness on 10-04-2007

ICI System	Percent Mean Daily Cloudiness
Camera A 50° fov	98.6%
Camera B 50° fov	94.9%
Camera B 100° fov	97.1%

These data largely agree, except for a time period between 12:30 and 14:00, during the times the Camera B center 50° fov reports nearly clear at times where Camera A reports nearly overcast skies. This suggests that the clouds during this time period have cloud radiance near the minimum cloud detection thresholds for each camera. Over the total experiment the Camera-B center 50° fov reported the lowest cloudiness of 94.9%, 3.7% less than the cloudiness reported by the Camera-A system in the same fov. This suggests that the cloud detection thresholds for the cameras could still be adjusted so that the amount of clouds detected is the same.

Using the multi-value cloud threshold, the total cloud amount data can be separated into cloud-type statistics. Such data from October 4th 2007 taken over the overlapping 50° fov of each system is shown in Figures 4-24 (Camera A) and 4-25 (Camera B). In this case, the plot shows percentage of pixels with: thin clouds (type 1 and type 2 or 1.8 to 8 $W \cdot m^{-2} \cdot sr^{-1}$ Camera B, and 2 to 9 $W \cdot m^{-2} \cdot sr^{-1}$ for Camera A), thick clouds (type 3 to type 5 clouds or greater than 8 $W \cdot m^{-2} \cdot sr^{-1}$ for Camera B and greater than 9 $W \cdot m^{-2} \cdot sr^{-1}$ for Camera A), and total cloud amount (thin + thick).

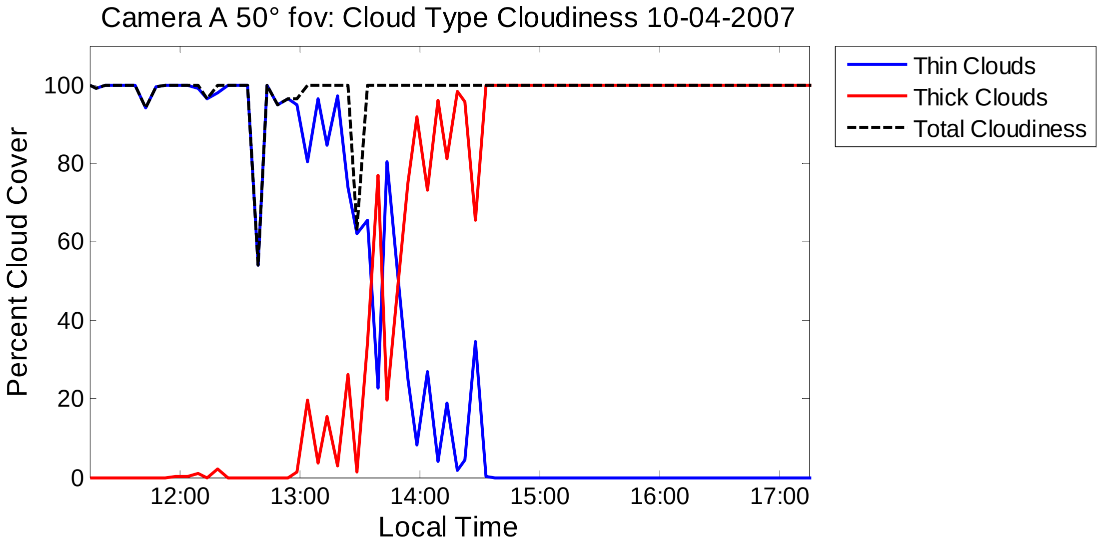

Figure 4-24. Cloud type with time for the Camera-A system full fov. Total cloudiness is largely constant over the experimental period, but there is a distinct change from thin clouds to thick clouds between 13:00 and 14:00 local time.

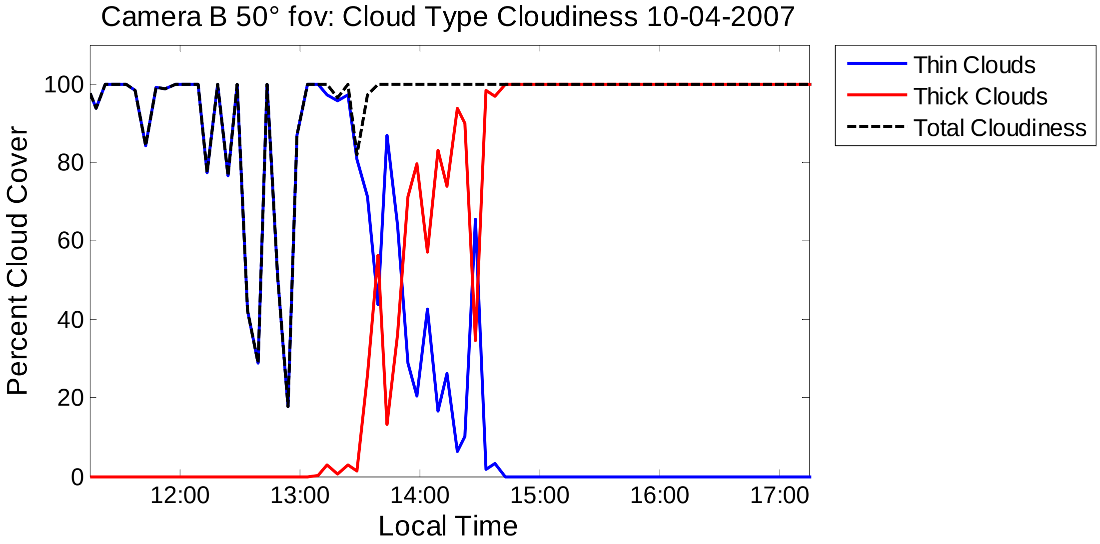

Figure 4-25. Cloud type with time for the center 50° of the Camera-B fov over the same time period as Figure 4-24. This system misses clouds during a time period from 12:00 to 13:00 that the Camera A system detects. The transition from thin clouds to thick clouds is still highly apparent, but appears to take place at a time period shifted by 30 minutes.

The importance of cloud-type information can be seen in these figures. Although the total cloud amount is largely constant throughout the day, this cloud amount is caused by distinctly different types of clouds, with thin clouds early on being replaced by thicker clouds as the experiment progressed. This distinct change from thin clouds to thick clouds takes place between 13:30 and 14:30 local time. Both systems detect this change in cloud type over nearly the same time periods, however the dynamics of this change appears slightly difference as observed by each system. During this experiment the cloudiness as measured by each camera is largely constant. However the Camera-B system misses clouds during a time period from 12:00 to 13:00 that the Camera-A system detects. These differences in the observed cloud amount and cloud type classification between these two systems suggest that the cloud detection thresholds used for the camera systems can be improved to provide more consistent cloud measurements.

Radiative Forcing Measurements: Another capability of these systems is the measurement of the Long-Wave downwelling cloud irradiance [W m^{-2}], which can be used to study cloud dependent radiative forcing [*Shupe and Intrieri2004*]. The downwelling cloud irradiance measured during this time period measured in the entire 100° fov of the Camera-B system is shown in Figure 4-26. Cloud-dependent irradiance in this case is defined here as the spatial average of the full-image residual sky radiance multiplied by the projected solid angle of the camera's fov. During the time period of changing clouds, the cloud radiative forcing significantly increased from ~5 Wm^{-2} to ~20 Wm^{-2} even though the total amount of cloudy pixels did not change significantly.

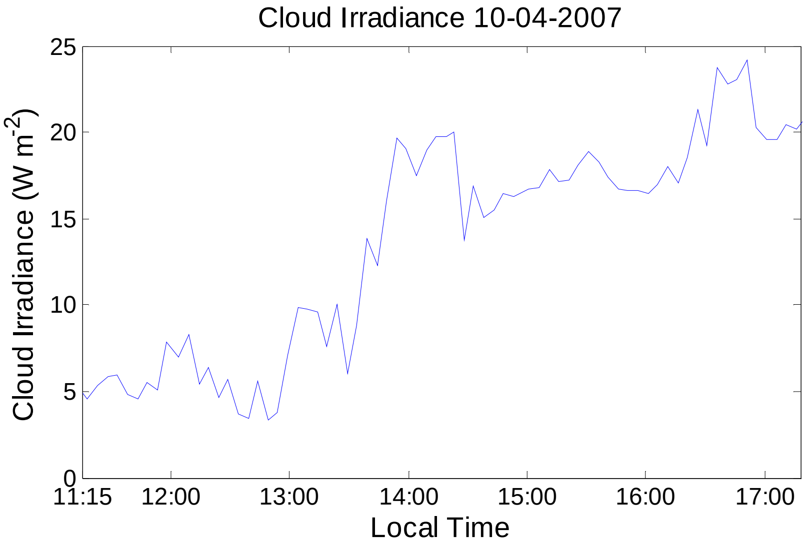

Figure 4-26. Cloud Irradiance (Wm^{-2}) measured over the whole 100° fov of the Camera-B system. During the period of cloud type change between 13:30 and 14:30, the cloud irradiance, and thus cloud radiative forcing, increases.

Applications for these Data

This project has focused on the development of these prototype second-generation ICI systems and the processing techniques needed to process the data from these systems. These data presented in this chapter, have demonstrated that techniques used in calibrating these cameras produce calibrated data and that the processing routines are able to distinguish between clouds and clear sky and between differing types of clouds.

One of the next steps in this project will be the application of these data to a scientific or engineering problem, such as the role of clouds in climate, or the characterization of optical communication paths. These data collected by the systems are of importance to the characterization of optical communication channels and to climate research. Cloud presence and spatial amount are important to any application where the detection of clouds is desired. Cloud type distinction is important to the characterization of optical communication channels, as thick clouds will block the signal, where thin clouds will attenuate the signal but may allow communication to take place. The bit-error rate of such communication would be expected to increase, but communication may still be achievable. This cloud type information is also important for climate research, in particular studies of the cloud-dependent radiative forcing. As was demonstrated in Figure 4-26 the radiative properties of clouds are dependent on the type of cloud, not just the total cloud amount. There are improvements that still can be made to the data processing routines to increase the quality of the data provided by these systems. Such higher quality data may be desired by some applications. However, these improvements can be made during a deployment of the system and should not hinder the application of these systems to scientific problems.

CONCLUSIONS

This research has focused on the development and testing of a set of second-generation ICI prototypes and the development of processing routines for the data provided by these systems. These imagers are based on the first-generation ICI system, but have extended this system to provide wider fields-of-view, 50° fov in one system and 100° fov in the latest, significantly reduced instrument size, and reduced instrument weight, and have reduced the overall cost of the instrument. To accomplish these improvements the imagers have been based on the FLIR Photon Core camera, with the addition of an after-market lens for the 100° fov system. Basing the imagers around this camera has dramatically reduced size and allowed the system to be redeployed at multiple locations with very little cost. Also, multiple versions of this instrument can be built at low cost. However, the use of this camera required careful development of temperature-compensation algorithms to maintain radiometric calibration with changing camera temperature.

Prototype versions of these compact ICI systems have been developed, calibrated, and demonstrated through deployments at MSU in Bozeman, MT and at JPL’s TMF. The development of a deployable and robust version of the 50° fov system is nearly complete. This system will be used by the Optical Communications Group at NASA JPL for their work in characterizing Earth-space optical communication paths. The feasibility of a deployable version of the 100° fov system has been demonstrated. However, construction of this system has not commenced.

Although these instruments have been built for the purpose of characterizing Earth-space optical communication paths, they are a cloud detection and classification instrument that need not be tied to this or any specific application. Rather, these instruments can easily be adapted for a wide variety of applications for which accurate localized cloud-cover statistics are required. Possible applications include, but are not limited to: climate studies, climate modeling, weather forecasting, Earth-space optical communication, validation of satellite cloud-clearing algorithms, Ka-band Earth-space communication, and many unforeseen applications where accurate cloud information is required on a 24-hour basis. The cloud statistics data from these imagers are also useful in characterizing the atmosphere for supporting other sensing systems, including passive and active remote sensors.

Contributions of This Project

These Long-Wave IR imagers are now ready to be used to measure local cloud cover statistics. With the use of a Long-Wave IR imaging detector, spatial cloud cover statistics can be determined directly, avoiding the problems that can arise through reliance on Taylor's hypothesis with zenith-only data. Infrared imaging does not depend on ambient sunlight or starlight and thus allows for a single method of gathering cloud data during both day and night, avoiding inconsistency caused by different methods for daytime and nighttime collection with visible-wavelength imaging. Infrared imaging can also be used during the sunrise and sunset periods of the day, providing a continuous data set through these important transition times.

The combination of an IR imaging detector, the use of fully calibrated data, and the processing routines unique to these systems work to provide important capability of measuring: cloud presence, cloud type, cloud spatial distribution, cloud radiative properties, and clear-sky radiative properties. Furthermore, these wide-angle imaging systems can be used to analyze cloudiness over large portions of the sky or smaller regions down to a single pixel. This has largely been made possible to measuring the per-pixel instantaneous field-of-view so that any angular region contained within this field of view can be selected.

The increased field of view of the ICI system, a requirement for both climate research and the characterization of optical communication paths, has been successful. This increase required that the processing of the data be changed. In particular, the atmospheric radiance removal routines needed to be adapted to account for per-pixel viewing angle across the detection. Accurate measurements of the per-pixel field of view and pointing angle were required for a full correction of atmospheric radiance over the entire fov. These measurements have been conducted using the distortion of a straight edge at known angles throughout each imager's full fov.

Climate-Related Cloud Detection

This project has led to the development of a system that can be applied to the study of clouds for the application to climate research. These systems have not yet been directly applied to this application, as the focus of work to date has been proving these systems and making the necessary improvements to apply these systems to the problem of clouds in climate.

Climate applications could include a wide variety of topics covering the radiative properties of clouds and their impact on climate. One such topic is cloud radiative forcing. These instruments can directly measure the long-wave downwelling radiation from the overhead cloud cover and also the cloud-type and spatial properties of the overhead cloud cover. The combination of these data could lead to increased understanding of the radiative properties of clouds and how to determine the net radiative forcing caused by cloud cover. These systems can also lead to improved capabilities in the validation of climate models through characterization of clouds at a single location on the Earth. Knowing cloud type and distribution at a single location could be used to improve the workings of these models through using the known data to set the parameters of climate models. The combination of cloud-base temperature data sets from the ICI with cloud-top data from on-orbit satellites could provide information about the in cloud temperature distributions. This could provide important information for modeling in cloud thermodynamic processes.

Earth-Space Optical Communication

The application of the ICI technique and data to the characterization of optical communication paths should take place with the deployment of these systems at JPL's TMF. Measuring cloud presence, distribution, and type will be needed for accurate characterization of the atmosphere over communication channels. This will require the development of the quantitative relationship between cloud types determined by the ICI and predicted fade statistics. It is believed that the cloud type, which relates to cloud optical thickness, as measured by the ICI could be used to predict the cloud optical depth and optical scattering at the optical wavelength used in the optical communication channel. This optical depth and optical scattering could then be related to the expected bit error rate of the communication signal.

Calibration of Infrared Imaging Systems

Another significant contribution of this project has been the development of unique techniques to provide radiometrically accurate real-time calibration of TEC-less infrared imaging systems. This calibration has largely been made possible by a two-part process. The first step was characterizing the FPA-temperature-dependent change in camera gain and camera offset over a temperature range from 15 °C to 30 °C. The second step was characterizing the radiometric differences between the camera viewing the internal shutter and an external blackbody at the same temperature as the internal shutter. This allowed for the internal shutter to be used as a blackbody to update the offset component of the camera's linear radiometric calibration equation. The use of the internal shutter in this method as a true radiometric calibration target is believed to be novel and unique work,and may allow for improved calibration of thermal-infrared cameras.

Quality of the Calibration

The calibration techniques used in this project have shown to produce a highly accurate calibration for these systems. For the 50° fov camera the radiometric calibration has been shown to be within ±0.36 $W\cdot m^{-2}\cdot sr^{-1}$ for most scenes. Due to the non-linear relationship between radiance and temperature this leads to a ±0.49 °C error for a 25 °C scene, a ±0.63 °C error for a 0 °C scene, and a ±2.4 °C for a -80 °C scene. For the 100° fov camera the calibration is stable to within ±0.51 $W\cdot m^{-2}\cdot sr^{-1}$. In temperature space this leads to errors of ±0.70 °C for a 25 °C scene, ±0.90 °C for a 0 °C scene, and ±5.4 °C for a -80 °C scene. On top of the calibration error there is the uncertainty of the atmospheric emission removal algorithms. These algorithms to day can calculate the atmospheric background to an accuracy of ±0.25 $W \cdot m^{-2} \cdot sr^{-1}$. These errors are independent and thus need be added as the sum of squares. This leads to a total expected error of ±0.44 $W \cdot m^{-2} \cdot sr^{-1}$ for the 50° fov system, and ±0.57 $W \cdot m^{-2} \cdot sr^{-1}$ for the 100° fov system. Thus, it is evident that the addition of the aftermarket lens to increase the fov comes with the trade off of increased calibration uncertainty. Despite this additional uncertainty in the wide fov system the overall level of calibration is within the levels required for cloud detection.

Types of Clouds that can be Observed

This uncertainty is the major determining factor for the level of clouds which can be detected by these systems. The cloud detection threshold need be approximately twice this uncertainty to be sure of a cloud detection. This leads to a possible minimum detection threshold between 0.88 $W \cdot m^{-2} \cdot sr^{-1}$ for the 50° fov system and 1.14 $W \cdot m^{-2} \cdot sr^{-1}$ for the 100° fov system. The water vapor distribution in the atmosphere is not uniform, and setting the thresholds this low would lead to the misclassification of water vapor variations as clouds. Thus the more practical detection threshold has been set to 2 $W \cdot m^{-2} \cdot sr^{-1}$ for the 50° fov and an equivalent 1.8 $W \cdot m^{-2} \cdot sr^{-1}$ for the 100° fov system. This leads to a matched sensitivity with a minimum detectable cloud type of subvisual to high altitude cirrus clouds. However, matching the thresholds in this manner has placed the detection threshold of the 100° fov system much nearer its level of uncertainty.

Running inside the enclosure and viewing the scene through the germanium window adds an additional background signal. This signal has been observed to vary between 3.5 $W \cdot m^{-2} \cdot sr^{-1}$ on October 2nd, 2007 and 4.2 $W \cdot m^{-2} \cdot sr^{-1}$ on October 4th, 2007. This variation shows that removing a single bias value will not fully correct for the impact of this germanium window. To make a determination of the accuracy of the system running in this manner an in-depth study of the background reflection from this window needs to be conducted. Currently it is believed that running the 50° fov system in the enclosure will limit the ability to detect level 1 clouds (2 $W \cdot m^{-2} \cdot sr^{-1}$ to 4.5 $W \cdot m^{-2} \cdot sr^{-1}$). This would leave a minimum cloud detection threshold of level 2 clouds (4.5 $W \cdot m^{-2} \cdot sr^{-1}$), allowing for the detection of cirrus clouds, but missing subvisual and thin cirrus clouds.

Proposed Future Work

The completion of the work summarized in this thesis does not complete the work necessary for the development of the second-generation ICI systems. The following section presents much of the major work that needs to be conducted as a continuation of this project. This work includes improved cloud processing techniques, improved calibration of the cameras, weather hardening the instrument, and testing the system over an extended period of time in a harsh environment.

FOV-dependent Atmosphere and Cloud Emission

The adaptation of the atmospheric emission calculations to wide-angle ICI systems is not complete. The atmospheric emission has been adapted to account for the increase in the water vapor path length with increasing zenith angle. This has brought the variability of the expected water vapor radiance correction to within ± 0.25 $W \cdot m^{-2} \cdot sr^{-1}$ over a fov up to 100°. This characterization and the fov-dependent error could be reduced by further characterizing the change in emission with viewing angle. It is possible that this change is due to a changing temperature profile along the CO_2 path observed on the edges of the bandwidths for these cameras. This error may be similar to the increasing water vapor path length, and could possibly be handled by a sec(θ) term. This error has not been adequately studied at this time to make a absolute determination of the source of this error. Future MODTRAN simulations should be able to model this change and lead to improved processing routines. This may require the use of a multi-dimensional fit to clear-sky atmospheric radiance taking in variables that include: the surface temperature, temperature profile of the lower atmosphere, total atmospheric water vapor amount, zenith angle, amount of CO_2, and possibly other variables.

There also exists a similar problem with thin cirrus clouds. The ICI systems actually see through these clouds. Thus, viewing the cloud at increasing zenith angle will make the cloud appear to be thicker, and will cause an increase in emission from the same cloud with increasing zenith angle. Processing routines that can correct for this increasing radiance to provide correct cloud type classification is needed. This could be accomplished by fov dependent cloud classification thresholds.

Characterization of the Enclosure Window

One possible solution for extended deployments will be placing the camera inside of an enclosure with an infrared window. This option has been selected by the Optical Communications Group at JPL for upcoming deployment of the 50° fov system. Running inside this enclosure causes the camera to see a reflection of itself (narcissus) mixed with the observed scene. Therefore, building a system around this enclosure will require characterization of the reflected signal off the window. Minor modifications to the enclosure such as a low-emissivity tube between the camera and the window with the additional calibration measurements will reduce the uncertainty of the window reflection, but will not remove the reflection. Further characterization of the reflection may be possible during a deployment at TMF later this year. This characterization could take place by comparing the signals observed by the 100° fov system running outside the enclosure with the 50° fov system running inside the enclosure. It has been shown that both these systems can be calibrated to a level to produce similar data. After the needed recalibration of these systems it should be possible to produce data with similar accuracy.

Sun and Moon Error Removal

Currently the system views the sun and the moon directly. Viewing the sun, as specified by FLIR, should not damage the detector array or cause excessive data bleeding into nearby pixels. Both the sun and the moon cause a signal over a small region that would be classified as a cloud; such an error was seen in Figure 4-18. Software-based removal routines could be developed that would locate and subtract the region of pixels biased by the sun or moon. These routines would need to be updatable, taking into account the instrument orientation and geographic location.

Extended Deployment in a Harsh Environment

One of the next steps should be to deploy the system in an extended field experiment to validate its long-term stability and to begin generating cloud-fraction and cloud-type statistics. Long-term deployment of either of these systems will test the ability of these cameras to operate in varied climate, including snow, rain, warm ambient temperatures, and cold ambient temperatures. Deployment in such an environment will require the development of a weather hardened enclosure to protect the camera and the electronics from the harsh external conditions. One possible solution for this is to use an enclosure similar to the system selected by the Optical Communications Group at JPL for the system to be deployed at TMF. Another solution is currently being investigated by ORSL at MSU that will allow for harsher environments such as Barrow, AK and will avoid the problems introduced by the germanium window on the current enclosure.

Pending Deployment at TMF

Currently the methods for detecting clouds have been proven. The application of these data to the characterization of optical communication paths and to climate research is the next steps necessary for these systems. Work is underway to ready both the 50° fov and 100° fov second-generation ICI system for deployment at JPL's Table Mountain Facility. These systems will be used for the study of cloud cover statistics for the characterization of optical communication paths. The development of a third second-generation system is also underway. This system will have a 100° fov and is planned for deployment in the Arctic for studying clouds for climate research. Long-term deployment of any of these three systems will require that they be adapted to operate in varied climate conditions, including snow, rain, heat, and cold.

Much of the continued work proposed in the previous sections including the characterization work can be conducted during the deployment at JPL’s TMF which should take place shortly. This work can continue on these systems as long as cooperation between the Optical Communications Group at JPL and ORSL at MSU continues. The deployment of the third system at the ARM site near Barrow, AK will provide the needed Arctic testing of these systems. Both these deployments will provide important information about the long-term calibration stability of these instruments.

REFERENCES CITED

Anderson G. P., S. A. Clough, F. X. Kneizys, J. H. Chetwynd, E. P. Shettle, "AFGL Atmospheric Constituent Profiles (0-120km)." Air Force Geophysics Laboratory, Enviromental Research Papers, no. 954 (1986).

Baum B., T. Uttal, M. Pellot, T. Ackerman, J. Alverez, J. Interieri, D. Starr, J. Titlow, V. Tovinkere, and E. Clothiaux, "Satellite Remote Sensing of Multiple Cloud Layers," Journal of the Atmospheric Sciences," v. 52, no. 23, pp 4210–4230 (1995).

Churnside J. H., K. Shaik, "Atmospheric Propagation Issues Relevant to Optical Communications," NOAA Technical Memorandum ERL WPL-159 (Jan. 1989).

Erickson D., D. H. Tsiang, "Upgrade to the Atmospheric Visibility Monitoring System," Proceedings SPIE Free Space Laser Communication Technologies XI, v. 3615, pp. 310-315 (1999).

Holben B. N., T. F. Eck, I. Slutsker, D. Tanré, J. P. Buis, A. Setzer, E. Vermote, J. A. Reagan, Y. J. Kaufman, T. Nakajima, F. Lavenu, I. Jankowiak, and A. Smirnov, "AERONET: A Federated Instrument Network and Data Archive for Aerosol Characterization," Remote Sensing of the Environment, v. 66, n. 1, pp 1-16 (1998).

Jeganthan M., D. Erickson, "An Overview of the Atmospheric Visibility Monitoring (AVM) Program," Proceedings SPIE Free Space Laser Communication Technologies IX, v. 2990, pp. 114-120 (1997).

Kassianov E., C. N. Long, M. Ovtchinnikov, "Cloud Sky Cover versus Cloud Fraction: Whole-Sky Simulations and Observations," Journal of Applied Meteorology, v. 44, pp 86-98 (2005).

King M. D., Y. J. Kaufman, W. P. Menzel, D. Tanré, "Remote Sensing of Cloud, Aerosol, and Water Vapor Properties from the Moderate Resolutions Imaging Spectrometer (MODIS)," IEEE Transaction on Geoscience and Remote Sensing, v. 30, no. 1, pp 2-27 (Jan 1992).

Kruse P. W. "Uncooled Thermal Imaging, Arrays, Systems, and Applications," SPIE Press (2002).

Liou K. N. "Influence of Cirrus Clouds on Weather and Climate Processes: A Global Perspective," Monthly Weather Review, v. 114, pp 1167-1199 (1986).

REFERENCES CITED - CONTINUED

Liu Y., J. R. Key, R. A. Frey, S. A. Ackerman, W. P. Menzel, “Nightime Polar Cloud Detection With MODIS,” Remote Sensing of Environment, vol. 92, pp. 181-194 (2004).

Long C. N., D. W. Slater, T. Tooman, “Total Sky Imager (TSI) Model 880 Status and Testing Results,” U.S. Department of Energy, Washington D.C., ARM Technical Report ARM TR-006 (2001). Available Online at: http//www.arm.gov/publications/tech_reports/arm-tr-oo6.pdf

Long C. N., J. M. Sabburg, J. Calbó, D. Pagès, “Retrieving Cloud Characteristics from Ground-Based Daytime Color All-Sky Images,” vol. 23, pp 633-652 (2006).

MacDonald A. E., Y. Xie, and R. H. Ware, “Diagnosis of Three-Dimensional Water Vapor Using a GPS Network,” Monthly Weather Review, v. 130, pp 386-397 (2002).

Minnis P., W. Smith, D. Young, L. Nguyen, A. Rapp, S. Heck, P. Sun-Mack, Q. Trepte, and Y. Chen, “A Near-Real Time Method for Deriving Cloud and Radiation Properties from Satellites for Weather and Climate Studies,” Proceedings AMS 11th Conference on Satellite Meteorology and Oceanography, pp. 477-480 (2001).

OFCM, Office of the Federal Coordinator for Meteorological Services and Supporting Research “Federal Meteorological Handbook No. 1: Surface Weather Observations and Reports,” U.S. Department of Commerce, FCM-H1-2005, pp [12-7]-[12-8] (2005).

Piazzolla S., S. Slobin, and P. E. Amini, Cloud Coverage Diversity Statistics for Optical Communication in the Southwestern United States, JPL Publication 00-13 (Sep. 2000).

Piazzolla S., Personal Correspondence, NASA Jet Propulsion Laboratory, Aug 2007 (2007).

Planck M. “Theory of Heat, Volume V of Introduction to Theoretical Physics,” MacMillan and Co., pp 264-280 (1932).

Reitan C. H., “Surface Dew Point and Water Vapor Aloft,” Journal of Applied Meteorology, v. 2 pp 776-779 (1963)

Saleh B., M. C. Teich, “Fundamentals of Photonics,” Wiley, 1991, pp. 645-696 (1991).

REFERENCES CITED - CONTINUED

Seldomridge N. L., “Dual Polarization Cloud Lidar Design and Characterization,” Masters Thesis, Montana State University Electrical and Computer Engineering (2005). Available online at http://etd.lib.montana.edu/etd/view/item.php?id=68.

Seldomridge N. L., J. A. Shaw, K. S. Repasky, “Dual Polarization Cloud Lidar Using a Liquid Crystal Variable Retarder,” Opt. Eng. v. 45, n. 10, pp 106202-1 – 106202-10 (2006).

Shaw J. A. and L. Fedor, “Improved Calibration of Infrared Radiometers for Cloud-Temperature Remote sensing,” Opt. Eng., v. 32, no. 5, pp 1002–1010 (1993).

Shaw J. A., N. Cimini, E. R. Westwater, Y. Han, H. M. Zorn, and J. H. Churnside, “Scanning infrared radiometer for measuring the air-sea temperature difference,” Appl. Opt. 40, 4807-4815 (2001).

Shaw J. A., P. W. Nugent, N. J. Pust, B. Thurairajah, “Radiometric Cloud Imaging With an Uncooled Microbolometer Thermal Infrared Camera,” Opt. Exp., v. 13, no. 15, pp 5807-5817 (2005).

Shupe M. D. and J. M. Intrieri, “Cloud Radiative Forcing of the Arctic Surface: The Influence of Cloud Properties, Solar Albedo, and Solar Zenith Angle,” Journal of Climate, v. 17, pp 616-627 (2004)

Stephens G., “Remote Sensing of the Lower Atmosphere,” Oxford University Press 1994, pp. 328-334 (1994).

Sun C. H., and L. R. Thorne, “Inferring Spatial Cloud Statistics from Limited Field of View, Zenith Observations,” Proceedings ARM Science Team Meeting, CONF-9503140, pp 331-334 (1995), Available Online at: http://www.arm.gov/publications/proceedings/conf05/abstracts/76_95.pdf

Thurairajah B., J. A. Shaw, “Cloud Statistics Measured With the Infrared Cloud Imager (ICI),” IEEE Transactions on Geoscience and Remote Sensing, v. 43, no. 9, pp 2000-2007 (2005).

Thurairajah B. “Thermal Infrared Imaging of the Atmosphere The Infrared Cloud Imager,” Masters Thesis, Montana State University Electrical and Computer Engineering (2004). Available online at http://etd.lib.montana.edu/etd/view/item.php?id=274.

REFERENCES CITED – CONTINUED

TIROS, “Final Report on the TIROS I Meteorological Satellite System,” Goddard Space Flight Center and the U.S. Weather Bureau, NASA TR R-131 (1962).

Tomasi C., “Precipitable Water Vapor in Atmospheres Characterized by Temperature Inversions,” Journal of Applied Meteorology, v. 16, pp 237-243 (1977).

Tooman T. P., “Whole Sky Imager Retrieval Guide,” U.S. Department of Energy, Washington D.C., ARM Technical Report, ARM TR-011.1 (2003), Available Online at: http://www.arm.gov/publications/tech_reports/arm-tr-011-1.pdf.

Town M. S., V. P.Walden, S. G. Warren, “Cloud Cover over the South Pole from Visual Observations, Satellite Retrievals and Surface-Based Infrared Radiation Measurements,” Journal of Climate, vol. 20, pp. 544-559 (2007).

Wetherald R. T., and S. Manabe, “Cloud Cover and Climate Sensitivity,” Journal of the Atmospheric Sciences, v. 37, pp 1485-1510 (1980).

Wetherald R. T., and S. Manabe, “Cloud Feedback Processes in a General Circulation Model,” Journal of the Atmospheric Sciences, v. 45, n. 8, pp. 1397-1415 (1988).

Westwater E. R., Y. Han, M. D. Shupe, and S. Y. Matrosov, “Analysis of Integrated Cloud Liquid and Precipitable Water Vapor Retrievals from Microwave Radiometers During the Surface Heat Budget of the Arctic Ocean Project,” Journal of Geophysical Research, v. 106, n. D23, pp 32019-32030 (2001).

Wild M., A. Ohmura, and H. Gilgen, “Evaluation of Downward Longwave Radiation in General Circulation Models,” Journal of Climate, v. 14, pp 3227-3239 (2001).